Structural Optimization for Propulsion Airframe

Final Project Report

POLITECNICO DI TORINO	Laurea Magistrale in Ingegneria Aerospaziale
ISAE-SUPAERO	Diplôme Ingénieur Aéronautique
UNIVERSITÉ PAUL SABATIER	Génie Mécanique - SMMS

Author:
Gabriele Capasso

Supervisors:
Remi Amargier
Simone Coniglio
Joseph Morlier
Christine Mabru
Marco Di Sciuva

"The art of structure is where to put the holes."

Robert Le Ricolais

Abstract

Ultra High Bi-pass Ratio Engines constitute one of the most cutting-edge architectures in propulsion research panorama. Fundamentally, their introduction is motivated by the need of reducing fuel consumptions. Most of research projects on this topic focus on solving the numerous aerodynamic, control and structural challenges deriving from concepts. In this work, structural issues will constitute the central focus.

The present study is the result of a 6-month internship in Airbus Operations SAS (Toulouse, France). The project aims to explore possible solutions of the design of the airframe of such engines. For this purpose, Topology Optimization (TO) is adopted as main tool: it allows to find the optimal arrangement of masses in pre-sizing phases. In particular, TO is used when no knowledge (nor experience) on the possible designs is available.

A numerical model is developed in commercial software *Optistruct*. All engine configurations and most flight operative conditions are included in numerical analysis. Several mathematical formulations are investigated, and corresponding results are analyzed and reported. The final goal is to acquire an understanding on architectural features improving existent propulsion airframe.

Contents

1 Introduction **1**

1.1 Motivations 1

1.2 Context of the Study 2

1.3 Objectives and Contributions 2

1.4 Overview 3

2 UHBR Engines **4**

2.1 New Generation UHBR Engines 4

2.2 Main Structural Components 7

2.3 Aerodynamics considerations 8

2.4 Structural Issues 10

3 Topology Optimization **15**

3.1 Generalities on the method 15

3.1.1 Implicit Methods (Eulerian Approach) 15

3.1.2 Explicit Methods (Lagrangian Approach) 16

3.2 Focus on SIMP Approach 17

3.2.1 General Algorithm 18

3.2.2 Sensitivity Analysis 20

3.2.3 Aggregation approach 22

3.2.4 Numerical Instabilities 23

3.2.4.1 Mesh dependence 23

3.2.4.2 Checkerboard patterns 27

3.2.4.3 Local minima 29
3.2.5 Minimum member size control 30
3.2.6 Optimization Procedure 33
3.2.6.1 Approximation approach 34
3.2.6.2 Dual method approach 35
3.2.6.3 Convex Linearization Method (CONLIN) . . 36
3.2.7 Optimality Conditions 38
3.3 Previous Studies on Airframe Topology Optimization 39

4 Problem Statement **44**
4.1 Industrial Needs 44
4.2 Design Space Definition 45
4.3 Boundary Conditions 46
4.4 Load Cases 47
4.5 Material 49
4.6 Specific Requirements 50
4.6.1 Tip Clearance 50
4.6.2 Structural Performances 50
4.6.3 Multi Model Optimization (MMO) 51

5 Methodology **52**
5.1 Software Environment 52
5.2 Main Assumptions 53
5.3 Tip Clearance Computation 54
5.4 OGV Loads modeling 57
5.5 Constraints modeling 59
5.6 MMO Implementation 60
5.7 Analysis Procedure 61

6 Preliminary Results: Stow Configuration **64**
6.1 Classical Problem 64

6.2 Compliance Minimization (under TSFC and Volume Fraction constraints) . . . 70
6.3 TSFC Minimization . . . 74

7 Numerical Results **76**
7.1 First MMO Results . . . 77
7.1.1 Classical Problem . . . 77
7.1.2 Compliance Minimization (under TSFC constraint) . . 82
7.1.3 TSFC Minimization . . . 87
7.2 Final MMO Results: OGV Loads constraint introduction . . . 91
7.2.1 Compliance Minimization (complete formulation) . . . 91
7.2.2 OGV Loads Minimization . . . 98
7.2.3 TSFC Minimization . . . 98
7.2.4 Compliance Minimization (under OGV load constraint) 102
7.3 Pareto front . . . 104

8 Conclusions **107**

A Tip clearances convergence **110**

B Optimal Structures in Pareto front **116**

C Tabular Results **126**

References **136**

List of Figures

2.1 NextGen UHB, High OPR, Geared, Variable Pitch UHBR Engine Eliminates the Thrust Reverser and Achieves a 35:1 BPR (source: [1]) 5
2.2 Powerplant Fundamentals and Their Impact on Engine Architecture (source: [1]) 6
2.3 Pylon primary structure 8
2.4 Pylon secondary structure 8
2.5 Nacelle structure decomposition 9
2.6 Visualization of tip clearance variation 11
2.7 Effects of tip clearance variation on engine airframe (source: [2]) 12
2.8 Radial relative displacement terms c0, c1, c2, c3 (red) plotted as perturbations over the base circle (blue) 13

3.1 Numerical instabilities: MBB problem (a), checkerboard pattern (b), mesh-dependence (c-d) (source [41]) 24
3.2 Small design space (a) and optimised topology with respect to the tip clearance (b) and OGV stress minimization (c) 40
3.3 First optimization results from the large design space 41
3.4 Optimised topologies with respect to the compliance (a) and tip clearance (b) minimization (large design space) 43

4.1 Model of the Design Space: isometric view 47
4.2 Model of the Design Space: interfaces 48

5.1 Tip Clearance Modeling in Optistruct 54
5.2 OGV assembly: modified set-up 59

6.1 Classical Problem (MINMAX): iso-view of optimized structure 65
6.2 Classical Problem (with compliance aggregation): iso-view of optimized structure 67
6.3 Classical Problem (with compliance aggregation): convergence history 68
6.4 Classical Problem (with compliance aggregation): global gains 69
6.5 Compliance minimization under TSFC aggregated constraint (inactive at optimality): iso-view of optimized structure 71
6.6 Compliance minimization under TSFC aggregated constraint (active at optimality): iso-view of optimized structure 71
6.7 Compliance minimization under TSFC aggregated constraint: convergence history 72
6.8 Compliance minimization under TSFC aggregated constraint: global gains 74
6.9 TSFC minimization: iso-view of optimal structure (DELTOP=0.1) 75

7.1 Classical Problem (MMO): iso-view of optimised structure . . 78
7.2 Classical Problem (MMO): convergence history 80
7.3 Classical Problem (MMO): global gains 81
7.4 Compliance minimization under TSFC aggregated constraint (MMO): iso-view of optimised structure 83
7.5 Compliance minimization under TSFC aggregated constraint (MMO): convergence history 84
7.6 Compliance minimization under TSFC aggregated constraint (MMO): global gains 86
7.7 TSFC minimization (MMO): iso-view of optimised structure . 88
7.8 TSFC minimization (MMO): convergence history 89
7.9 TSFC minimization (MMO): global gains 90

7.10 Compliance minimization under TSFC and OGV load constraints (MMO): iso-view of optimised structure 93
7.11 Compliance minimization under TSFC and OGV load constraints (MMO): convergence history 95
7.12 Compliance minimization under TSFC and OGV load constraints (MMO): global gains 96
7.13 Compliance minimization under TSFC and OGV load constraints (MMO): results with different aggregation formulations (from left, $p-norm$, G^l_{KS} and G_KS) 97
7.14 OGV loads minimization under TSFC constraint (MMO): iso-view of optimised structure 99
7.15 OGV loads/compliance minimization under TSFC constraint (MMO): iso-view of optimised structure 100
7.16 TSFC minimization under OGV loads constraint (MMO): iso-view of optimised structure 101
7.17 Compliance minimization under OGV loads constraint (MMO): iso-view of optimised structure 103
7.18 Pareto front: Compliance vs volume fraction constraint 105
7.19 Pareto front: Compliance vs TSFC constraint 106
7.20 Pareto front: Compliance vs OGV bending constraint 106

A.1 Classical Problem (with compliance aggregation, Stow): tip clearance convergence history 110
A.2 Compliance minimization under TSFC constraint (Stow): tip clearance convergence history 111
A.3 Classical Problem (MMO): tip clearance convergence history . 112
A.4 Compliance minimization under TSFC constraint (MMO): tip clearance convergence history 113
A.5 TSFC minimization (MMO): tip clearance convergence history 114
A.6 Compliance minimization (complete formulation MMO): tip clearance convergence history 115

B.1 Pareto front ($V = 0.85\ V_0$): iso-view of optimised structure . 117
B.2 Pareto front ($V = 1.15\ V_0$): iso-view of optimised structure . 118
B.3 Pareto front ($V = 1.3\ V_0$): iso-view of optimised structure . . 119
B.4 Pareto front ($M = 2\ M_0$): iso-view of optimised structure . . 120
B.5 Pareto front ($M = 0.7\ M_0$): iso-view of optimised structure . 121
B.6 Pareto front ($M = 0.5\ M_0$): iso-view of optimised structure . 122
B.7 Pareto front ($TSFC = 1.2\ TSFC_0$): iso-view of optimised structure 123
B.8 Pareto front ($TSFC = 0.8\ TSFC_0$): iso-view of optimised structure 124
B.9 Pareto front ($TSFC = 0.6\ TSFC_0$): iso-view of optimised structure 125

List of Tables

4.1 Available Load cases in IFEM with TRU Shutter 49

5.1 Balance on adopted responses 60

C.1 Tabular results of Classical problem (MMO): relative variations 126
C.2 Tabular results of TSFC minimization (MMO): relative variations 127
C.3 Tabular results of complete formulation: relative variations . . 128

Nomenclature

TO	Topology Optimization
TL	Thrust link
TC	Tip Clearance
UHBR	Ultra High Bypass Ratio Turbofan
TSFC	Thrust Specific Fuel Consumption
PPS	Power Plant Structure
IFEM	Integrated Finite Element Model
TRU	Thrust Reverser Unit
TBS	Torque Box Structure
WEM	Whole Engine Model
OFS	Outer Fixed Strucure
IFS	Inner Fixed Structure
DOE	Design Of Experiment
LC	Load Case
FBO	Fan Blade Off
LHS	Left Hand Side
RHS	Right Hand Side
IPC	Intermediate Pressure Compressor
HPC	High Pressure Compressor
IPT	Intermediate Pressure Turbine
HPT	High Pressure Turbine

Chapter 1

Introduction

The present work constitutes the final report of the Project I developed in Airbus Operations SAS (Toulouse, France) during my 6-month internship.

1.1 Motivations

Among flight companies exists an increasing interest in fleet fuel consumption. Airbus can continuously improve the fuel efficiency of its planes thanks to the integration of new engines. The improvements in turbomachinery and combustion efficiency are not good enough to satisfy these needs, so that the BPR must be increased to ultra-high values to attain the requested TSFC.

With an Ultra High Bypass Ratio (UHBR) the engine reaches a size never seen before and its integration becomes challenging from a structural point of view.

Within this picture engineers from both engine and aircraft manufacturers are struggling to design a light integrated power plant and are moving to new integration architectures. For this purpose, no previous knowledge seems adapted and totally new structures are needed. Topology Optimization is the tool we are now using to explore new concepts, and to find some innovative solutions. The base idea is to find the best arrangement of masses to obtain the stiffest structure possible, within satisfying all structural constraints and

without deteriorating aerodynamic performances.

Being fuel consumption the critical parameter, an appropriate study of engine deformation is needed. The integration of engine deformations in a FEM can allow optimizing the power plant structure for fuel consumption.

1.2 Context of the Study

The present work is inserted in an Airbus project, developed in "Transverse Stress Team", devoted to the stress-analysis of the engine support.

Our team is part of the Engineering Structure group, which reunites engineers involved in Structure Analysis and Design. Among the several sectors in this department, there is the Engine Structure and Design group. Our equip is located inside this group and collaborates with other teams to encounter all the industrial needs for the Engine Airframe.

1.3 Objectives and Contributions

In 2018, an analogue internship took place to initiate the parametric study of several components of the engine support and the pylon topology itself. It was verified that Topology Optimization could take place in earl phases of Power Plant Structure (PPS) architecture. However, the design of the Engine also evolved since then.

This study aims to apply Topology Optimization (TO) of Power Plant Structure (PPS) on mass, loads, standard engine performance criteria and on an engine deformation criteria. This is done in order to discovering the leading criteria which would allow engineers to conceive a solution which could substitute classical pylon and nacelle architectures. The final goal consists in understanding the logic and to provide sufficient knowledge on the best designs to support such an innovative structure, both from structural and aerodynamic point of view.

In the present work, several modifications to the assumptions on which

the Design Space was based and to the modeling of responses have been defined and implemented into an *Optistruct* environment. This choice was established to focus on the analysis of all possible mathematical formulations of the TO problem and examine all effects of variations of the hyper-parameters. Although implementation does not constitute the main issue, the logic followed by the software is outlined and exploited at the maximum.

A fundamental contribution is given by the integration of multiple models in the same scenario. Different scenarios are then explored, always to provide sound basis to analogue engineering problems.

1.4 Overview

In Chapter 2, a literature review reports most of the useful sources to better analyze the industrial problem to be solved.

In Chapter 3, the tool known as TO is described, outlining all recent results found in literature.

The Problem Statement is exposed and discussed in Chapter 4, including all the engineering choices at the base of the whole project.

The adopted methodology and implementation choices are illustrated in Chapter 5.

Then, in Chapter 6 some preliminary results are reported to establish the first differences with the previous work.

Full numerical results on Multi-Model Optimization (MMO) are collected and elaborated in Chapter 7: these will include different scenarios, the choice of the best one, with relative complete post-processing. Moreover, a Pareto front based on the variations of individual constraints of the best candidate formulation is traced.

Finally, a complete balance on the present work is reported in Chapter 8, together with all possible way-forwards and perspectives for future work.

Chapter 2

UHBR Engines

In this chapter a literature review on Ultra High Bi-pass ratio Engines (UHBR). In Section 2.1, few generalities on the new engine are presented. In Section 2.2, main structural components are described. Section 2.3 reports several studies on aerodynamic issues related to UHBR Engines and taken into account in the present work. Finally, in Section 2.4, structural outcomes of this innovative system are outlined.

2.1 New Generation UHBR Engines

The NASA *Aeronautics Research Mission Directorate* established two projects, *Fundamental Aeronautics Program Subsonic Fixed Wing Project* and *Integrated Systems Research Program Environmentally Responsible Aviation Project*, both conducting research on advanced aircraft technology to address the environmental goals of reducing fuel burn, noise and NOx emissions for future aircrafts (the former beyond 2025, the latter by 2020)[3]. Among all research topics, the most important regard: advanced materials, like Ceramic Metal Composites and Superalloys; three dimensional aerodynamic compressor and turbine designs; advanced engine core research to produce higher thermal efficiencies; advanced engine technology research, in the areas of Ultra High Bypass Ratio and Open Rotor engine cycles.

The present study will be focused on Ultra High Bi-pass ratio Engines (UHBR).

Figure 2.1: NextGen UHB, High OPR, Geared, Variable Pitch UHBR Engine Eliminates the Thrust Reverser and Achieves a 35:1 BPR (source: [1])

The primary purpose of increasing bypass ratio is to improve the propulsive efficiency of the turbofan engine.

The ultimate end point for this would be a design which eliminates the nacelle entirely which would result in effective bypass ratios beyond 50. However, it is generally accepted that single rotation propeller systems are limited to Mach 0.7. Counterrotating open rotor systems with highly swept blades can remain efficient up to Mach 0.8 but beyond that efficiency falls off rapidly. Since most commercial flight operations are configured around aircraft flying between Mach 0.82 and Mach 0.85 any new aircraft system needs to fly in that speed range. As consequence, bypass ratios are limited, in theory, to about 35 [1].

In addition, meeting future more stringent noise regulations would be difficult. Since low fuel burn is achieved by increases in both propulsive efficiency and thermal efficiency, as shown in Figure 2.2, commensurate improvement in core technology for a future UHBR engine must also be developed.

Many programs, both civil and military, are ongoing which aim to develop

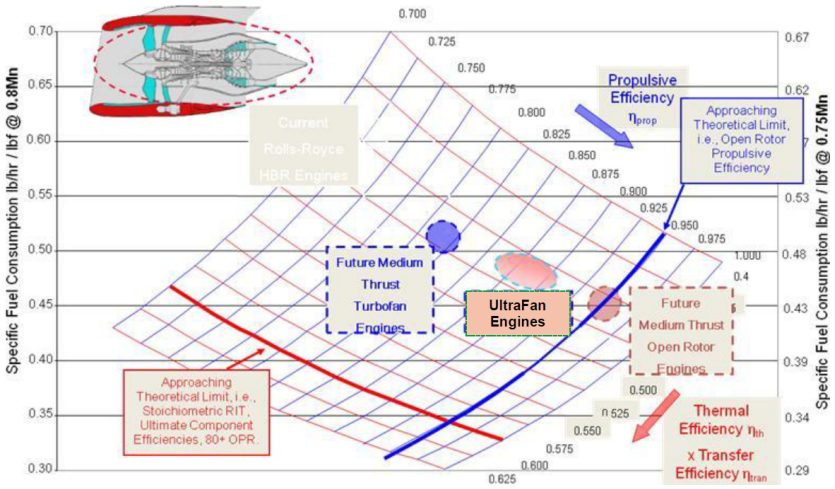

Figure 2.2: Powerplant Fundamentals and Their Impact on Engine Architecture (source: [1])

higher Overall Pressure Ratio, high temperature cores with high component efficiencies.

Pushing bypass ratios to the ultra high levels envisioned (of about 35) required attention to some fundamental items which have been a barrier to advancing BPR since the invention of the high bypass turbofan engine in the late 1960's. Primarily these are controlling the weight of the low pressure system turbomachinery, controlling losses in the bypass air stream, and minimizing the weight and drag of the nacelle system. In addition, since high bypass ratio is accompanied by much lower Fan Pressure Ratios (FPR) an additional problem of controlling stall and flutter margins at off-design conditions is manifested. In [1], the primary technology considered for controlling LP system weight was a lightweight geared fan system coupled with an ultra slimline composite nacelle.

2.2 Main Structural Components

The Power Plant Structure (PPS) is a component of the aircraft that has the function to pass the propulsive force acting on the engine to the airplane. Its design strongly depends on the position of the engine on the plane. For civil passenger planes the engine are usually located near the wings. In particular for commercial jets the engines are located under the wing, slightly forward. This position is efficient in terms of aerodynamic.

In this case the PPS is made of the pylon and the nacelle. In the pylon we can identify:

- Pylon primary structure: it maintains the engine in his place and is the load path between engine and wing;

- Pylon secondary structure: It supports the aerodynamic surfaces and some fundamental systems.

The pylon design is a box-type structure: This assures that both bending and torque are passed from the engine to the wing. A current approach used for wing mounts and engine mounts is to have a isostatic connection so that loads are determined easily and independently of the design of the connected components. Furthermore, only an isostatic engine mounts guarantees that no stress is induced from engine thermal expansion.

No loads from the engine are transferred through the secondary structure. It serves to define the external aerodynamic shapes and to host systems.

The nacelle is composed of several units, which together define an aerodynamic shape around the engine, define the secondary flow duct and the primary flux final duct, as well as absorbing the engine noise and serve as a flow reverser. In the following images the location of the nacelle parts are shown. The TRU (Thrust Reverse Unit) is a mechanism which deploys and changes the direction of the secondary flow.

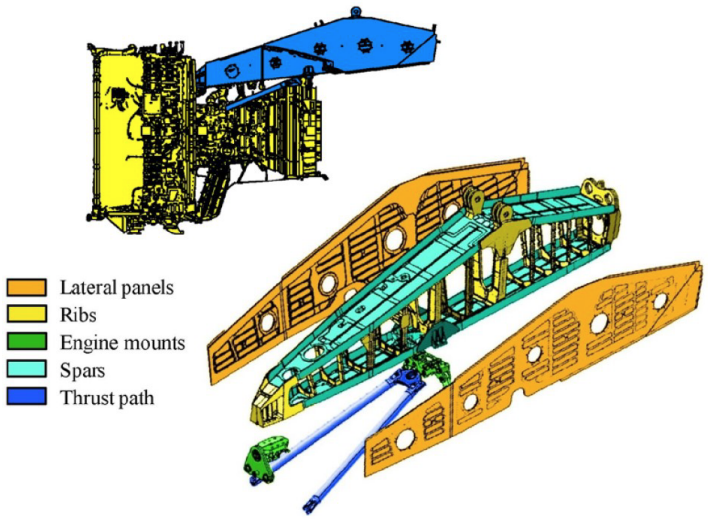

Figure 2.3: Pylon primary structure

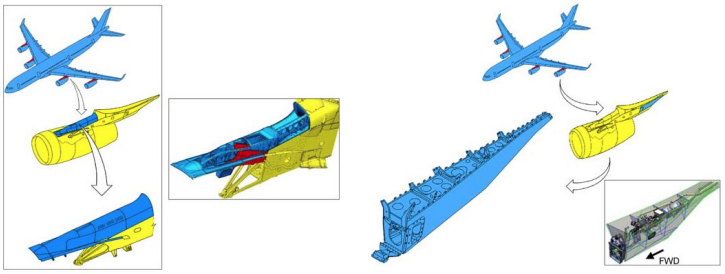

Figure 2.4: Pylon secondary structure

2.3 Aerodynamics considerations

Designing a UHBPR Engine has proved challenging since the introduction of the concept in late 1960's [3], involving a number of engineering fields. One major difficulty is given by aerodynamic performances. Several innovative concepts dealing with this issue can be found in literature.

Work in [4] analyses the possibility of overwing nacelle installations to improve energy efficiency on turbofan and, above all, UHBR engines. Detailed design studies were performed on the 6 configurations identified in the initial

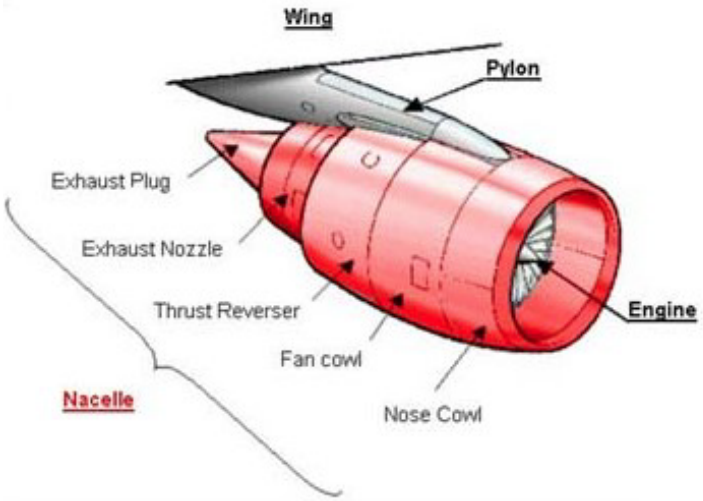

Figure 2.5: Nacelle structure decomposition

shape optimization effort at two transonic Mach numbers (M = 0.80 and 0.85). The pylons were designed to have similar characteristics to either existing pylons or pylons in development for future mobility concepts. Results from [4] demonstrate that the installation of the ultra fan engine significantly increases the wing shock strength and that the incorporation of the pylon further increases its strength. However, they also illustrate that it's possible to optimize the wing shape to significantly reduce the shock strength.

The progression towards ever higher bypass ratios in commercial gas turbine engines has increased the operating disparity between the fan flow conditions at different flight speeds, requiring the use of variable geometry to maintain the surge margin throughout the flight envelope [5]. Mechanisms such as a Variable Pitch Fan (VPF) and a Variable Area Nozzle (VPN) help maintain the surge margin while providing greater fuel burn reduction, especially as engine bypass ratio increases [6]. Reference [1] states that the weight penalty associated with VAN area variation becomes prohibitive at very low FPR, finding that a BPR of 25 is the cross-over point at which a VPF becomes necessary (vs. 20-27 in [5]). More importantly, the results of this research show that, on a completely equal footing and common cycle

settings, the difference in fuel burn consumption between the VPF and VAN are on the order of 3 percent.

Being the subject very recent, such system architectures cannot be found in commercial aircrafts. However, Airbus is trying to make these concepts reality.

2.4 Structural Issues

With Ultra High Bypass Ratio engines, the front part of the engine becomes bigger and aerodynamic loads as well as inertial loads on the fan case increase. This means that the engine itself is subjected to more bending and torsion. Moreover, bending of the engine shaft as well as stator casing deformation can impact tip clearance.

Tip clearance on a blade is defined as the distance of the tip of the blade from the internal wall of the stator casing. The tip clearance depends mainly form the deformation of 3 different components:

- Blade elongation caused by thermal expansion and centrifugal force;
- Shaft bending;
- Stator casing deformation.

A visualization of the tip clearance variation is reported in Figure 2.6.

The noise due to TC in axial flow fans having two different TCs has been investigated by experimental analysis using two rotating hot-wire sensors at a design and off-design operating conditions [7]. Noise increase due to TC at low flow rate conditions is mainly caused by high velocity fluctuation in a vortical flow and the interference between tip leakage vortex and adjacent pressure surface as well as the casing surface. The intensity of velocity fluctuation is increased by enlarging the TC and decreasing the flow rate.

Reducing tip clearance both improves performance and reduces noise, not only at the maximum efficiency operating point but also in an appreciable

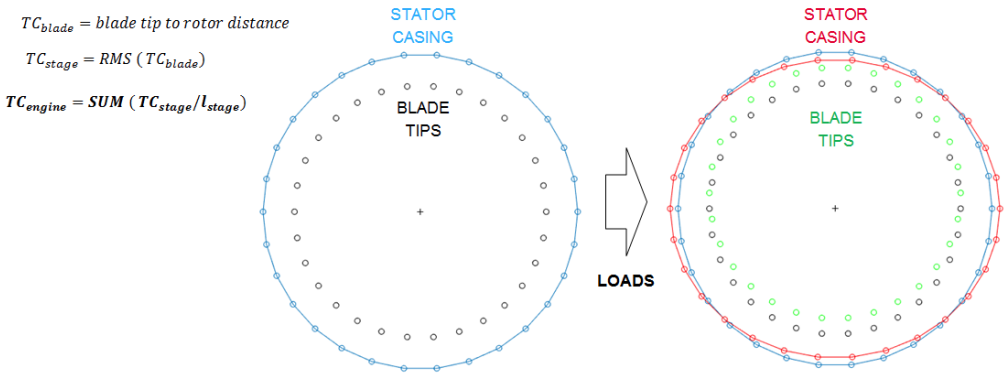

Figure 2.6: Visualization of tip clearance variation

low flow rate operating region. With tip clearances small enough to optimize performance and minimize noise fan/duct eccentricity must be kept to a very small value, implying strict precautions in fan and duct manufacture, installation and service conditions [8].

Martin [9] reported a 1 % loss estimate in engine performance due to clearance changes that occurs during the production flight test acceptance profile 9. As the engine operating clearances increase, the engine must work harder (hotter) to produce the same work and is therefore, less efficient. This increase in operating temperature, particularly takeoff Exhaust Gas Temperature (EGT), further promotes the degradation of hot section components due to thermal fatigue. Retaining engine takeoff EGT margin by maintaining tight tip clearances and either eliminating rubs or compensating for them can dramatically increase engine cycle life. This could also lead to huge savings in engine maintenance over a period of years due to the large overhaul costs.

In [2] one can find all the issues related to the tip clearance and its variations. Figure 2.7 show the possibility of the appearance of rubbing on the blade tips on the stator internal wall. This prematurely damages the abradable coating of the stator internal wall and permanently affects the tip clearance. In particular, rubbing occurs when there is a closure of the tip clearance.

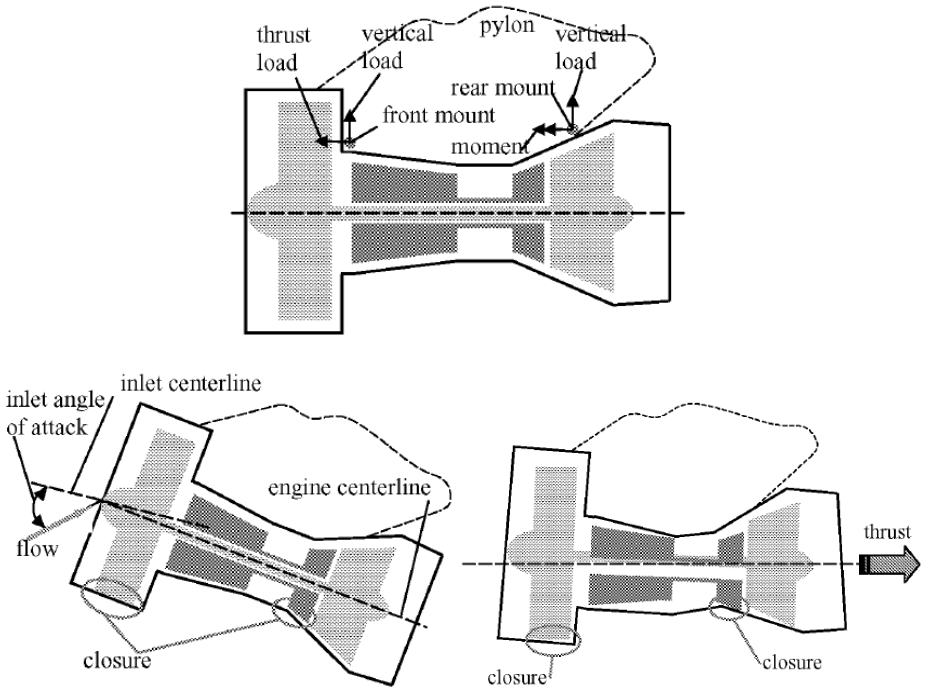

Figure 2.7: Effects of tip clearance variation on engine airframe (source: [2])

A useful approach to tip clearance computation consists in expressing the stator displacement in a cylindrical system around the engine axis [10]. This simplification doesn't require any hypothesis on axisymmetrique nature of the internal flow. We are only interested in the radial component for tip clearance, which can be determined through a Fourier series:

$$u_r(\theta) = \sum_{i=0}^{\infty} c'_i \cos(i\theta + \phi'_i)$$

If we now want the relative radial displacement between shaft and stator:

$$TC(\theta) = u_r(\theta) u_{shaft} \cos(\phi_{shaft} + \theta)$$

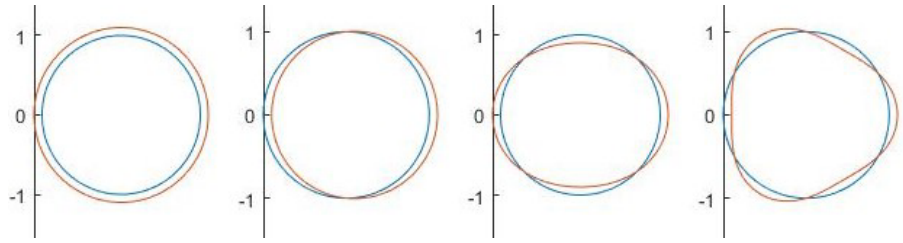

Figure 2.8: Radial relative displacement terms c0, c1, c2, c3 (red) plotted as perturbations over the base circle (blue)

With

$$u_{shaft,y} = u_{shaft}\cos(\phi_{shaft}), \qquad u_{shaft,y} = u_{shaft}\sin(\phi_{shaft})$$

. The added term is a term with $i = 0$. Therefore, also $TC(\theta)$ can be expressed in a Fourier decomposition.

$$TC(\theta) = \sum_{i=0}^{\infty} c_i \cos(i\theta + \phi_i) \tag{2.1}$$

Figure 2.8 shows the shape of the first terms of the series.

By simplifying the formula in 2.1 one obtains:

$$c_{TCi} = \sum_{j=1}^{n_i} \left(\frac{1}{l_j} \sqrt{\frac{1}{m_j} \sum_{l=1}^{m_j} \left[(v_{\alpha j} - v_{sjl})^2 + (w_{\alpha j} - w_{sjl})^2 \right]} \right) \tag{2.2}$$

Where:

- n_i is the number of stages in the module;
- l_j is the blade length of the stage j;
- m_j is the number of nodes on the stator of stage j;
- $v_{\alpha j}$ and $w_{\alpha j}$ are the shaft displacement on stage j along y and z direction respectively;

- v_{sjl} and w_{sjl} are the l-th stator node displacements on stage j along y and z direction respectively.

The tip clearance formula has been simplified in order to take into consideration only the eccentricity term (relative shaft-stator relative displacement). This constitutes the c1 term in the polar Fourier decomposition of tip clearance. This can be done for two reasons:

- any other terms (isotetic expansion, ovalization and successive terms) depend on the local stator structure, while the shaft-rotor relative displacement depends more on the PPS architecture;

- considering only the eccentricity term decreases the computational cost of each simulation.

Chapter 3

Topology Optimization

In this chapter a literature review on Topology Optimization (TO) is reported. In Section 3.1, a simplified description of the generalities of the method is briefly discussed. In Section 3.2, the state of the art on a particular approach is analyzed. Finally, Section 3.3 presents an analogue work performed in another internship in Airbus Operations SAS in 2018.

3.1 Generalities on the method

The past twenty years have seen increasingly rapid advances in the field of structural optimization: in particular, Topology Optimization (**TO**) is becoming a key figure in the research panorama. This method leads to an optimal structural efficiency, through the removal of unnecessarily placed material, in order to accomplish the minimization of a given objective (such as the compliance of the system). In [11] one can find an up to date review of the most promising applications of TO to classical aerospace structures.

3.1.1 Implicit Methods (Eulerian Approach)

Since the pioneering work of Bendsoe and Kikuchi (1988) [12] a number of implicit approaches has been proposed, among which: density-based methods

(the well-known SIMP algorithm) [13, 14], evolutionary strategies [15] and level-set based methods [16, 17]. The key feature is the parameterization of the topology based on an Eulerian approach, similar to the one adopted in fluid Dynamics: every finite elements is described locally independently to the surroundings. This outcomes into an optimization problem with a very large number of design variables (one for each finite element).

This methods are widely adopted in commercial softwares, such as the well-known Optistruct.

3.1.2 Explicit Methods (Lagrangian Approach)

Most of the existing approaches actually do topology optimization in an implicit way. This means that in these approaches the optimal structural topology is identified either from a black-and-white pixel image (in SIMP approach) or from the level set of a Topology Description Function (TDF) defined in a prescribed design domain (in level set approach). Possible problems associated with the implicit methods can be summarized as follows. Firstly, it is difficult to give a precise control of the structural feature sizes, which is very important from manufacturing point of view, under the implicit topology optimization framework. This is because there is no explicit geometry information embedded in the implicit optimization mode.

In this context is the article by Norato et al. [18] inserted: they adopted a fictitious domain method for topology optimization in which a level set of the topological derivative field for the cost function identifies the boundary of the optimal design. This method took inspiration from an analogue method adopted in shape optimization problems [19]. Some elementary components are thus projected onto a fictitious domain, simplifying the response analysis and the enhancing convergence of the optimization algorithm. This was the first step toward a deeper study of Explicit Topology Optimization, However, the method still lacked robustness to guarantee additional constraints.

Norato et al. [20] then introduced another method to design structures by introducing fixed-width and fixed-thickness using continuum-based TO.

This is based once again on the Geometric Projection of rounded-end beams described by their end points. The consequent reduction in terms of design variable is enormous, since only the coordinates of the end points of a limited number of components are needed to completely define the problem.

Another approach presented by Zhang et al. [21] is inserted in the same context: this has been the first work focused on an explicit description of the geometry through BEAM elements (Moving Morphable Components or MMC) with variable geometry.

Several extensions to this work have been proposed. One of the most-known is the Moving Morphable Void (MMV) approach [22], which considers the voids as the real components of the structure. Proposing essentially a two-dimensional case, this has been developed and extended to the three-dimensional case [23] and to stress-based TO [24].

Finally, the introduction of plate structures in the work published by Zhang and Norato [25] constitutes one of the most cutting-edge generalization of the Explicit TO panorama.

3.2 Focus on SIMP Approach

Despite their improved performances, explicit methods are not sufficiently mature to be implemented in commercial softwares, like Optistruct.

The density-based approach, also known as Solid Isotropic Material with Penalization (SIMP), is the most popular TO method. SIMP has a solid mathematical foundation. This method is capable of handling various objectives and constraints, and is relatively easy to implement within a finite element environment.

Several researchers tried to implement and diffuse simple and efficient codes. One of the most known and important results is due to Andreassen et al. [26], who created a very simple and efficient 88-line code written in *MATLAB*, capable of optimizing a MBB beam through a SIMP algorithm. Compared to other available codes and the same 99-line code (published by

Sigmund et al. [27]), the former needs much less computational power, thanks to a wise use of vectorization and pre-allocation of most of the variables. Moreover, this work can be used as reference to understand how an use-friendly Topology Optimization software work.

3.2.1 General Algorithm

The starting point is given by a discrete compliance minimization problem, which can be formalised as follows:

$$\begin{cases} min & f(x_1, x_2, ..., x_n) \\ s.t.: & \sum_{i=1}^{n} x_i = V \\ & x_i = 0 \text{ or } 1 \quad \forall i = 1, ..., n \end{cases} \tag{3.1}$$

The binary compliance problem is known to be ill-posed [28].

One alternative to make the compliance problem well-posed is to control the perimeter of the structure [29, 30]. Another alternative is to relax the binary condition and include intermediate material densities in the problem formulation. This method is referred to as *homogenization method for topology optimization* [31]. The main drawback of this approach is that the optimal microstructure, which is required in the derivation of the relaxed problem, is not always known. This can be alleviated by restricting the method to a subclass of microstructures, possibly suboptimal but fully explicit. This approach, referred to as *partial relaxation* [12]. Another problem with the homogenization methods is the manufacturability of the optimized structure (gray areas). However, this problem can be mitigated with penalization strategies. One approach is to impose a priori restrictions on the microstructure that implicitly lead to black-and-white designs [31]. Even though penalization methods have shown to be effective in avoiding or mitigating intermediate densities, they revert the problem back to the original ill-posedness with respect to the mesh refinement.

An alternative that avoids the application of homogenization theory is

to relax the binary problem using a continuous density value with no microstructure. The mechanical properties of the material are determined using a power-law interpolation function between void and solid [32]. This power law implicitly penalizes intermediate density values driving the structure towards a black-and-white configuration. This approach is usually referred to as the *solid isotropic material with penalization* (SIMP) method. The SIMP method does not solve the problems ill-possedness, but it is simpler than other penalization methods.

The basic idea behind FEA based SIMP is that each finite element is associated with a fictitious pseudo-density variable $0 \leq \rho_e \leq 1$, that essentially parameterizes the topology (here 0 would represent the total absence of material in an element) . This intervenes in the Young Modulus definition, through the relation:

$$E_e = E_{min} + \rho_e^p \left(E_0 - E_{min}\right) \tag{3.2}$$

where p is a penalty factor which prevents from obtaining a solution with intermediate densities between 0 and 1 (typically $p = 3$). A non-null minimum value for the Young Modulus E_{min} in empty elements guarantees the non-singularity of the stiffness matrix. This has to be set on a very low value, in order to prevent empty elements from interfering with the actual topology. The pseudo-densities are then optimized to reach the desired objective J.

Very few mathematical justification of this method can be found. In [33], the classical TO problem (compliance minimization under volume fraction constraint) is analyzed from a mathematical point of view, making an equivalence between discrete problem in Eq. 3.1 and the equivalent TO problem in SIMP approach, which can be formalised as follows:

$$\begin{cases} min & f(x_1^p, x_2^p, ..., x_n^p) \\ s.t.: & \sum_{i=1}^{n} x_i = V \\ & 0 \leq x_i \leq 1 \quad \forall i = 1, ..., n \end{cases} \tag{3.3}$$

In [33], Rietz enunciates and proves the following theorem:

Theorem *Assume that the discrete problem in Eq. 3.1 has a unique solution and that the objective function f is continuously differentiable and that its derivatives fulfill:*

$$C \leq \frac{\partial f}{\partial x_i} \leq D, \quad \forall i = 1, ..., n$$

where C and D are some constants less than zero. Also assume that the volume V is an integer. Then the problem in Eq. 3.3 will have the same solution as Eq. 3.1 for a sufficiently high finite value of p.

In general, every TO problem can be formalized as follows:

$$\begin{cases} min_{0 \leq \rho \leq 1} & J(\rho, U_f) \\ s.t.: & h_i(\rho, U_f) = 0 \quad \forall i = 1, ..., M \\ & g_i(\rho, U_f) \leq 0 \quad \forall i = 1, ..., N \end{cases} \tag{3.4}$$

Here U_f represents the free nodal displacements, h_i the equality constraints and g_i the inequality constraints. Among h_i, equilibrium constraints always appear: this is traduced by imposing a null force residual in all of degrees of freedom and simplified in the usual relation $KU = F$ in linear mechanics. The general algorithm is detailed in Algorithm 1.

3.2.2 Sensitivity Analysis

Since the objective and constraint function depend both on density distribution and nodal displacements, an adjoint sensitivity analysis is to be performed. In particular, we use an augmented Lagrangian $L[\rho, U_F(\rho)]$, which may be defined as follows:

$$L = f + \lambda^T R \tag{3.5}$$

Algorithm 1 *SIMP* Algorithm

Initialization:
  Densities, mesh-independency filter
Main loop:
  while convergence not reached **do**
    FE Analysis
    Objective and Constraints evaluation
    Derivatives evaluation
    Mesh-independency filter applied to sensitivity
    Update of density
    Mesh-independency filter applied to density
  end while
Density results analysis

Here f indicates a general function, indifferently the objective or the constraint; λ is a Lagrange multiplier ensuring that the residual of forces R vanishes. Deriving this expression and using the chain rule, we obtain:

$$\frac{dL}{d\rho} = \frac{\partial f}{\partial \rho} + \frac{\partial f}{\partial U_F}\frac{dU_F}{d\rho} + \lambda^T \left(\frac{\partial R}{\partial \rho} + \frac{\partial R}{\partial U_F}\frac{dU_F}{d\rho} \right) \tag{3.6}$$

Collecting all the implicit terms indicated by $\frac{d}{d\rho}$, we obtain:

$$\frac{dL}{d\rho} = \frac{\partial f}{\partial \rho} + \lambda^T \frac{\partial R}{\partial \rho} + \left(\frac{\partial f}{\partial U_F} + \lambda^T \frac{\partial R}{\partial U_F} \right) \frac{dU_F}{d\rho} \tag{3.7}$$

In order to annihilate the implicit dependence of free nodal displacements on density distribution, the lagrangian multiplier can be computed, remembering the definition of the derivative of the residual related to the nodal displacements, as follows:

$$\lambda^T = -\frac{\partial f}{\partial U_F}\frac{\partial R}{\partial U_F}^{-1} = -\frac{\partial f}{\partial U_F} K_T^{-1} \tag{3.8}$$

Finally, we can obtain:

$$\frac{dL}{d\rho} = \frac{\partial f}{\partial \rho} + \lambda^T \frac{\partial R}{\partial \rho} \tag{3.9}$$

One can observe that the evaluation of gradients only requires a linear system of equation resolution, extremely convenient if compared with direct or finite difference approaches.

3.2.3 Aggregation approach

As the number of constraints increases, the maximum may be taken into account to represent the whole domain. Given the fact that the max function is non-derivable, there is the need to approximate it. A number of aggregation methods are available in literature [37]. In classical stress-based TO, the lower bound of Kreisselmeier-Steinhauser function [38, 39] is employed:

$$\max_i \overline{g}_i \approx G^l_{KS} = \frac{1}{P} \log \left(\frac{1}{N} \sum_{i=1}^{N} e^{P\overline{g}_i} \right) \tag{3.10}$$

The bigger is the factor P, better will be the approximation of the max, but also more expensive will be the computational cost of the overall optimization process. In fact the non-convexity of the optimization problem is enhanced by the use of higher values of P. Therefore, P has to be chosen as an appropriate compromise between computational burden and accuracy in stress control.

Optistruct is an *Hypermesh* environment which adopts another constraint aggregation method, known as $p - norm$ [37] and formulated as follows:

$$\max \overline{g}_i \approx \left(\sum_i \overline{g}_i^P \right)^{\frac{1}{P}} \tag{3.11}$$

Stability of this operator is fairly discussed in [40]: the same considerations outlined for the lower bound of Kreisselmeier-Steinhauser function can be extended for the $p - norm$.

Moreover, such approaches can be adopted to aggregate objective and

constraint functions defined in multiple load cases.

3.2.4 Numerical Instabilities

In [41] one can find a complete review on numerical instabilities in TO. The most common issues can be divided into three categories:

- *Checkerboards*: refer to the problem of formation of re- gions of alternating solid and void elements ordered in a checkerboard like fashion;
- *Mesh dependence*: refers to the problem of not obtaining qualitatively the same solution for different mesh-sizes or discretizations;
- *Local minima*: refers to the problem of obtaining different solutions to the same discretized problem when choosing different algorithmic parameters.

In the following, all categories will be detailed, as well as the proposed method to overcome these difficulties.

3.2.4.1 Mesh dependence

The mesh-dependence problem is illustrated in Figs. 3.1c and d. Figure lc shows the optimal topology for the so-called MBB- problem discretized by 600 finite elements (optimized using the SIMP approach). Solving the same problem but now with a 5400 finite element discretization, results in a much more detailed structure (Fig. 3.1d). Ideally mesh-refinement should result in a better finite element modeling of the same optimal structure and a better description of boundaries - not in a more detailed and qualitatively different structure.

Mesh-dependence problems can be divided into two categories:

- the problem of (necessarily) obtaining finer and finer structure with mesh- refinement, which is due to the previously discussed problem of nonexistence of solutions;

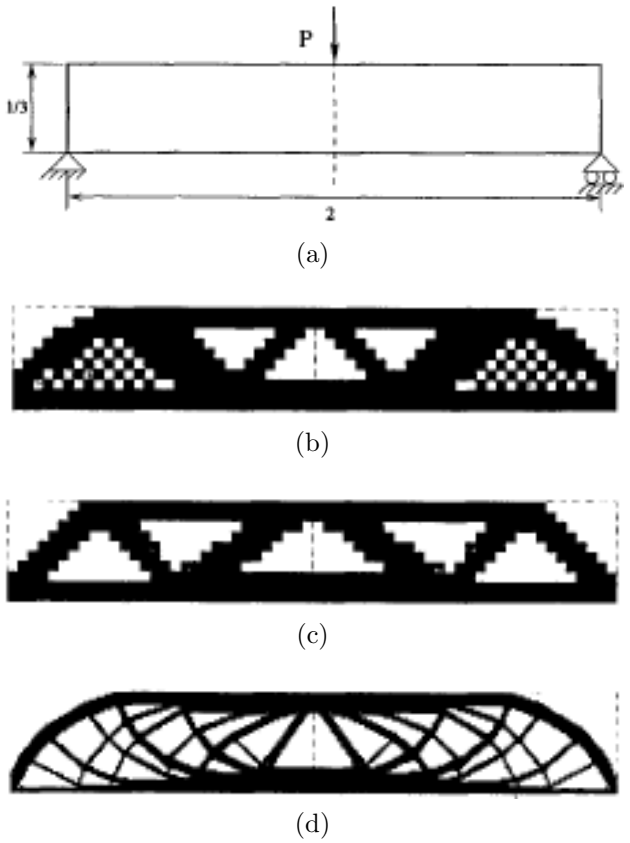

Figure 3.1: Numerical instabilities: MBB problem (a), checkerboard pattern (b), mesh-dependence (c-d) (source [41])

- problems with many optima, i.e. nonunique solutions.

An example of the latter is the design of a structure in uni-axial tension. Here a structure consisting of one thick bar will be just as good as a structure made up of several thin bars with the same overall area. In category (a) the refinement into a finer structure follows necessarily since it gives a strictly better value of the objective function. In (b) a finer structure is always possible but not necessary.

Naturally, one cannot set up schemes that remove the non-uniqueness problem, but by introducing manufacturing constraints such as a minimum

area constraint a less oscillating solution can be determined.

A first scheme to prevent the nonexistence problems is known as *relaxation method*: it is constituted by an enlargement of the design set to achieve existence. A particular approach to obtain a well-posed problem for a broad range of problems is to allow all materials with a symmetric and positive semidefinite elasticity tensor to compete in the problem. This converts the problem to one where the energy depends linearly on ρ [42]. Here, the variable ρ is allowed to attain all values between 0 and 1. This linear problem in one sense provides the "most relaxed" problem, and gives a useful bound on the maximum structural efficiency. It also models the variable thickness sheet problem, where ρ is interpreted as the thickness function of a two-dimensional sheet. Henceforth we will use this term for any topology optimization problem where the energy depends linearly on ρ.

Unless one is interested in resulting design with composite areas, this approach does in general not result in easily manufacturable solutions (i.e. macroscopic 0-1 designs). For this reason, three *restriction methods* are currently employed: *perimeter control*, *mesh independent filtering* and *density slope control*.

- ***Perimeter control method***

  In this approach, a constraint on the perimeter of boundaries of the structure is introduced [43].The boundary perimeter of a discrete structure is formulated as:

$$P = \sum_{k=1}^{K} l_k \left(\sqrt{(\rho_i - \rho_j)^2 + \varepsilon^2} - \varepsilon \right) \tag{3.12}$$

  where l_k is the length of interface between adjacent elements i and j. The parameter ε is a small positive number that guarantees the differentiability of the perimeter.

- ***Mesh independent filtering***

The following intuitive rule for the modification of the sensitivity of the objective function is introduced by Sigmund [44]:

$$\frac{\partial \tilde{f}}{\partial \rho_k} = \rho_k^{-1} \frac{1}{\sum_{i=1}^{N} H_i} \sum_{i=1}^{N} H_i \rho_i \frac{\partial f}{\partial \rho_i} \tag{3.13}$$

in which the operator H_i is formulated as

$$H_i = r_{min} - dist(i,k), \quad i \in N | dist(i,k) \leq r_{min} \tag{3.14}$$

where r_{min} is a half of the predetermined minimum member diameter d_{min}, elements i and k are adjacent elements and $dist(i,k)$ denotes the distance between them. In this fashion, an element with low sensitivity obtains a much higher sensitivity after the modification if the sensitivities of elements within the zone of radius r_{min} of this element have higher values. This guarantees that wherever a member is formed during the optimization process, the radius of the member is in general not below r_{min}. An undesired effect of this method is that members in the final solution involve layers of elements with intermediate densities similar to the results of density slope control approach that is discussed below.

- ***Density slope control***

  As mentioned earlier, the reason for checkerboard solutions lies in the poor quality of the finite element formulation for problems involving highly discontinuous density variations. Based on this understanding, Petersson and Sigmund [45] introduced a constraint on the local gradient of the slope of element densities for guaranteeing the accuracy of the finite element formulation. This constraint was formulated for 2D structures with $n_x \cdot n_y$ regular mesh as follows:

$$|\rho_{j+1,k} - \rho_{jk}| \leq s \cdot h, \quad j = 1, ..., n_x - 1, \ k = 1, ..., n_y \tag{3.15}$$

$$|\rho_{j,k+1} - \rho_{jk}| \leq s \cdot h, \quad j = 1, ..., n_x, \ k = 1, ..., n_y - 1 \tag{3.16}$$

where subscripts j and k denote the element location in the coordinate system, s is the upper bound on the density slope and h denotes the mesh size. Under this formulation, the above mentioned authors proved the convergence of the finite element formulation. Numerical implementation for 2D structures was presented, where 2N linear constraints are involved and the optimization problem is solved by sequential linear programming. It was recommended that the parameter $s \cdot h$ should be less than 1/3 in order to guarantee a checkerboard free solution. Note that minimum member size control can be achieved by defining the lower bound of density slope according to preferred minimum member size r_{min}.

3.2.4.2 Checkerboard patterns

In [46], Diaz and Sigmund suggested that checkerboard patterns in layout optimization can be explained on the basis of local behaviour. In [46], it is shown that numerical approximations introduced by the finite element method may cause material arranged in a checkerboard fashion to appear artificially strong. When this happens checkerboard arrangements appear to be locally stronger than any other arrangement of two constituent materials, including a layered arrangement, and are a stable extremum of the strain energy density. Under such conditions checkerboard patterns are preferred in layout optimization problems seeking the stiffest structure.

Jog and Haber [47] presented a theoretical framework based on a linearized, incremental form of the problem and a patch test was proposed. They argued that spurious thickness modes can be detected by investigating the non-uniqueness of solutions to the discretized incremental equation system. Both works provide useful guidelines regarding choice of stable elements and they show that checkerboard patterns are prone to appear in both the homogenization and the SIMP approach.

Theoretical studies of the appearance of checkerboards in three-dimensional

problems have not yet been carried out. However numerical experience shows that checkerboards also appear for this case [48].

Several prevention schemes have been proposed, but they are almost all based on heuristics. They include:

- ***Smoothing***

  Having obtained the "optimal solution" (with checkerboards) the output picture is smoothed with image processing. This method ignores the underlying problem and should be avoided. Many commercial post-processing codes automatically use smoothing of the output images, so here precautions should be taken.

- ***Higher-order finite elements***

  Many papers suggest the use of higher-order finite elements for the displacement function u to avoid the checkerboard problem. In [46], it is shown that checkerboards are mostly prevented when using 8 or 9-node finite elements for the homogenization approach. For the SIMP approach, however, checkerboards are only prevented using 8 or 9-node elements if the penalization power is small enough (i.e. p should be smaller than 2.29 for a specific example in [46]). A drawback of using higher-order finite elements is the substantial increase in cpu-time.

- ***Patches***

  This technique effectively introduces a kind of superelement to the finite element formulation and has in a practical test shown to damp the appearance of checkerboards. However in topology optimization it does not remove them entirely.

- ***Restriction methods***

  They are essentially analogue to the three methods described as solution to prevent mesh-dependent solutions.

3.2.4.3 Local minima

Considering the many differing solutions to, for instance the MBB-beam problem, having appeared in literature, it is clear that topology optimization problems have extremely many local minima. To a large extent local minima appear for the nonrestricted 0-1 topology optimization problems. Restriction methods tend to convexify the problems and produce reproducible designs. Nevertheless, small variations in initial parameters such as move limits, geometry of design domains, number of elements, perimeter constraint value or filter parameter, etc., can result in drastic changes in the "optimal design". These problems are partly due to flatness of the objective function, but probably more importantly, due to the numerical optimization procedures used to solve the problems. Based on experience, it seems that continuation methods must be applied because, by construction, they take also "global" information into account and are thus more likely to ensure "global" convergence (or at least convergence to better designs).

The idea of continuation methods is to gradually change the optimization problem from an (artificial) convex problem to the original (nonconvex) design problem in a number of steps. In each step a gradient-based optimization algorithm is used until convergence. Different continuation procedures have been suggested.

For the perimeter constraint, Haber et al. [29] suggested a gradual raise in the penalization factor. For a low value of the penalization factor, the design problem resembles the variable thickness sheet problem which is convex. For increasing penalization factor the problem is expected to gradually converge to the desired 0-1 design.

For the mesh-independence filter Sigmund [49] suggested starting with a large value of the filter size r_{min} ensuring a convex solution and gradually to decrease it, to end up with a 0-1 design.

Tovar and Khandelwal [50] examined the continuation method and the conditions under which a gradient-based optimization algorithm converges to a global optimum in topology optimization, focusing on compliance problem.

In particular, they found that:

- Analytic solutions are restricted to problems of low dimension. For two design variables, the compliance function is convex for any value of p and the solution of the problem is unique. As the dimension of the problem increases, this study shows how the problem remains convex only for $p = 1$.

- For small enough problems, the binary global optimum can be found using an exhaustive search. This investigation considers problems with up to 32 design variables. Continuation was applied with a sufficiently small Δp. In every case, the solution converges to the global binary optimum. For the problems considered, a binary solution is obtained for $p \geq 5$.

- In problems involving hundreds or thousands of design variables, filtering followed by filtering reduction is to be implemented. After a certain small value, the end compliance value converges to a global minimum as the step Δp decreases, while for values of $\Delta p \leq 0.1$ the method is also algorithm independent.

These results support the conclusion that the continuation method is an efficient strategy to reach a global optimum.

3.2.5 Minimum member size control

From an engineering point of view, the mesh dependency of the design may not be as significant as the concern about manufacturability of the resulting topology. This means that a design engineer may not worry about the fact that different mesh densities may result in different final solutions. Instead, it may be more important for him to be able to control the size of members in the final topology, and therefore, the degree of simplicity of the design that can satisfy his manufacturing criteria. Besides manufacturing considerations, very thin members are unstable under compression.

The currently adopted *restriction methods* to prevent both *mesh dependence* and *checkerboard patterns* could be a good starting point to create an efficient control on minimum member size. However, they present several implementation drawbacks.

The perimeter control method is reasonably efficient in obtaining mesh independent results since only one additional constraint is introduced into the optimization problem. However, it is not easy to define the proper bound on the perimeter that leads to the desired simplicity of topology that reflects a specific manufacturing need. Therefore, many runs are, in general, needed, on a trial-and-error basis, to find the suitable perimeter bound value. Note also that although the perimeter bound tends to limit the number of members in the final solution independent of mesh density, it does not provide direct control on the minimum member size.

Except for its heuristic nature, the mesh independent filtering method has been shown to be extremely efficient for direct minimum member size control. However,numerical difficulties are expected when this method is applied to multiple constrained problems. The reason is that manipulation of sensitivity of constraints would significantly influence the quality of constraint approximation and hence makes it difficult to satisfy behaviour constraints during the iterative process.

The method based on local density slope control is obviously applicable to problems with multiple constraints. However, this method introduces 2N and 3N additional linear constraints into the optimization problem for 2D and 3D structures, respectively. This makes this approach computationally prohibitive for practical applications.

In [51],an algorithm based on constraining the slope of density is developed. For achieving a predetermined minimum member size of radius $r_{min} = d_{min}/2$,the slope constraint can be formulated for a general irregular finite element mesh as follows:

$$|\rho_i - \rho_k| \leq (1.0 - \rho_{min}) \frac{dist(i,k)}{r_{min}} \tag{3.17}$$

where $dist(i,k)$ denotes the distance between adjacent elements i and k, i.e. $k \in \Omega_i$ with Ω_i denoting the set of elements adjacent to element i. The symbolmin, whose default value is chosen as 0.1, represents the threshold that is interpreted as void in the final solution. This condition guarantees that whenever an element j reaches the density of 1.0, the member connected to this element has a diameter of at leastdmin. Note that the member size can be between $d_{min}/2$ and d_{min} if the element j is close to the boundary of the structure. This condition introduces $n \cdot N$, with n bigger than 2, additional linear constraints and makes the direct solution of this formulation computationally prohibitive. To overcome this barrier, a simple, yet extremely efficient technique is introduced in [51] to accommodate the above density slope constraints during the iterative process. The density slope constraints in Eq. 3.17 can be achieved through enforcement of adaptive lower bounds on the density as follows:

$$\rho_i \geq \max\left[\eta, \rho_j - (1.0 - \rho_{min})\,\frac{dist(i,k)}{r_{min}}\right] \tag{3.18}$$

where η is the lower limit of density and ρ_j is the density of element j at previous iteration that has the highest density among all elements that are adjacent to element i:

$$\rho_i = \max\left(\rho_k \mid k \in \Omega_i\right) \tag{3.19}$$

Note that no adaptive upper bounds except the absolute limit of 1.0 are needed for achieving the density slope constraints described in Eq. 3.17. The possible large violation of density slope constraints of element i due to increases of densities of its adjacent elements will be corrected in the forthcoming iteration by updating the lower bounds on the basis of Eq. 3.18. This way, the computationally prohibitive linear constraints in Eq. 3.17 are accommodated with adjustments of the side constraints of design variables. It is easy to see that except the negligible computation associated with the adjustment of the side constraints of design variables on the basis of Eq.

3.18, no extra computational effort is needed.

As has been previously pointed out, a phenomenon of the results under the slope control approach is that the members of the final solution represents a tapered density distribution that decreases from 1.0 in the middle of a member to 0.0 on the boundary of the member. This is highly undesirable, especially for problems with behaviour constraints since, under the penalization formulation, the constraint values are highly artificial when semi dense elements exist extensively. To avoid this undesirable effect, the following iterative scheme is implemented:

1. the iteration under the density slope control in Eq. 3.17 is performed for the given penalty parameter ($p_0 = 2.0$ for plate and shell structures and $p = 3.0$ for solids as default).

2. after the convergence of phase 1, the same problem is performed with an increased penalty of $p = p_0 + 1.0$ for insuring a clear member definition.

3. then the density slope constraints on the boundary of members formed during the phases 1 and 2 are relaxed so that the solution can achieve a clear 0/1 material distribution.

It is reasonably easy to identify elements on the boundaries of members for plate and shell structures whereas more dedicated rules have to be developed for 3D solids. The above procedure is implemented in the *Altair OptiStuct Release 3.5*.

3.2.6 Optimization Procedure

When the number of design variables is very large, gradient based optimization methods are the most efficient algorithms.

The classical optimizer used in TO is the Optimality Criteria (OC) [52, 53], based on a bi-section method. While being formulated for single-objective and single-constraint problems, OC was extended to multiple-constraints optimization problems [54].

As shown in [34], the MMA is one of the most suitable optimizers which could substitute the Optimality Criteria adopted in the 88-line code by Sigmund [55], in order to accelerate convergence in linear and non-linear problems. It constitutes the generalization of different algorithms. In *Optistruct*, the base optimizer is an industrial implementation of CONLIN. In the following, the construction of such algoritm is analyzed in detail.

3.2.6.1 Approximation approach

In the approximation concepts approach, the primary optimization problem is replaced with a sequence of explicit sub-problems having a simple algebraic structure. Each sub-problem is generated through Taylor series expansion of the objective function and constraints in terms of intermediate linearization variables. For example, linearization of the constraints with respect to reciprocal variables is a well recognized technique to solve optimal sizing problems. There is an intuitive explanation for the success of this technique, in that stresses and displacements are exact linear functions of the reciprocal sizing variables in the case of a statically determinate structure. For shape optimal design problems, there is no such physical guideline for the selection of intermediate linearization variables. Nevertheless, this change of variables continues to have a highly beneficial effect on the convergence properties of the shape optimization process [56]. .

A very attractive feature of the approximation concepts approach is that it replaces the primary optimization problem with a sequence of separable sub-problems which can be efficiently solved by a dual method formulation. In the dual approach, the constrained primal minimization problem is replaced by maximizing a quasi-unconstrained dual function depending only on the Lagrangian multi- pliers associated with the linearized constraints. These multipliers are the dual variables subject to simple non- negativity constraints. The efficiency of the dual formulation is due to the fact that maximization is performed in the dual space, whose dimensionality is relatively low and depends on the number of active constraints at design iteration.

3.2.6.2 Dual method approach

In the convex linearization method, the initial problem is transformed into a sequence of explicit sub-problems having a simple algebraic structure. Furthermore each sub- problem is convex and separable. These properties make it attractive to solve the sub-problem by using dual algorithms. The dual method approach is well-known and quite respected in the mathematical programming community (Lasdon 1970, pp. 396-459; Lootsma 1989). The solution of the primal problem can be obtained by the following "Max-Min" two-phase procedure:

$$\begin{cases} \max & l(r) \\ s.t.: & r_j \geq 0 \end{cases} \tag{3.20}$$

where the dual function $l(r)$ results from minimizing the Lagrangian function:

$$L(x,r) = \sum_{j=0}^{m} r_j \left(\sum_{+} c_{ij} x_i - \sum_{-} c_{ij} x_i - \overline{c}_j \right) \tag{3.21}$$

over the acceptable primal variables

$$l(r) = \min_{\underline{x}_i \leq x_i \leq \overline{x}_i} L(x,r) \tag{3.22}$$

The separability of the primal problem implies that the Lagrangian function in Eq. 3.21 can be written as the sum of n individual functions $L_i(x_i)$, and therefore, the n-dimensional minimum problem in Eq. 3.22 can be split into n single variable minimization problems.

A fundamental property of the dual function is that its first derivatives are simply given by the primal constraint values. In addition, because the dual problem is fully explicit and because the corresponding primal problem exhibits a relatively simple algebraic form, the second derivatives of the dual function can be written in closed form.

3.2.6.3 Convex Linearization Method (CONLIN)

The convex linearization method (CONLIN) [57] was initially conceived as an extension to the approximation concepts approach. The key idea in the CONLIN method is to perform the linearization process with respect to mixed variables, either direct or reciprocal, independently for each function involved in the optimization problem. At each successive iteration point, the CONLIN method only requires evaluation of the objective and constraint functions and their first derivatives with respect to the design variables. The optimizer will then select by itself an appropriate approximation scheme on the basis of the signs of the derivatives. This constitutes a major improvement with respect to the regular approximation concept approach, where it is usually assumed that the objective function is linear in the direct variables (e.g. structural weight) and that the constraints can be accurately approximated as linear functions of the reciprocal variables (e.g. stresses and displacements). Furthermore, the CONLIN optimizer has an inherent tendency to generate a sequence of steadily improving feasible designs, in contrast with the previously developed approximation concept approach using dual methods [58]. Finally, it is relatively straightforward to equip CONLIN with a built-in strategy for dealing with highly infeasible starting points, by uniformly relaxing the violated behavior constraints.

The CONLIN method proceeds by linearizing each function defining the optimum design problem with respect to a properly selected mix of direct and reciprocal variables, so that a convex and separable subproblem is generated. The selection of the "intermediate" linearization variables is made on the basis of the signs of the first partial derivatives. It is easily proven that, considering any differentiable function $c(x)$, the following linearization scheme yields a convex approximation (hence the term "convex linearization"):

$$c(x) = c(x^0) + \sum_{+} c_i^0 (x_i - x_i^0) - \sum_{-} (x_i^0)^2 c_i^0 \left(\frac{1}{x_i} - \frac{1}{x_0} \right) \tag{3.23}$$

where c_i denote the first derivatives of $c(x)$ with respect to the design variables x_i. The symbol $\sum_+$ ($\sum_-$) means "summation over the terms for which c_i is positive (negative)". One of the most interesting features of the convex linearization scheme is that it also leads to the most conservative approximation amongst all the possible combinations of mixed direct/reciprocal variables.

As stated for dual method approaches, hessian function can be expressed in closed form [59], through:

$$H_{jk} = -\frac{1}{2} \sum_{i \in I} n_{ij} n_{jk} \frac{x_i}{a_i} \tag{3.24}$$

where $a_i = \sum_+ c_{ij} r_j \geq 0$ and

$$n_{ij} = \begin{cases} c_{ij} \text{ if } c_{ij} > 0 \\ \frac{c_{ij}}{x_i^2} \text{ if } c_{ij} < 0 \end{cases}$$

It is important to emphasize that the summation is restricted to the free primal variables, i.e. the variables x i which do not reach their lower or upper bound. This means that the second derivatives of the dual function are discontinuous whenever a free primal variable becomes fixed, or conversely. The fundamental difficulty in using Newton type methods for solving the dual problem resides in these inherent discontinuities of the Hessian matrix. Fortunately, the topology of the dual space can be described in an exact mathematical way via the concept of second order discontinuity planes [58, 60, 61]. Based on this concept, a very reliable sequential quadratic programming method has been devised to solve the dual problem [59].

In the new version of the second order dual optimizer, no line search is

required, and the Hessian matrix H is allowed to be occasionally singular. Instead of using the Newton method, the dual problem is transformed into a sequence of quadratic sub-problems. Each quadratic sub-problem can be readily solved by using, for example, a simple conjugate gradient method with non-negativity constraints on the dual variables. Because each quadratic sub-problem is restricted to the current dual subspace, its dimensionality is usually small, and the maximization process is quite fast. Clearly, in this approach the Hessian matrix no longer needs to be inverted (it can, in fact, be occasionally singular), and no line search process is necessary. The main change is therefore to replace the basic generalized Newton iteration in DUAL-2 with the solution of the equivalent quadratic sub-problem. However, in order to prevent the instability of convergence that might occur because of the second order discontinuities, additional modifications were found to be necessary, namely to the treatment of side constraints and relaxation. In particular, the latter is necessary because of the conservative character of the CONLIN approach, that could create an approximate feasible domain which is empty, especially when the initial starting point is seriously infeasible: this feature makes CONLIN algorithm adapted to solve TO problems with highly infeasible starting points.

Further details, as well as the complete algorithm, can be found in [59].

3.2.7 Optimality Conditions

The solution is said to have reached convergence when the first order Karush Kuhn Tucker (KKT) conditions are satisfied to a given tolerance. In alternative, a criterion based on the norm of the variation of the solution or on the number of iterations can be adopted.

3.3 Previous Studies on Airframe Topology Optimization

The present work is part of a larger research project in Airbus Operations SAS. It is developed around an entire PhD entitled *Propulsion Airframe Topology Optimization with performance and stress criteria using Eulerian and Lagrangian approaches*, conducted by Simone Coniglio.

Another study, analogue to the present one, was performed in 2018 in Airbus Operations SAS by the intern Martin Vlashi. He analysed two design spaces which are similar to the ones which will be treated in the present work:

- CLS Structure (small design space): it includes mainly the front secondary structure and the upper bi-fi. It is delimited by the upper spar of the pylon (internally) and the aerodynamic surfaces (externally). The Topology Optimization problems which are treated regard the minimization of tip clearance and OGV stress.

- Disruptive PPS architecture (large design space): this includes the previous design space, pylon, fan case, nacelle and lower bi-fi. The Topology Optimization problems which are treated regard the minimization of compliance and tip clearance.

A complete description of both design spaces and their interactions is given in Chapter 4.

In Figure 3.2, the obtained topologies for the small design space are illustrated. From the mentioned results, one can conclude that:

- There is no guarantee that the solution found is the global optimum nor if there are any more feasible design with comparable trades. The solution can be improved or not in a redesign starting from the topology. For this reason, the gain obtained is probably not the best.

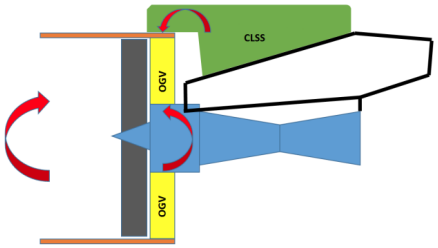

(a) a

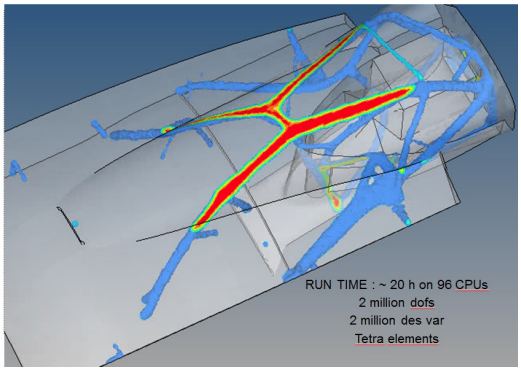

(b) b

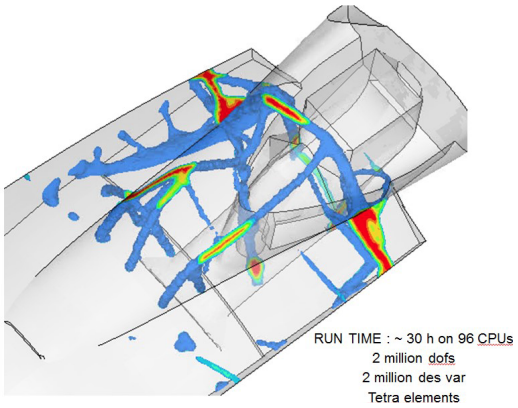

(c) c

Figure 3.2: Small design space (a) and optimised topology with respect to the tip clearance (b) and OGV stress minimization (c)

- A CLS structure that reduces OGV loads reduces also TC and viceversa.

- A CLS structure that reduces OGV loads or TC also reduces other engine performance criteria.

With respect the second design space, the first results show that a reduction is possible (see Figure 3.3). The results obtained from the two optimization problems are depicted in Figure 3.4.

With respect to the compliance minimization problem, some conclusions have been identified:

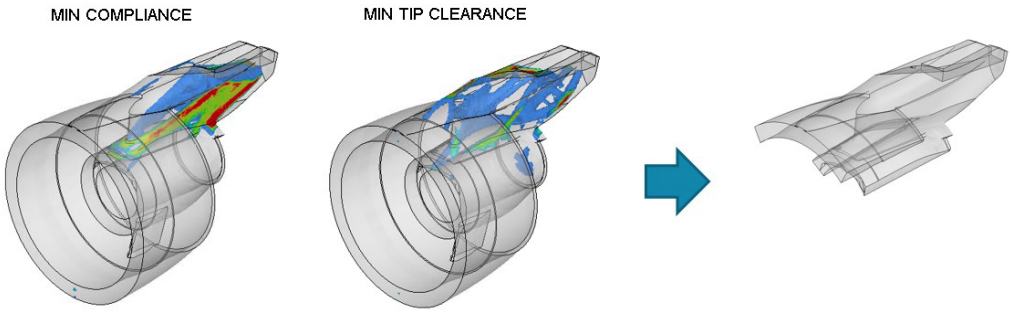

Figure 3.3: First optimization results from the large design space

- the pylon has two lateral panels that resist to bending.
- The pylon has some cowl load sharing on the upper part of the fan case.
- The pylon is almost symmetric, indicating that the asymmetry of the design volume and the asymmetric load cases are not very relevant to the result.
- The pylon is not a box, because part of the torque Mx passes through the engine and then through the rear mounts. This differs from the present design were Mx is recovered at the front mount. This difference arises from the different hypotheses of rear mount interface
- Upper and lower spar and thrust links are replaced by a trussed structure on the plane going from the front mount and the spigot. This structure transfers part of the thrust.
- The front mount has a quite complex shape which should be studied more in detail for understanding, but surely it takes thrust, bending and torque.
- The distance between the lateral panels is maximized.

On the other hand, looking at the tip clearance minimization problem, the author affirmed that:

- Non-symmetrical and very important cowl load sharing. It is clear that a tip clearance solution will focus on CLS.

- There are no traditional elements of the pylon: upper spar, laterl panels, thrust links are replaced by a complex structure not easy to interpret at first glance. For interpretation of the results, a deeper study on load paths is needed.

- The topology found in this case cannot correspond to a real pylon because the limit load cases are not considered, neglecting many points of the flight envelope.

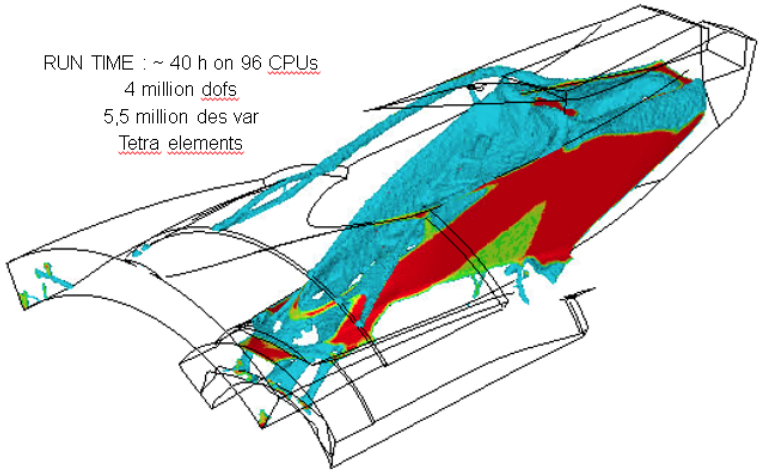

(a) a

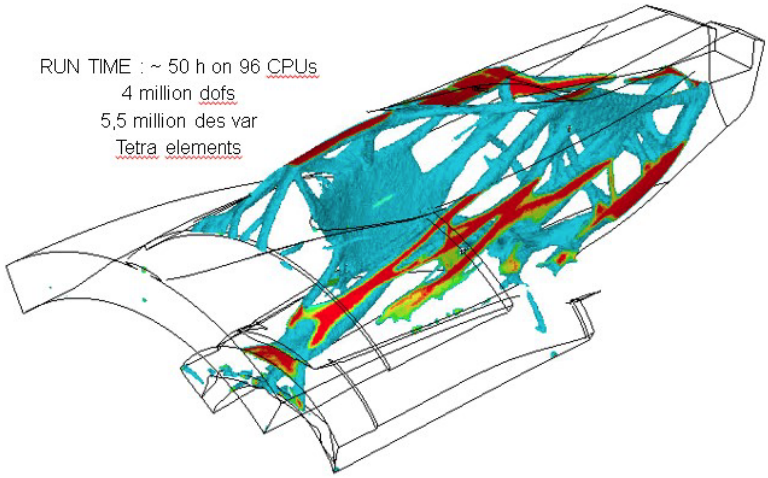

(b) b

Figure 3.4: Optimised topologies with respect to the compliance (a) and tip clearance (b) minimization (large design space)

Chapter 4

Problem Statement

In this chapter, the Engineering problem is presented. In Section 4.1, the industrial reasons behind the study are introduced. In Section 4.2, Design Space is defined. In Section 4.3, interfaces with the non-design region are described. In Section 4.4, we find the Load Cases (LCs) adopted in optimization process. In Section 4.5, material choice is outlined. Then, aerodynamic, structural and all other requirements are detailed in Section 4.6.

4.1 Industrial Needs

The UHBR is a leap in technology. Some problems cannot be forecasted in time when developing a new type of design. For example, in our case a problem that could come out is the excessive load in the fan OGV (outlet guide vane) blades. Being the size and the weight of this engine unprecedented, this is actually not a surprising problem. The sizing of the OGV is limited by the aerodynamic shape constraint, in particular when it comes to their thickness and section shape. Also, a resizing of the OGV blades would add some mass. If another solution which is less expensive in terms of mass can be found it is welcome.

The amount of load passed through the OGV is then dependent, speaking simply, on the relative stiffness between OGV and CLSS. This is an oversim-

plification which could help to understand the concept. A solution could be, together with adding a CLSS, to soften the OGV, in order to reduce passing loads. This is viable but requires knowledge in OGV sizing.

4.2 Design Space Definition

In the present intern, two design spaces have been considered:

- CLS Structure (small design space);
- Disruptive PPS Architecture (large design space).

Since the actual objective is a long term project aiming to re-design the pylon and the nacelle, only the second design space is presented and analysed.

This design space covers the following regions:

- fan case: this is front delimited by the extremity of the fixed beams of the TRU, while the rear boundary is an arbitrary surface created between the rear extermity of the OFS and the rear section of the fan case itself;
- front secondary structure (FSS): this constitutes the direct link between fan cowl and the pylon;
- pylon: the boundaries are the aerodynamic surfaces defined by the secondary structure (behind), the bifurcation of the secondary flux (in front) and the OFS (on top), the interface with the wing (behind, on top), the fixed beams of the TRU (laterally) and the IFS (at the bottom);
- IFS region: it is the surface surrounding the original IFS;
- front mount ring: it includes the interface between pylon and IFS, and it is identified as the ring included in the TBS (in front), the engine core (internally) and the IFS (externally);

- rear mount ring: delimited by the front and rear sections of the mount ring on the LPT stator, the mount ring itself (internally) and the aerodynamic surfaces describing the mobile part of the TRU;

- lower bi-fi: the boundaries are constituted by the fixed TRU (on the bottom), the aerodynamic surfaces describing the bifurcation of the secondary flux (in front, behind and laterally) and the IFS (on top);

- fixed TRU: this is entirely delimited by the extremity of the fixed beams of the TRU.

We have to underline the presence of keep-out zones in the engine: these are constituted by regions where there is no possibility to arrange the primary structure, in order to avoid the loss of fundamentals in case of Fan Blade Out (FBO). This is a key-feature which has been ignored in the previous internship discussed in the previous chapter. The design space is presented in Figure 4.1.

4.3 Boundary Conditions

The rear upper spar of the pylon is tied to the wing: this constitutes the only interface with external structures.

Internally, there is a number of interfaces between the design space and the internal engine systems and structures:

- the fan case region and the front side of the FSS are glued to the fan cowl, covering a cylindrical surface surrounding the OGVs;

- the FSS and the fixed TRU are connected to the external surfaces of the fixed beams of TRU;

- IFS region and front mount ring are glued to the IFS itself and the engine;

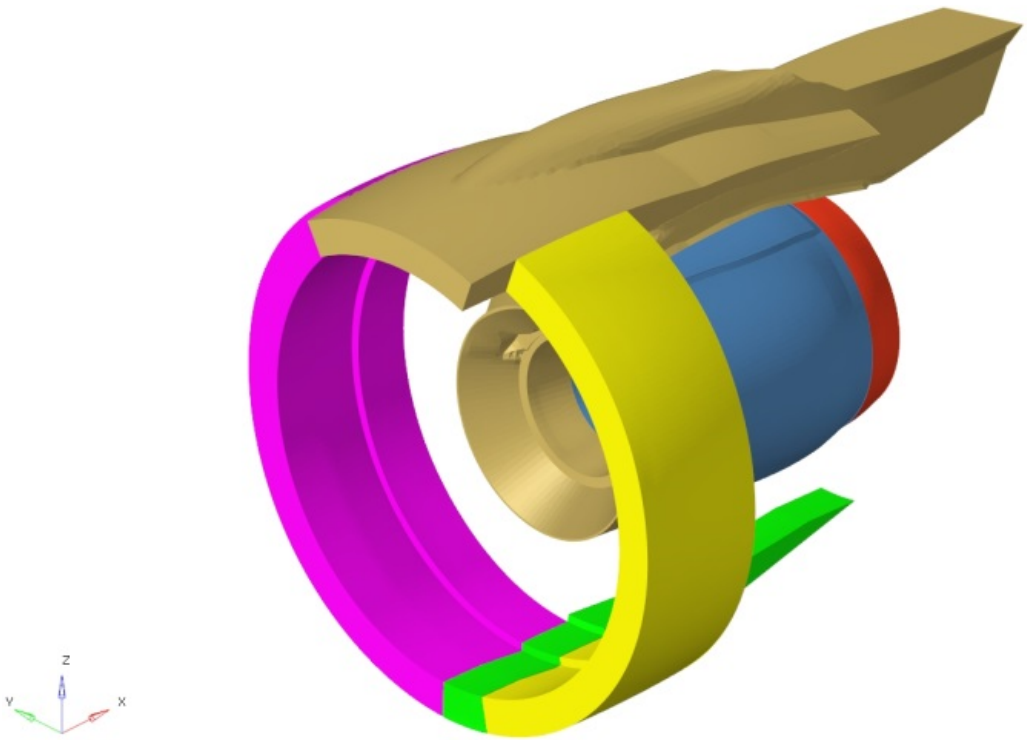

Figure 4.1: Model of the Design Space: isometric view

- front and rear mount ring regions are glued respectively to TBS and rear mount ring and the engine;
- the lower bi-fi and pylon regions are glued to the correspondent bi-fis in front and the engine;
- FSS, pylon, TRU and fan case are glued to the external and internal skins of the OFS.

4.4 Load Cases

The loads applied on the Integrated Finite Element Model (IFEM) can be distinguished into five categories:

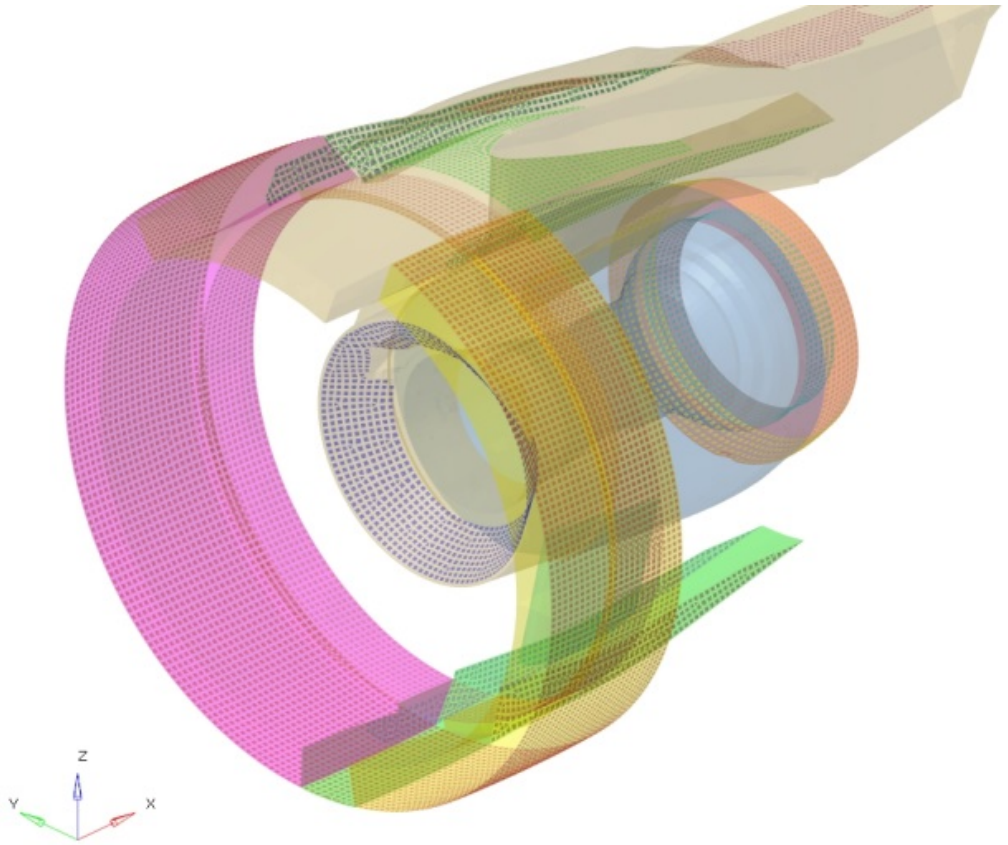

Figure 4.2: Model of the Design Space: interfaces

- Inertial acceleration loads in X, Y and Z direction: they correspond to the load factors nx, ny and nz experienced by the power plant system.
- Aerodynamic loads on the nacelle and fan case: these are due to external and internal flows.
- Thrust from each stage applied on the shaft axis.
- Torque from each stage applied on the shaft axis and stator casing.

The different load cases are combinations of these loads. They are identified in a wide range of flight conditions. In particular:

CONF.	CATEGORY	ID	LOAD CASE NAME	TSFC	Mx (Nm)	MBEND (Nm)
Stow	Fatigue	1050				
Stow	Fatigue	1052				
Stow	Fatigue	1055				
Stow	Fatigue	1056				
Stow	Limit	2001				
Stow	Limit	2004				
Stow	Limit	2005				
Stow	Limit	2007				
Stow	Limit	2008				
Stow	Limit	2009				
Stow	Limit	2012				
Stow	Limit	2014				
Stow	Limit	2017				
Stow	Limit	2018				
Stow	Limit	2019				
Stow	Limit	2040				
Reverse	Fatigue	1193				
Reverse	Limit	2192				

Table 4.1: Available Load cases in IFEM with TRU Shutter

- limit Load Cases (LCs) correspond to extreme load conditions of the envelope diagram;

- fatigue LCs represent flight conditions actually present all along aircraft life.

4.5 Material

The material chosen for the structure is Titanium. Only the linear properties of titanium have been used so the actual Alloy is not specified. The choice of material influences the volume fraction which corresponds to a given value of mass. For Titanium we would get 0.005, 0.01 and 0.015 as typical volume fractions, while for aluminum we would get almost the double.

The specific stiffnesses of Al and Ti are close, so the choice is not influential for the scope of this optimization. The choice of a less dense metal also makes the optimization easier since it corresponds to higher volume fractions.

In order to avoid small volume fraction, it's common to use a degraded

material. Such a material would have, for example, half the density and half the Young modulus, thus, the desired specific stiffness, but double the volume.

In the present study, degraded Ti is chosen as material for the DS: it will have half Young Modulus and half density of the real Titanium.

4.6 Specific Requirements

Like any other engineer project, some requirements must be matched. In the following, aerodynamic, structural, configuration and other constraints are explained.

4.6.1 Tip Clearance

In our model thermal expansion effects, centrifugal forces and pressurization of stator case are not studied. These effects are well understood by the engine manufacturer, and they are independent of the engine integration on the plane. Only shaft flexion and stator casing deformation will be considered. Figure 6 shows the effect of engine structure deformation on tip clearances.

4.6.2 Structural Performances

Despite the possibility of adopting the relaxation/aggregation methods (illustrated in the previous chapter) on the stress constraints, the number of responses required to compute the maximum is unvaried (an equivalent Von-Mises stress for each Gauss point in the mesh), leading to a very huge memory consumption. Hence, another approach is used in the present work. Every load applied to the OGV is recovered, although just the resultant moment is considered as actual constraint.

In previous internship (the results of which have been described in Section 2.3), stress constraints were used while monitoring at the same time the OGC loads, leading to an excessive computational time.

4.6.3 Multi Model Optimization (MMO)

A significant advance in this project with respect to the previous one (in 2018) is given by the introduction of a double IFEM Model of the Engine itself: this is furnished in Stow and Reverse configuration.

This is not reflected only on the presence of different load cases, but also in two distinct configurations of the components themselves. In particular, in Reverse configuration the TRU is fully deployed.

The need for a double model comes from the seek for an optimal architecture which would take into account all main load conditions all along aircraft life.

Chapter 5

Methodology

In this Chapter, the fundamental aspects of the methodology adopted in the present work are presented. Section 5.1 defines the software adopted in the study. In Section 5.2 main assumptions of the model are discussed. In Sections 5.3-5.4 we introduce the modeling strategies to compute tip clearance and OGV loads respectively. In Section 5.5 a balance on constraint modeling computational cost is detailed. Section 5.6 describes the tips to implement Multi-Model Optimization in the adopted software. Finally, mathematical formulations of the chosen problems are formalized in 5.7, together with the general strategy to the current study.

5.1 Software Environment

The aerodynamic surfaces have been created in *CATIA* environment. Other Finite Element Models have been created in Airbus Operations SAS through the sotware *Hypermesh*.

The whole pre and post-processing are effectuated respectively in *Hypermesh* and *HyperView*, while the analysis itself is left to *Optistruct*.

5.2 Main Assumptions

The chosen material is considered as perfectly isotropic, while the whole structure is supposed to follow a linear behaviour, under the fundamental hypothesis of small displacements. The Finite Elements Model will also be composed by first-order solid (*TETRA4* and *PYRA5*) and shell elements (*TRIA3* and *QUAD4*).

The total amount of Finite Elements used to discretize the whole Design Space has to respect the constraints on available memory on the CPUs. Hence, the size of each element cannot be lower than certain limits. Moreover, since the solution could be mesh-dependent, the homogeneity of the relative sizes has to be guaranteed, leading us to the choice of the interval between 0.96 and 1.04 times the average mesh size of the non-design region. Overall, there are 1296207 design variables and 2083071 degrees of freedom.

Particular attention has to be paid to the interfaces between the design space and the loaded aerodynamic surfaces (corresponding here to the internal and external skins of the engine itself). Given the limits underlined before, reduced stiffeners cannot be obtained through a conventional solution. Hence, shell elements must be added to boundary regions: instead of material density, thickness will be the design variable used in such elements. In order to obtain a realistic path of the stiffeners, the 2D mesh has to be much more refined than the boundaries of the 3D mesh on the correspondent surface. This is another key-feature which has been ignored in the previous internship, the results of which have been described in Section 3.3.

With respect to the Boundary Conditions, we have supposed that all the interfaces defined in the previous chapter can be considered as glued. The only exception is the rear mount ring interface, where we suppose the possibility of relative movement in the axial direction: this would allow thermal engine deformation without damaging the structure itself.

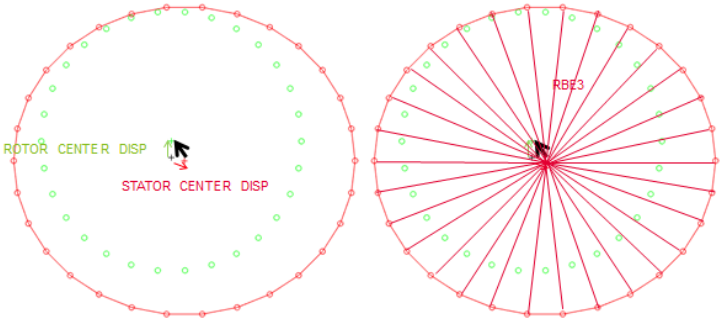

Figure 5.1: Tip Clearance Modeling in Optistruct

5.3 Tip Clearance Computation

The implementation in Optistruct of the Tip Clearance can be done using, for each stage, an RBE3 element with master a node on the shaft and as slaves all the nodes on the stator wall of the stage. In practice, there is no node in the model representing the centre of the casing. To get this information, we create a RBE3 element between a node initially situated on the centreline and the nodes on the casing structure. The slave node's displacement is therefore a weighted average of the master nodes' displacements. In our case, all nodes on the casing contribute with the same unitary weight to the slave node's displacement. This method does not allow us to take into account the exact deformed shape of the casing, but an average global displacement of it, depending on local nodal displacements. The slave node is placed on the exact x coordinate of the stage (engine coordinate system). Because the shaft is already quite finely meshed, we do not add extra nodes at the exact coordinate of the stage to compute the shaft displacement but we take the closest existing node. The difference between the exact coordinate and the considered node 's coordinate is usually less than 1 mm, and reach around 5 mm for the Fan and the 6th HP stage. This small variation is marginal and will not significantly impact the results.

To get the relative displacement, we started by outputting the Y and Z displacement of the shaft node and casing node (X being the shaft axis, the

displacement on the X axis does not play a part in eccentricity). This latter is computed through the following formula:

$$c_1 = \sqrt{(u_{master} - u_{slave})^2 + (v_{master} - v_{slave})^2}$$

where u and v represent the displacement respectively on the axis x and y. Thus, the total number of DRESP used in the previous project (2018) was 5 per stage:

- 4 DRESP1 for the displacements of the 2 nodes;
- 1 DRESP2 to compute the above formula.

Tip clearance computation was simplified by considering only the eccentricity contribution. In order to reduce even more the number of DRESP, only the stages that contribute the most to tip clearance were taken into account. Choosing the 10 most relevant stages it can be reported, for the baseline design, an error of around 10%. This assumption was made basing on the fact that, with an optimization, the design can choose configurations where the simplified tip clearance is easier to optimize that the real criteria considering all stages. Moreover, it is not guaranteed that this error will stay the same in the case we add a supplementary structure. Because of both computational cost and lack of precision, we abandoned this strategy.

In the actual project, in order to improve the run efficiency, we reduced the number of responses requested by adding a third node, called delta node, which displacement is directly the relative displacement of the 2 previously considered nodes. To do so, we first need to create the delta node for each stage, we create it on the exact stage coordinate (so it is superimposed with the casing RBE3 slave node) and we block its translation on X and the three rotations. Then, we define for each stage two MPCs (Multi-Point Constraints) that will impose to the delta node the relative displacement. A MPC is a sum of weighed displacements, in our case, all component of the equation have a unitary weight. For each stage, the MPCs set the following equations:

We can then output directly the total translation of the grid node, as we ensure its X component would be null with boundary conditions, and the Y and Z component are directly the relative displacement between shaft and casing. With this definition, we reduced the number of requested response per stage to only 1. Knowing there is 21 stages of compressor and turbines on the studied engine, we require 21 outputs to get a full appreciation of our structure effect on tip clearances.

Though, it is not convenient to have 21 values to look at to appreciate the optimization effect on tip clearances. Moreover, the final purpose of the study is to minimize fuel consumption, and if tip clearances surely affect it, it does not have the same impact at each stage of the engine. Therefore, it is convenient and more accurate to compute a global value from the 21 stages that would give an appreciation of the structure performances regarding fuel consumption. To do so, we introduce a simplified expression of Thrust Specific Fuel Consumption (TSFC). TSFC is expressed in grams of fuel per second-kilonewton (gs-1kN-1) and represents the mass of fuel needed to provide 1 kN of thrust for a period of time of 1 s. A lot of parameters impact the TSFC, including tip clearances. The relationship between tip clearances and TSFC is very complex and is the engine manufacturer knowledge. Nevertheless, we can use a simplified model, using only the 21 responses we computed and several trade factors to get an idea of ipact over TSFC due to tip clearances.

The first thing to do before applying the trade factors in to weight each stage's tip clearance output value with the blade length of the stage. The stages can be of very different sizes: the fan blade length can be more than 50 times the shortest HPC stage's one. The tip clearances may then not be of the same order of magnitude from one stage to the other. To be able to compare the tip clearances on each stage, we then use to weight them with the blade lengths.

Then, computing the variation of TSFC due to tip clearances will only use one DRESP2, which is not very expensive in terms of calculation, to

compute the following equation:

$$\Delta TSFC = \sum_{c} \left(\sum_{s=1}^{n} \frac{TC_{c,s} k_{c,s}}{L_{c,s}} \right) \tag{5.1}$$

With:

- c : considered component (Fan, IPC, HPC, HPT, IPT)
- n : Number of stages in the component
- s : considered stage
- TC/L : weighted tip clearances output with previous DRESP2
- k : Exchange rate of considered component stage.

5.4 OGV Loads modeling

The torque moment in the following is, in our case and if not specified, always considered in the OGV load. Integrating the computation of the load on each OGV would take at least 240 DRESP for each load case (for a total of 800 DRESP per load case). Furthermore, the design of the OGV blade is not fixed and can still change: in particular the blades could be different from one another. Therefore it is not important to take into account the load on a single blade but the resultant.

Because they are long blades, especially in the case of UHBR power plants, OGVs can be subjected to important efforts that can be reduced by an appropriate nacelle and pylon design. This is therefore an important parameter to consider for our optimization. Though it requires some important changes in the initial model to output the wanted responses.

In the previous internship, the stress in the OGV has been considered and not the load. This is not a very reliable parameter to monitor, as it can locally vary, show some singularities we cannot easily understand, and

is inconvenient and expensive to set as optimization constraint or objective. The loads had not been previously considered as the implementation in the previous model where introducing software errors that had not been solved even with Altair support. In the latest version of the WEM on which the present study is focused, the set-up between the OGVs and the fan case, through which the loads are passing, has changed. Therefore, this set-up needed some modifications in order to get resultant forces and moments of all OGVs.

There is 40 OGV blades and each of them has 4 rigid connections RBE3 at the end that are connected to RBE3 on the fan case to model the ties. The initial set-up link each OGV RBE3 to the corresponding fan case RBE3 with spring elements (CELAS2) and a rigid element (RBAR). All this assembly, from node A to B is superimposed at one geometrical point.

In order to get the resultant forces and moments of all OGV, we need to gather the 160 efforts of each RBE3 couples at one node. Otherwise, we would have to output every element forces, so 160*6=960 responses, and then post process them to get the relative efforts and transport the moments on a single point, which would be extremely expensive in calculation and post processing time. To get the resultant, a totalizer node is created on the axis of the engine, clamped in all 6 d.o.f.s, and the set-up between the casing and the OGVs is modified (so that efforts would transit through that node).

The RBAR elements connecting each side on the initial set-up were replaced by RBE2 between the nodes C/D and nodes C*/D*, geometrically superimposed with the totalizer. Then, several MPCs (multi-points constraints) between nodes C*, D* and T (totalizer) were to be introduced to impose the relative displacement of C* and D* to the totalizer in all directions for all 160 OGV/casing interface nodes. Because the totalizer is clamped, instead of getting displacement resulting from the 160 local displacements at the interface, we will get a reaction force being the resultant of all the forces applied at the interface on the OGV from the fan case.

The spring elements between nodes A/B and C/D are kept because of

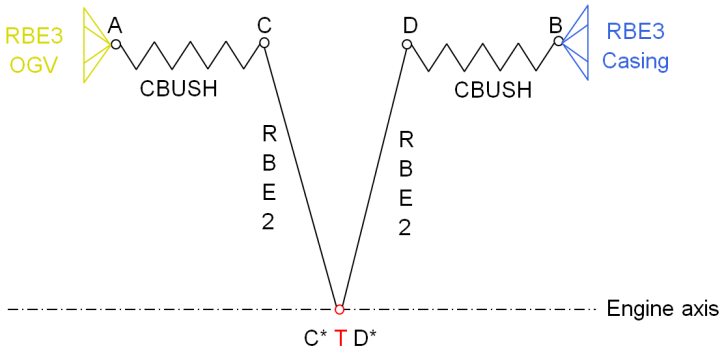

Figure 5.2: OGV assembly: modified set-up

master slave incompatibilities between RBE2 and RBE3 elements. Nodes A and B being slave of the RBE3, they cannot be also slave of RBE2, and C* and D* being involved in MPCs cannot be slaves of RBE2. The RBE2 should have, in fact, 2 master nodes, which is impossible. This is why we deport the RBE2 slave nodes from A and B to C and D with a CBUSH. As we want rigid connection though, very high rigidity values are necessary, as prescribed by IFEM Protocol: 10^8 for translational d.o.f.s and 10^{11} for rotational d.o.f.s.

With this configuration, we only need to output 6 DRESP1 of the forces in the totalizer grid to get the resultant of efforts passing through the OGVs. As the critical efforts for the engine operations are only the bending moment and to a lesser degree the torque, we actually do not need 6 responses. We output only the three moments using DRESP1 and set a DRESP2 to get the bending moment, resultant of My and Mz. The total number of responses for the OGV load is therefore 4.

5.5 Constraints modeling

The torque moment in the following is, in our case and if not specified, always considered in the OGV load. Integrating the computation of the load on each OGV would take at least 240 DRESP for each load case (for a total of 800

DRESP per load case). Furthermore, the design of the OGV blade is not fixed and can still change: in particular the blades could be different from one another. Therefore it is not important to take into account the load on a single blade but the resultant.

It is interesting to compare the total number of responses output in projects presented in 2018 and 2019. The number of output responses could have been even more reduced, for example by choosing only a pertinent sample of rotor stages to study for tip clearances, as it has been finally done last year by Martin, who only studied 10 stages. Below is a recapitulative and comparative table of 2018 and 2019 responses, we see that the number has been drastically decreased due to a focus on less parameters and a more efficient way to output the responses.

Parameter	Number of output responses in previous project	Number of output responses in current project
Tip Clearances	40 DRESP1 + 10 DRESP2	21 DRESP1
TSFC variation	1 DRESP2	1 DRESP2
Moments in OGV	Not studied implementation issues	3 DRESP1 + 1 DRESP2
Stress in OGV	1 DRESP1	Not studied Moments instead

Table 5.1: Balance on adopted responses

5.6 MMO Implementation

To model the presence of a double model representing the Stow and Reverse configuration, a single modification on the Coordinate systems of the joins between fixed and mobile part is needed. Being that the Design Space is only connected to the fixed part of the engine, no different configurations are required. However, all the optimizations must take into account the different models, creating two different stiffness matrices. The algorithm performing the computations cannot include any symmetry pattern within a single design variable card (DTPL), since a projection method is used to pass from a model to the other. Instead, to create such a symmetry, different DTPL cards have to be written: one will be the master and the other the slave variable, following a linear pattern along with the y-axis (local cartesian

engine coordinate system). The same procedure is valid for SHELL and SOLID elements.

5.7 Analysis Procedure

In the present work, different scenarios will be presented and studied.

The internship is divided into two parts, devoted to two variations of the global design space:

- CLS structure (assigned to Philippine Hindre), including only the cradle (intended as a link between the pylon and the fan cowl);
- Disruptive PPS Architecture (assigned to Gabriele Capasso), including the whole domain described in the previous chapter.

Focusing on second half of the internship, several analysis are performed in order to find the best mathematical formulation to optimize such a structure.

Firstly, three TO problems in Stow Configuration engine model are solved. They can be formalized as follows:

$$\begin{cases} \min & \max_{i \in I} C(\rho, U_f(\rho)) \\ s.t.: & V(\rho) \leq V_0 \\ & 0 < \rho_{min} \leq \rho_k \leq 1 \quad \forall k \in T_k \end{cases} \tag{5.2}$$

$$\begin{cases} \min & \max_{i \in I} C(\rho, U_f(\rho)) \\ s.t.: & V(\rho) \leq V_0 \\ & TSFC \leq TSFC_0 \quad \forall j \in J_1 \\ & 0 < \rho_{min} \leq \rho_k \leq 1 \quad \forall k \in T_k \end{cases} \tag{5.3}$$

$$\begin{cases} \min & \max_{i \in J_1} TSFC(U_f(\rho)) \\ s.t.: & V(\rho) \leq V_0 \\ & 0 < \rho_{min} \leq \rho_k \leq 1 \quad \forall k \in T_k \end{cases} \tag{5.4}$$

Here I indicates the set of all LCs, J_1 only fatigue LCs and T_k the elements in the whole DS.

Side constraint on densities is introduced with a $\rho_{min} = 0.001$ in order to avoid singularities on stiffness matrix at each iteration. Moreover, $TSFC_0$ is imposed equal to the value of $TSFC$ in LC 1056: this follows the logic of improving performances in all critical load configurations.

Note that Eq. 5.2 represents the classical problem in TO. The same problems will be solved also adopting a MMO procedure.

Then, OGV bending loads are included in successive TO problems, leading to the following analysis:

$$\begin{cases} \min & \max_{i \in I} C_i(\rho, U_f(\rho)) \\ s.t.: & V(\rho) \leq V_0 \\ & TSFC_j \leq TSFC_0 \quad \forall j \in J_1 \\ & M_{OGV,bend,j} \leq M_0 \quad \forall j \in J_2 \\ & 0 < \rho_{min} \leq \rho_k \leq 1 \quad \forall k \in T_k \end{cases} \tag{5.5}$$

$$\begin{cases} \min & \max_{i \in J_2} M_{OGV,bend,i}(\rho, U_f(\rho)) \\ s.t.: & V(\rho) \leq V_0 \\ & TSFC_j \leq TSFC_0 \quad \forall j \in J_1 \\ & 0 < \rho_{min} \leq \rho_k \leq 1 \quad \forall k \in T_k \end{cases} \tag{5.6}$$

$$\begin{cases} \min & \max_{i \in J_1} TSFC(U_f(\rho)) \\ s.t.: & V(\rho) \leq V_0 \\ & M_{OGV,bend,j} < M_0 \quad \forall j \in J_2 \\ & 0 < \rho_{min} \leq \rho_k \leq 1 \quad \forall k \in T_k \end{cases} \tag{5.7}$$

Here J_2 represents the set of limit LCs.

It is important to underline the fact that aggregation is applied both to objective and constraints in every TO problem. The built-in *MINMAX* key (in *Optistruct* environment) is adopted for the first scenario, while user-defined aggregation formulations will be adopted for all successive simulations.

Finally, a Pareto front based on the variations of objective in function of variation in constraint values (except for the side constraint on densities) will be traced.

Chapter 6

Preliminary Results: Stow Configuration

In this chapter, preliminary results regarding the Single-Model Optimization problem are presented. The engine is considered in Stow Configuration and only relative Load Cases are taken into account. Results of the distributions of densities are presented with linear interpolation and threshold filter set to 0.45.

In Section 6.1, minimization of compliance under volume fraction constraint is treated. In Section 6.2, TSFC constraint is added. In Section 6.3, a minimization of the effects of tip clearances on TSFC under volume fraction constraint is presented.

6.1 Classical Problem

The Classical Topology Optimization Problem consists of a simple minimization of compliance under volume fraction constraint (Eq. 5.2). Here, we consider the compliance of the complete Design Space (both solid and shell elements), without including the rest of the engine itself in the compliance computation. Moreover, the volume constraint is fixed following the principle to get an overall mass which is exactly equal to the base engine itself.

Given the presence of 16 Load Cases, this problem can be translated into the minimization of the maximum compliance over the totality of Load Cases.

In a first approach, we tried to adopt the built-in MINMAX option in *Optistruct*. The results are displayed in Fig. 6.1. Here we can observe a lack in convergence of the final solution. In fact, the built-in MINMAX option considers a number of sub-cases lower than 16. Moreover, the algorithm can choose any sub-case at each iteration. In this way, the already implemented aggregation approximates the *max* functional making it smoother, but the continuity is not always guaranteed.

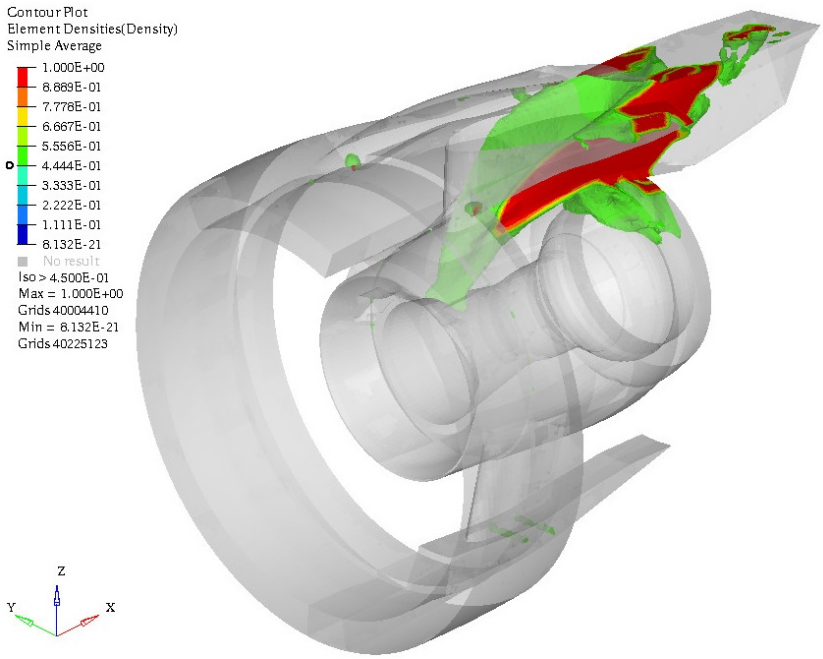

Figure 6.1: Classical Problem (MINMAX): iso-view of optimized structure

Secondly, a *p-norm* objective aggregation (with aggregation hyper-parameter $p = 4$)was implemented. This is translated into the introduction of a supplementary optimization response *DRESP2* including all the Load Cases. Results in terms of density distribution are reported in Fig. 6.2. This time, continuity is ensured by the aggregation itself and the obtained structure is

regular.

The structure presents a simple box which links the rear upper spar to the core of the engine. Two attacks on the core are provided in correspondence to the front engine mounts, at the level of the last stage of the compressor (HPC10) and to the rear engine mounts, at the level of the first stages of the turbine. This latter is quite massive and solution could still be improved through a mesh refinement. On the rear upper spar we may find three different chains, re-uniting on a single point in correspondence to the aerodynamic surfaces. What may surprise is the relatively small thickness on the rear chain, which is supposed to support the moments around y-axis: actually, the reason is explained through the convergence history.

The fan-case is linked to the Design Space through two little reinforcements starting from the fixed beams of the TRU. Efforts on cradle aerodynamic surfaces can pass directly to the Design Space through the rear sector. The primary load path is then closed through two reinforcements on the lower fixed beams of the TRU.

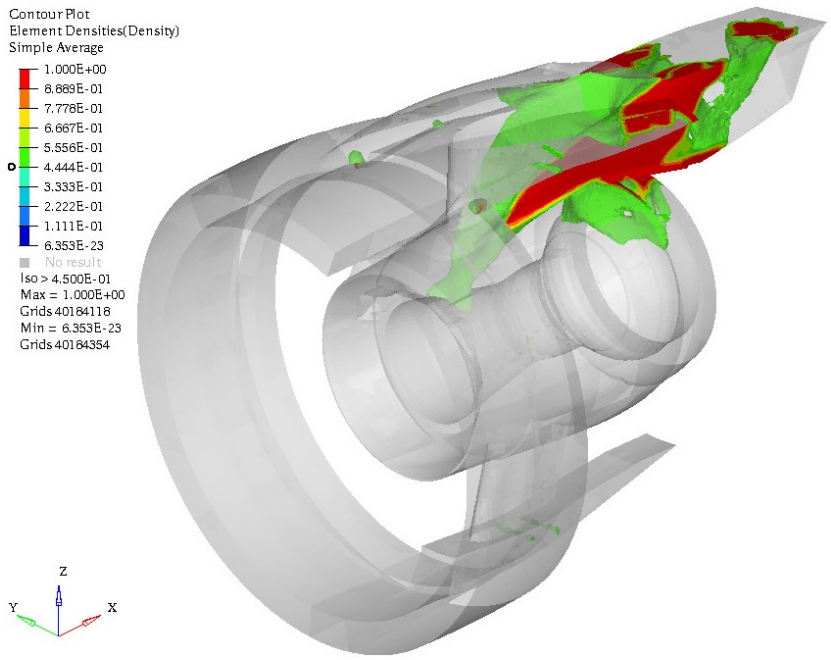

Figure 6.2: Classical Problem (with compliance aggregation): iso-view of optimized structure

In Fig. 6.3, the convergence diagrams are reported. From a superficial comparison between the evolutions of compliances in single sub-cases and the global objective, one can notice that the Load Cases driving the optimization are the static Load Cases 2018 and 2019. In fact, the objective reproduces exactly the variations of these two responses of the model. This is also the reason why the rear chain (which links the rear upper spar to the main body of the optimized solution) appears not to be relatively stiff. Actually, the optimized structure aims to maximize the stiffness to moments around z-axis and forces along y-axis, without taking into account the bending moments around y-axis.

Following objective convergence history, an initial growth is observed at the beginning, followed by an almost totally regular reduction. This evolution is typical of a TO problem. The first increase in terms of aggregated compliance is triggered by the attempt to reach the first feasible solution.

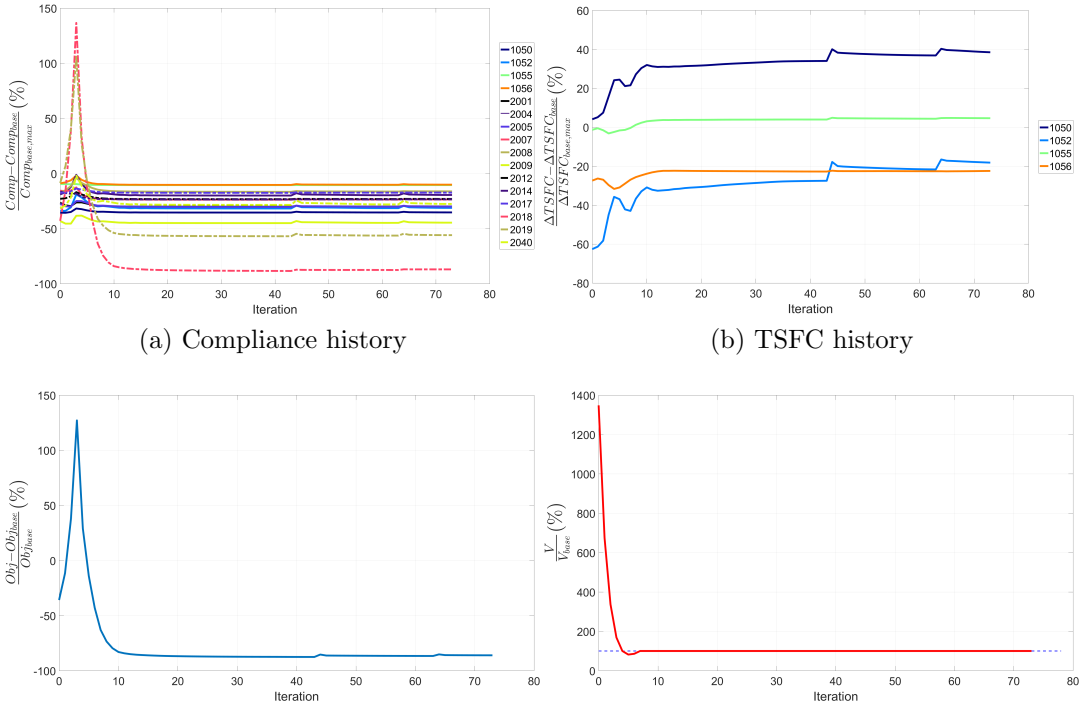

(a) Compliance history

(b) TSFC history

(c) Objective history

(d) Volume fraction history

Figure 6.3: Classical Problem (with compliance aggregation): convergence history

Then, the first decrease is very fast and followed by an almost stationary evolution of the objective itself: this doesn't imply that the density distribution doesn't change. In order to avoid local minima, as stated in Chapter 3, a continuation method is adopted by *Optistruct*: a plausible trace may be furnished by the little irregularities reported in objective convergence diagram.

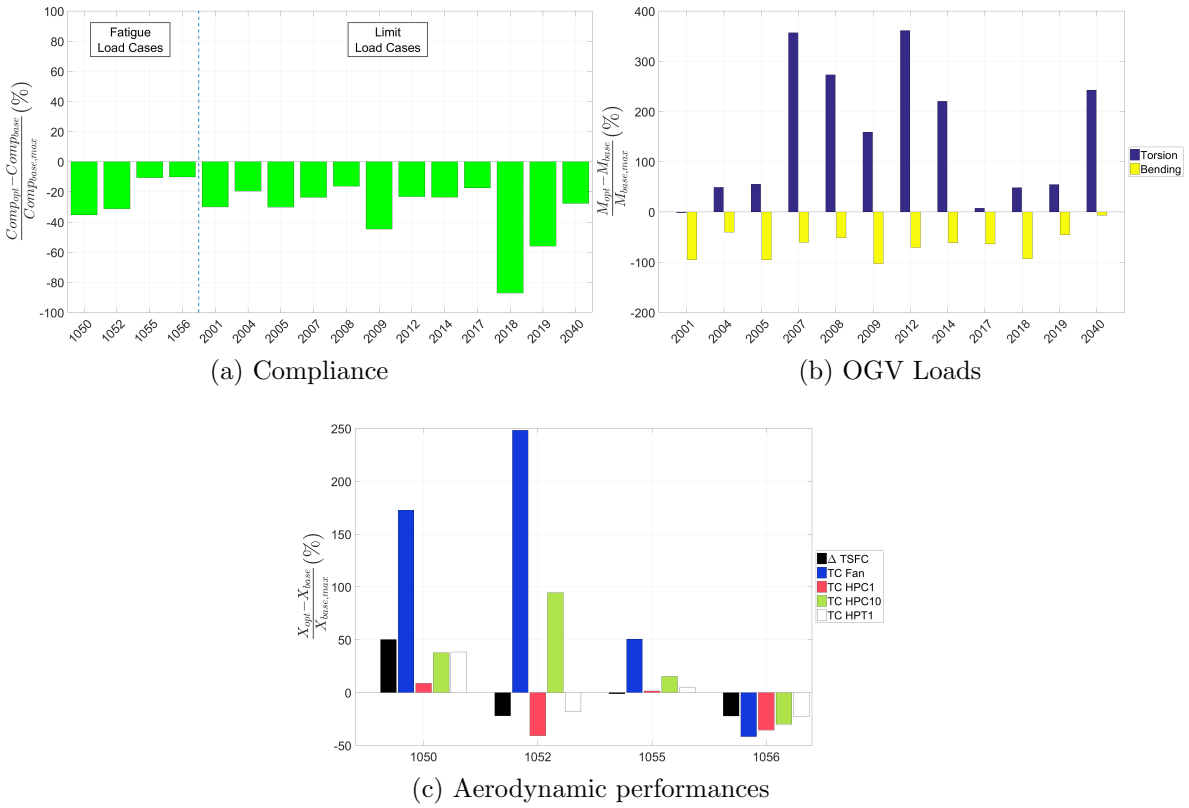

(a) Compliance

(b) OGV Loads

(c) Aerodynamic performances

Figure 6.4: Classical Problem (with compliance aggregation): global gains

Globally, compliance is reduced in every load case, above all in 2018 and 2019, which determine the sizing of the whole structure.

Bending loads are reduced but torsion is increased: however, given the different orders of magnitude, this effect can be neglected.

Looking at the aerodynamic performances, the contribution on TSFC given by tip clearances is reduced in LC 1052, the most critical and 1056. This reduction is ensured by the first stage of the compressor (HPC1) and the first one of the turbine (HPT1). This result shows also an increase in tip clearance at the fan stage: even if mathematically this reduces the global variation in terms of TSFC, a successive CFD analysis should be performed to verify the validity of the analytical model in Eq. (5.1).

6.2 Compliance Minimization (under TSFC and Volume Fraction constraints)

In this section, the aggregated constraint on TSFC is included in the analysis (Eq. 5.3), adopting G^l_{KS} aggregation function. Two results are reported in Fig. (6.5)-(6.6): in the first one, a limit equal to the value of the worst fatigue load case (on baseline architecture) is imposed, following the logic that performances must not be decreased; in the second analysis, a limit equal to the minimum value over all load cases is considered.

Actually, the first one presents an inactive constraint on TSFC, furnishing the same results obtained in the previous section. On the other side, by imposing a limit equal to the minimum value over specific consumptions in all Lcs in baseline engine, the constraint becomes active: in particular, the links between DS and compressor stages and the rear chain connecting to the wing are weakened, while the support on the turbine stage is reinforced.

To better understand the reasons behind these results, convergence history and global gains are presented in the following.

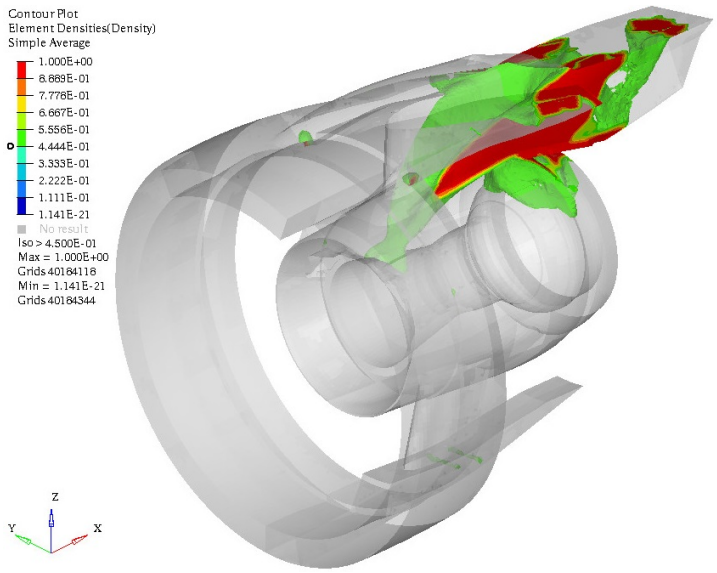

Figure 6.5: Compliance minimization under TSFC aggregated constraint (inactive at optimality): iso-view of optimized structure

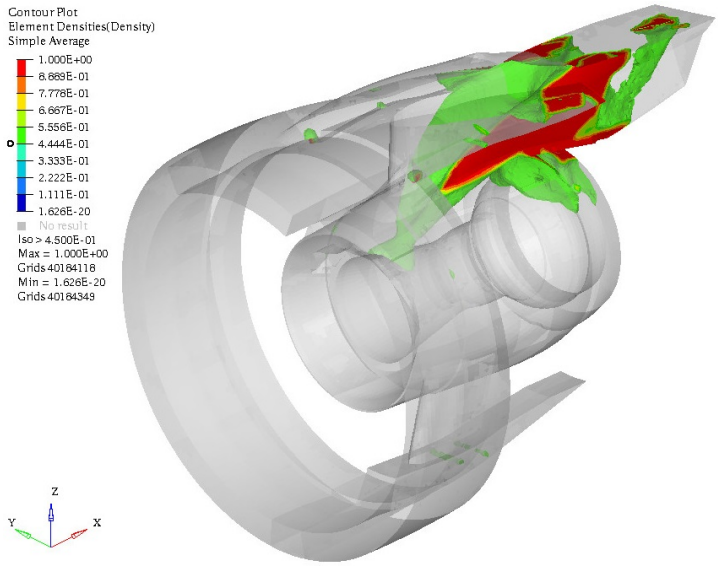

Figure 6.6: Compliance minimization under TSFC aggregated constraint (active at optimality): iso-view of optimized structure

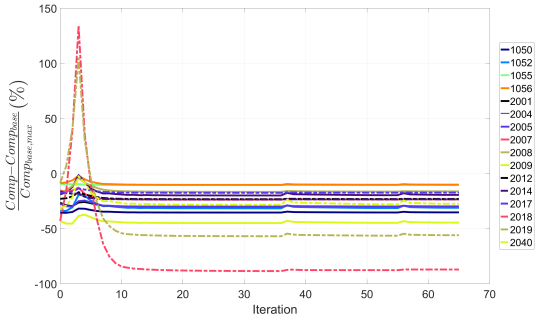

(a) Compliance history

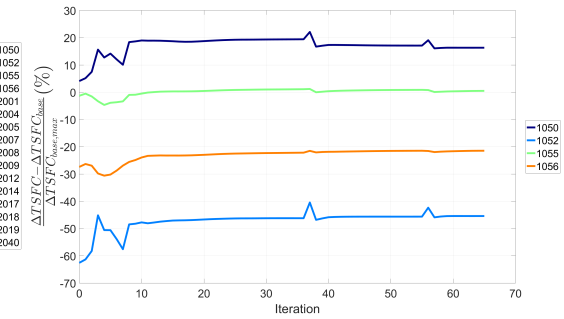

(b) TSFC history

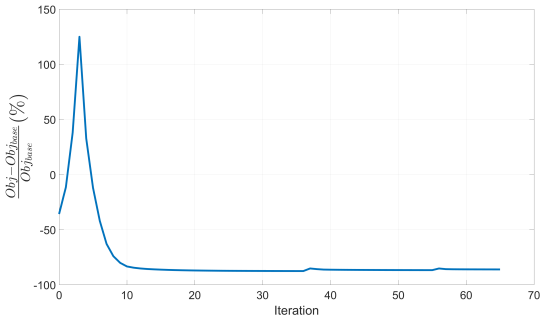

(c) Objective history

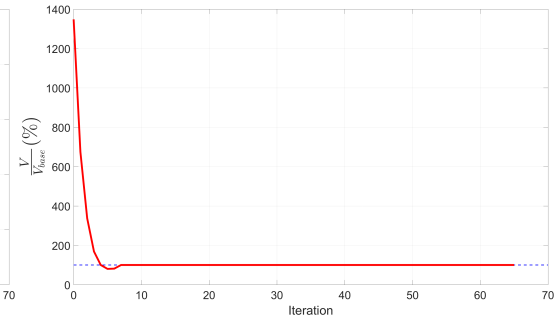

(d) Volume fraction history

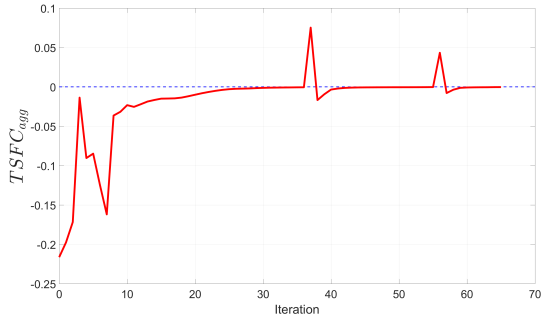

(e) TSFC aggregation history

Figure 6.7: Compliance minimization under TSFC aggregated constraint: convergence history

The convergence history of this analysis is similar to the one in the previous section. Almost the same path is followed by the objective function and volume fraction. Subcases 2018 and 2019 still drive the optimization process, in terms of compliance. The only difference in these two evolutions is given by the fact that here continuation does not affect the objective, but the respect of the introduced TSFC aggregated constraint, as visible in Fig. (6.7.e). The introduction of this new constraint clearly influences also the evolution of TSFCs in all fatigue load cases: the initial idea of improving all performances with respect to the baseline proved successful. Only LC 1050 sees an increase in consumption, while others are improved. In particular, LC 1056 is hugely improved (TSFC is reduced by 45%). From the graphs we can notice that LCs 2018 and 2019 drives the evolution of the newly introduced constraint.

As seen in previous section, compliances are reduced in every load case: the most evident improvement are relative to 2018 and 2019 subcases.

Looking at the OGV loads, we notice a less relevant decrease in bending and a more drastic increase in torsion moment with respect to the previous analysis: this suggests that consumption and loads are antagonists in the optimization process, while bending and torsion go on the same side. Thus, a constraint on bending load (the most relevant) could be introduced.

Finally, aerodynamic performances follow the same notions introduced in previous paragraph. With respect to the precedent results, the massive reinforcement on the turbine is justified by the fact that tip clearance on HPT1 stage shows the greatest influence over TSFC.

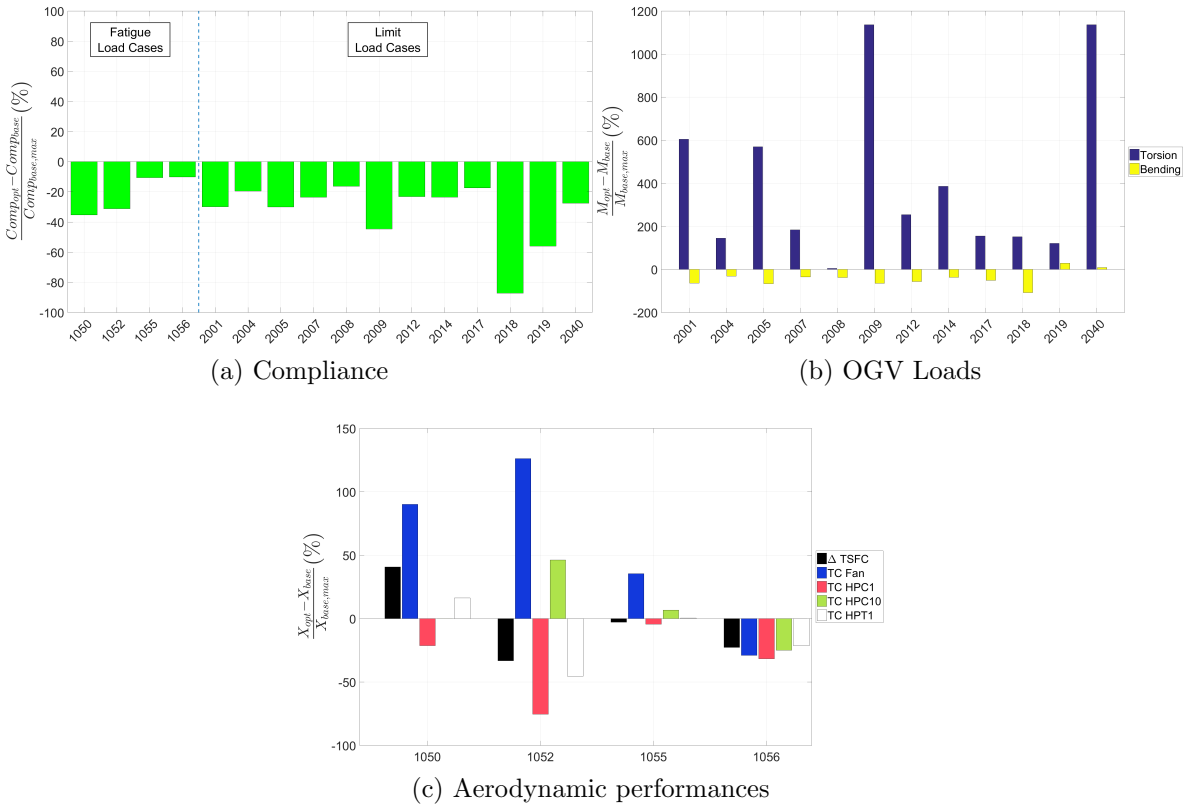

(a) Compliance

(b) OGV Loads

(c) Aerodynamic performances

Figure 6.8: Compliance minimization under TSFC aggregated constraint: global gains

6.3 TSFC Minimization

In this section, a minimization of the effects of tip clearances over global TSFC is performed. The only constraint introduced is relative to the volume fraction (Eq. 5.4).

In this case, a great sensibility on the limit move step (DELTOP in *Optistruct*) is encountered. In both solutions represented in Fig. 6.9, the optimal structure is not continue and floating structures are present. Moreover, connections are not defined, making the structure extremely flexible. In fact,

this formulation is not sufficient in Stow configuration to ensure a stiff structure.

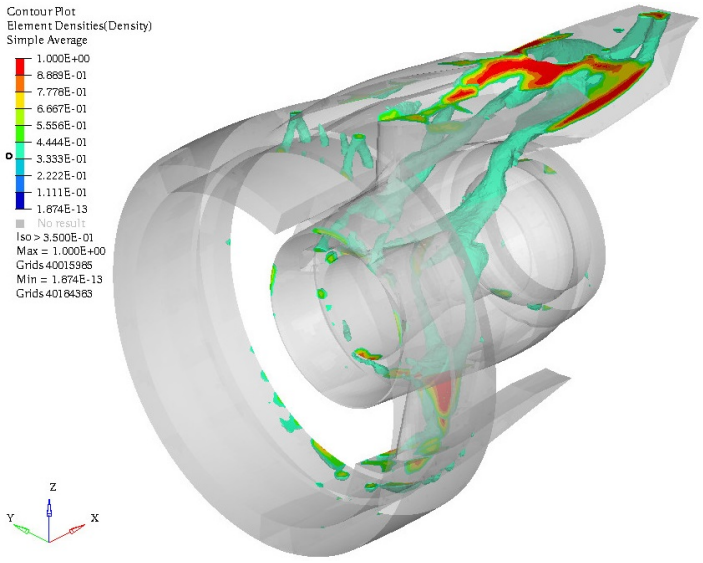

(a) DELTOP=0.5, default

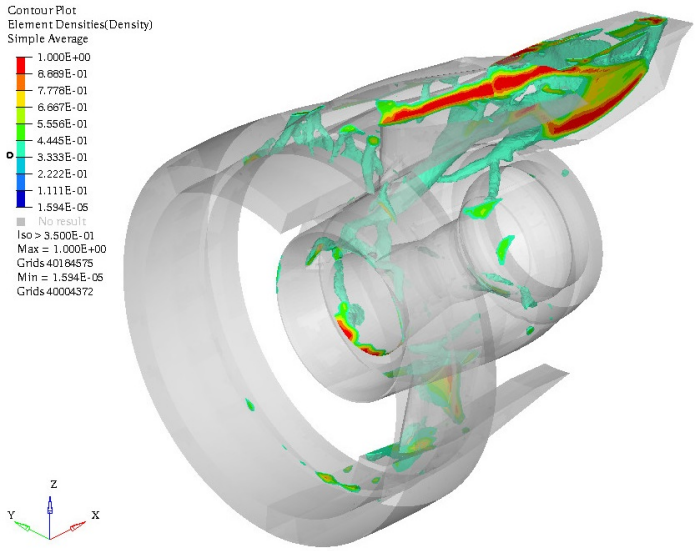

(b) DELTOP=0.1

Figure 6.9: TSFC minimization: iso-view of optimal structure (DELTOP=0.1)

Chapter 7

Numerical Results

In previous chapter three analysis were performed in Stow configuration. Among these, the minimization of TSFC under volume fraction constraint does not ensure a continuous rigid structure.

The most complete analysis, at this point, is compliance minimization under volume fraction and TSFC constraints: it's visible that compliance and volume fraction are antagonists, as well as compliance and TSFC. Moreover, in optimality conditions, TSFC and loads drive solution on different directions.

Overall, the sizing LCs are (in Stow configuration) 2018 and 2019 for compliance, and 1052 and 1056 for TSFC. The optimal solutions thus reflect the need for a stiff structure, capable of resisting to transversal loads, penalizing the structural performances in bending around $y-$axis.

In this Chapter, Reverse Configuration is added and two LCs are thus introduced, respectively one fatigue and one limit LC. In Section 7.1, three analysis analogue to the ones presented in Chapter 6 are reproduced and detailed. In Section 7.2, OGV load constraint is introduced in TO problems. Finally, in Section 7.3, a Pareto Front is traced following the influences among optimal compliance, volume fraction, OGV loads and TSFC.

7.1 First MMO Results

In this Section, the same TO problems treated in Chapter 6 are repeated with the introduction of Reverse configuration and the two associated LCs.

7.1.1 Classical Problem

First of all, compliance minimization under volume fraction constraint is performed (Eq. 5.2). In Fig. 7.1 we can observe an optimal structure which is substantially different from the one obtained in Stow Configuration (see Fig. 6.2). Here aerodynamic surfaces assume a fundamental role in bending stiffness: a closed force path involving the whole engine is then introduced.

With respect to the previous structure (presented in Chapter 6), the rear chain which linked the engine to the wing is now substituted by several panels covering the aerodynamic surfaces. This is a useful hint to change the perception of aerodynamic surfaces, now assuming a structural function. Several reinforcements on the upper boundary of the DS are also introduced.

The massive structure linking the turbine to the Design Space is very similar to the one seen previously. Also the connections between the inferior fixed beams of the TRU and between upper fixed beams and fan case appear unchanged.

The engine mount on the compressor stage presents a similar size, but different shape (here it is more regular) and a different orientation (this design is more vertical than the previous one). This is another consequence of the introduction of two new LCs, where forces have got a different orientation and thrust may not be the prevalent one.

New connections appear between the front mount ring and the panels on the IFS (they are visible in Fig. 7.1.b as micro-structures in circular disposition) which is involved only locally.

Several defects (in terms of useless micro-structures) are still present between fan case and fan cowl at the final iteration.

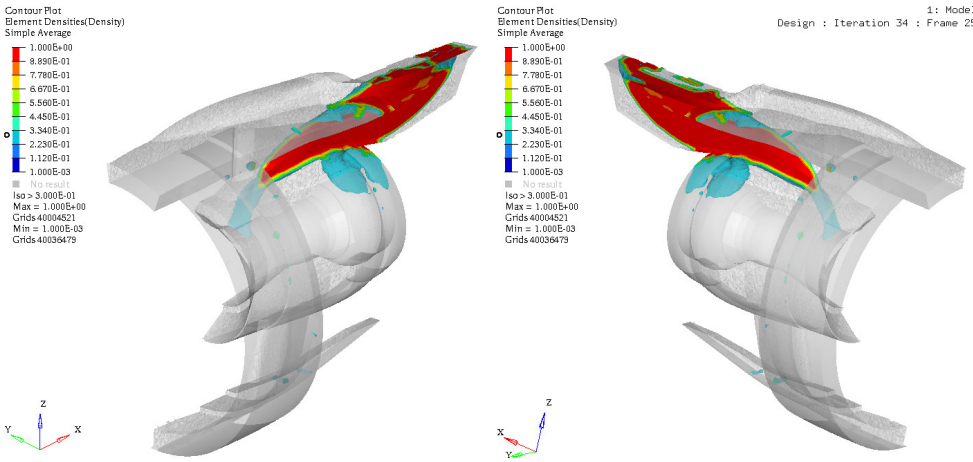

(a) Exploded view

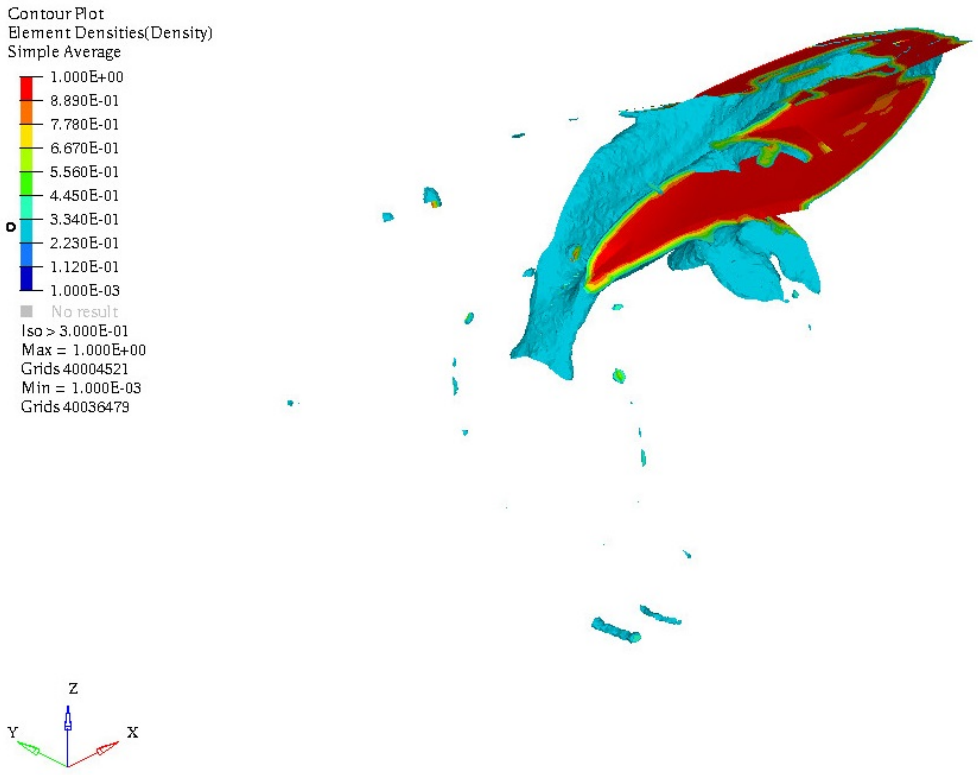

(b) Iso-metric isolated view

Figure 7.1: Classical Problem (MMO): iso-view of optimised structure

Looking at the convergence history (see Fig. 7.2), it is easy to understand that in this case, convergence is accelerated with respect to the Stow Configuration. The convergence rate allows the algorithm to apply a continuation much sooner than what was done for the analogue TO problem in Chapter 6.

Focusing on the compliance evolution in all subcases, one can easily find out the influence of the Reverse LCs on the whole problem, above all the subcase 2192. The global objective (given by the aggregation via $p-norm$ of the individual compliances) follows the same history than the LCs 2018 and 2019 in Stow Configuration as well as the newly introduced LCs in Reverse Configuration, 1193 and 2192. It is interesting to underline the fact that a fatigue LC (actually present all along engine life) can be determinant to the design of the primary structure itself.

Through a fast analysis on the volume fraction history, one can see how the different model impacted the convergence rate. In fact, at the end of the first overshoot of the objective (aiming at getting to the respect of the constraint), the volume fraction value is slightly superior to the allowed limit, preventing the graph from presenting oscillations (which can slower convergence rate).

Now, taking a look at the compliance gains at the final iteration, we notice the similar tendency to mostly reduce the most active LCs (2018 and 2019 in Stow, 1193 and 2192 in Reverse) of almost one order. This is essentially the same concept which was applied in the analogue TO problem in Stow Configuration.

By making a balance of OGV loads, we observe the same increases in torsion load reported for the compliance minimization under TSFC aggregated constraint in Chapter 6. Thus, with respect to the analogue TO problem in Stow configuration, the balance on structural performances is worsened. Moreover, we may observe the first increase in bending loads on OGV in the Reverse LC 2192. This implies that a constraint on OGV loads should be implemented and analyzed.

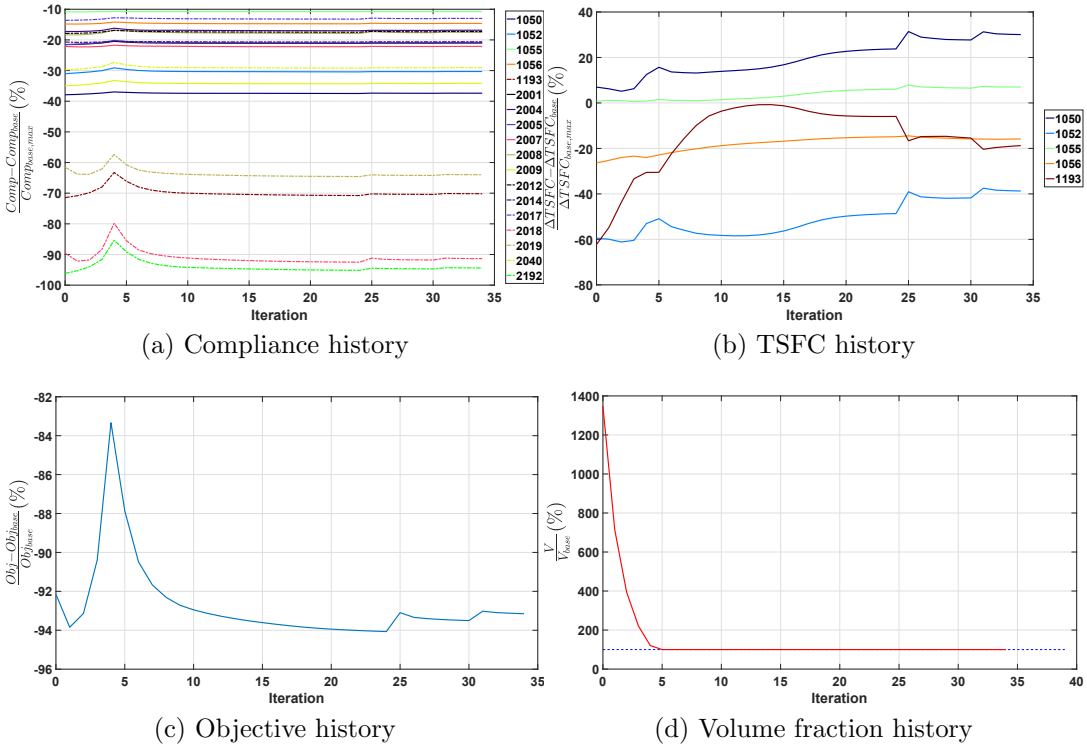

(a) Compliance history

(b) TSFC history

(c) Objective history

(d) Volume fraction history

Figure 7.2: Classical Problem (MMO): convergence history

With respect to the aerodynamic performances, in this formulation the evolution of the impacts of tip clearances over the variation in specific fuel consumption is similar to the one observed in previous Chapter. However, here fan stage is no more the most penalized: in fact the first stage of the high-pressure compressor presents an increased tip clearance. Again, such huge variations should be better analyzed through CFD simulations, in order to conclude on the validity of the analytical model of $\Delta TSFC$.

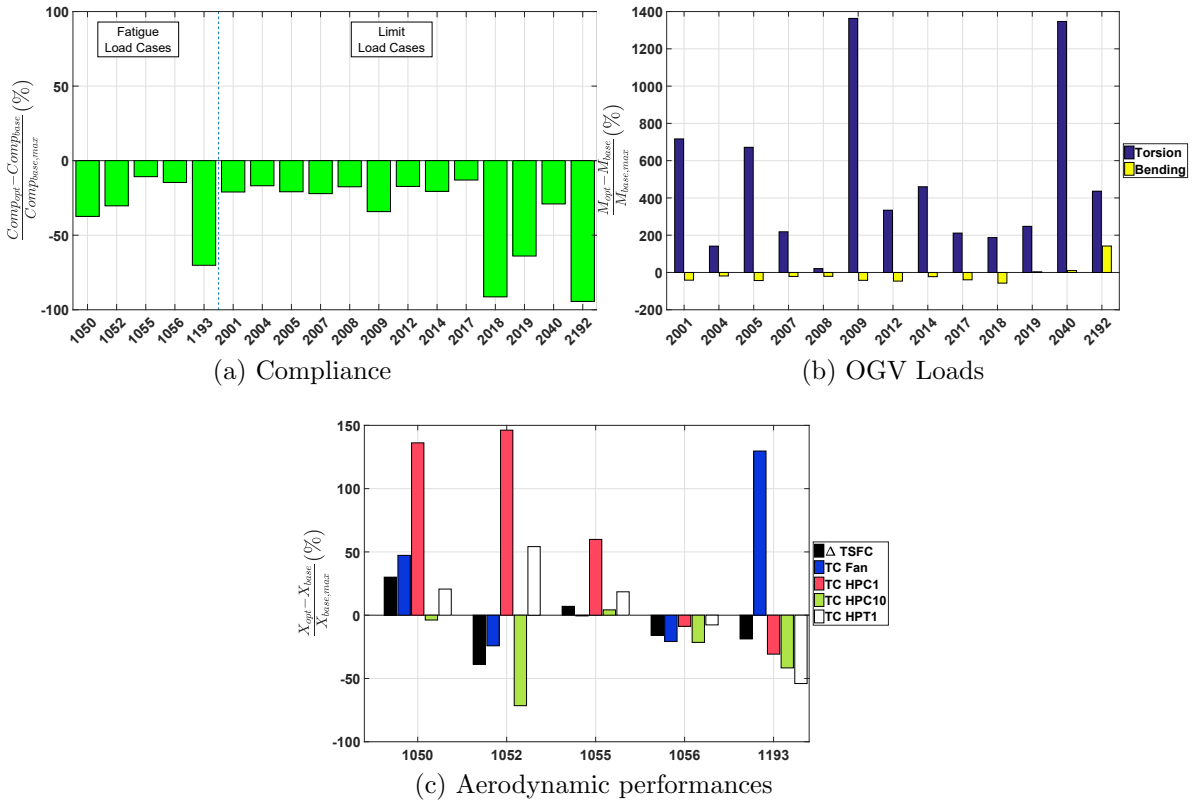

(a) Compliance

(b) OGV Loads

(c) Aerodynamic performances

Figure 7.3: Classical Problem (MMO): global gains

7.1.2 Compliance Minimization (under TSFC constraint)

In Fig. 7.4, the results relative to the second TO problem, regarding the minimization of compliance under TSFC and volume fraction constraints (Eq. 5.3), are reported.

The optimal structure is slightly modified with respect to the ones in Chapter 6 and in previous section. Comparing this result with the one in Fig. 6.2, we observe the effects of the introduction of Reverse Configuration and the related LCs: as seen previously, this is visible through the conversion of the rear chains into a box involving the aerodynamic surfaces. The attack on the compressor stages is reinforced and the section is very thick and uniform. This appears to be also different from the attack visible in Fig. 7.1.

The rear structure supporting the turbine stages is thicker than any other previous simulation and it involves the IFS on few points.

Upper fixed beams are always linked to DS in the rear part. As usual, inferior fixed beams of the TRU are connected through two little beams placed in the median section. Moreover, we may notice the constant link between fixed beam and fan case. A substantial difference is provided by the appearance of a similar structure on the inferior part of TRU, maybe linking inferior fixed beams to the fan case. However, this connection is not complete at convergence: repeating simulation with a superior number of iterations or a tighter tolerance on the variation of the objective function would provide us with poor improvements; on the other side, exploring the solution through the use of a finer mesh or the adoption of an higher volume fraction constraint could constitute better approaches.

Connections between DS and IFS are provided in the support to the turbine. Moreover, the reinforcements announced and described in Fig. 7.1 are here stiffer and more defined. This could be a hint to the fact that IFS could be involved in TSFC regulation.

Overall, we cannot ignore the presence of micro-structures which are in contact with the non-design region. They probably come from the combination of numerical errors and low threshold filter value (here fixed at 0.3).

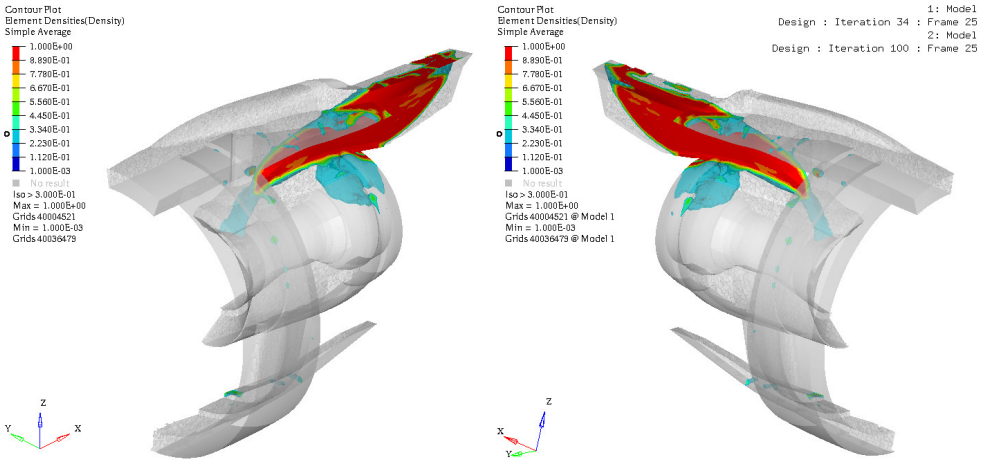

(a) Exploded view

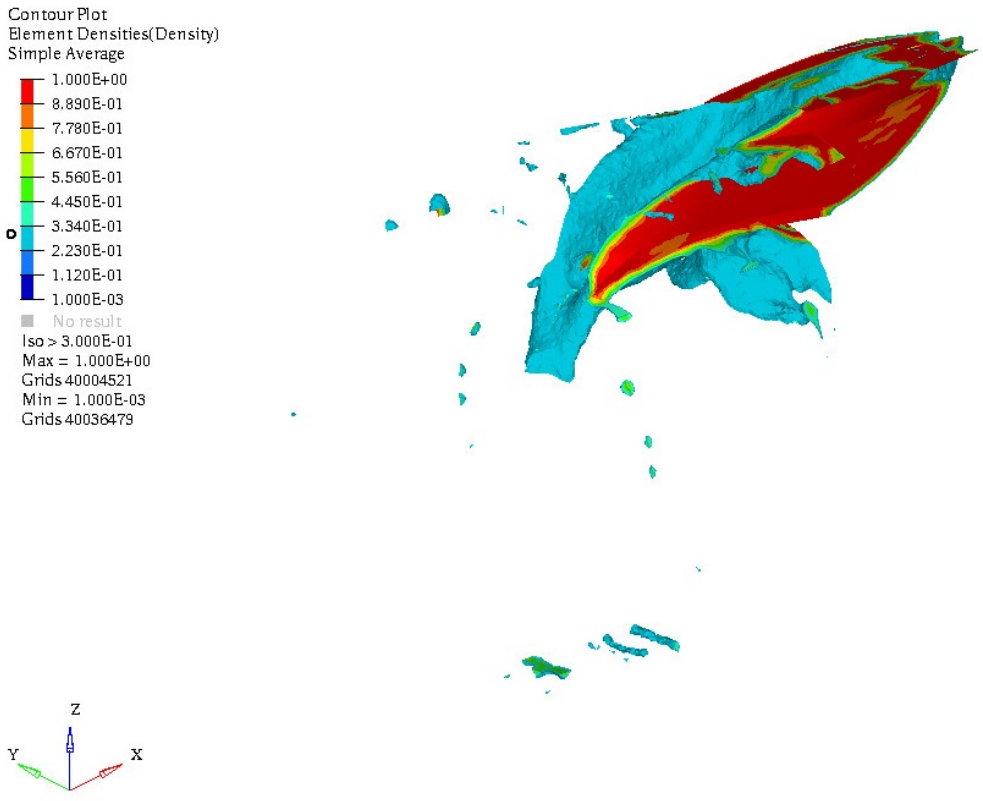

(b) Iso-metric isolated view

Figure 7.4: Compliance minimization under TSFC aggregated constraint (MMO): iso-view of optimised structure

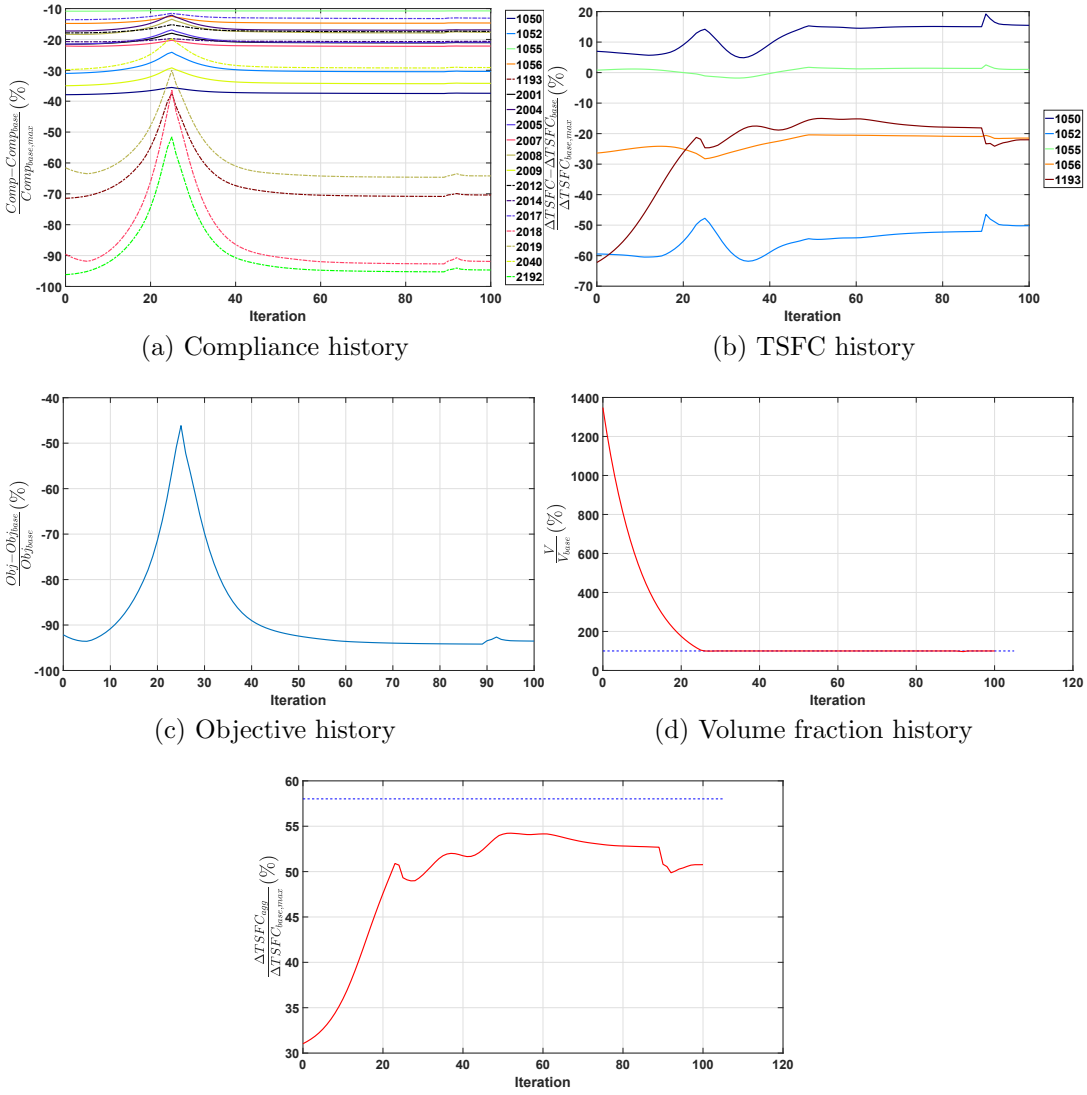

(a) Compliance history

(b) TSFC history

(c) Objective history

(d) Volume fraction history

(e) TSFC aggregation history

Figure 7.5: Compliance minimization under TSFC aggregated constraint (MMO): convergence history

The analysis of the convergence history of this simulation (see Fig. 7.5) is similar to the one described in Fig. 6.7. Optimization is initialized and presenting a violated volume fraction constraint, while satisfying the TSFC

aggregated constraint. The path followed by the objective function is typical of such an analysis with initially violated constraints. Although TSFC aggregation constraint is not active at the beginning, it increases all along the analysis, but never getting to saturation. For this reason, no LC can be identified determinant for the optimal design of the structure.

One continuation is applied after iteration 90: this hugely influences TSFC and compliance outputs of the structure, keeping volume fraction unchanged.

With respect to results presented in Fig. 6.7, TSFC here does not constitute an active constraint, even if the imposed limit is the same. Thus, the shape of the objective function is drastically changed after the introduction of Reverse Configuration and related LCs. However, given that the shape of the optimal structures in Fig. 7.1 and 7.4 are different, one can conclude that somehow the algorithm takes into account the respect of the TSFC aggregation constraint (it also appears in output files among retained responses) while performing each sensitivity analysis. This is justified by the fact that this output cannot be neglected face to unity.

At the end of the simulation, convergence is not exactly attended, but the variation on the objective function can be considered sufficiently low to retain this solution after 100 iterations.

Now focusing on global gains at the end of the simulation (reported in Fig. 7.6), one can easily notice that the balance is almost exactly the same than the one examined in previous section (confront Fig. 7.3).

Again, for compliance, the sizing LCs are 2018 and 2019 in Stow Configuration, combined with 1193 and 2192 in Reverse. These correspond also to the LCs where compliance is mostly reduced.

The increase in torsion is more evident than the analogue multi-model TO problem without any constraint on TSFC. The same variation is visible in bending load on the Reverse LC 2192: in particular, in this solution, its value is doubled.

On the other side, specific consumptions appear improved in all LCs

and the variations on tip clearances are globally taken under control. An interesting result is given by the compressor stages HPC1 and HPC10 in LC 1052: this unbalance could still derivate from an error on the analytical model of TSFC, leading to the need for a deeper investigation through CFD analysis.

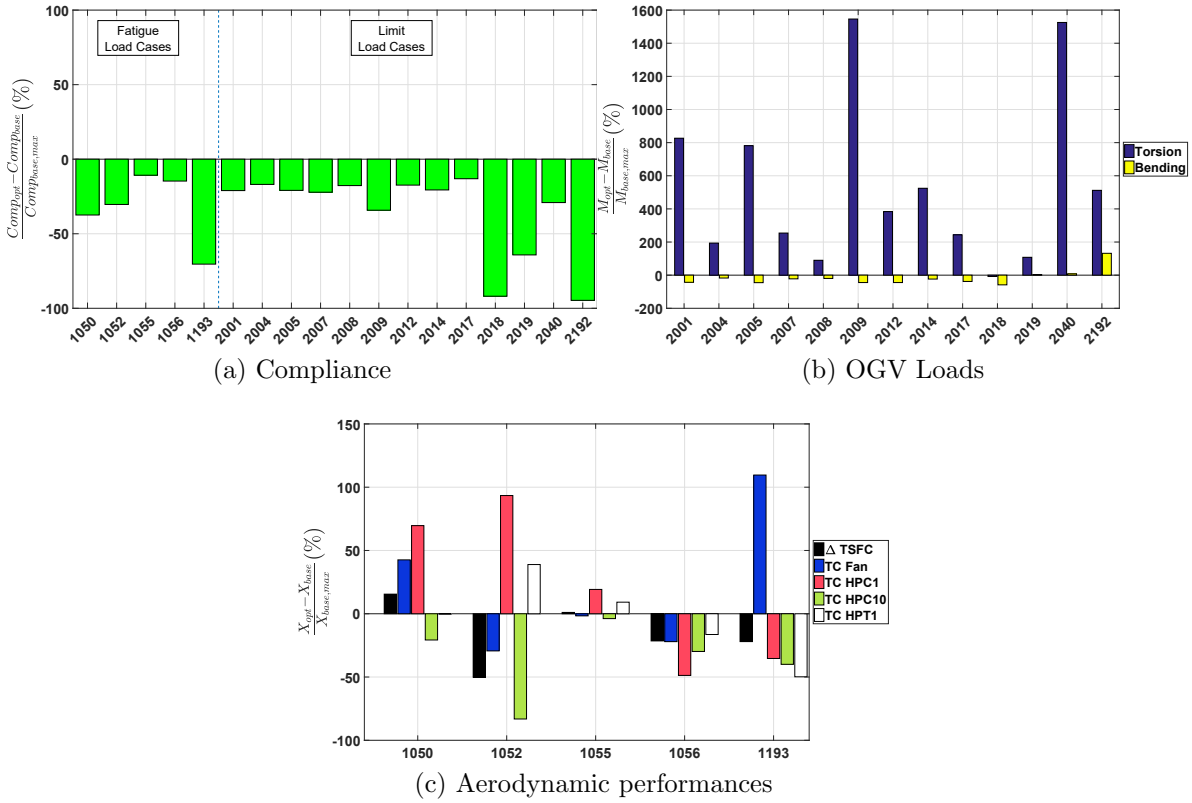

(a) Compliance

(b) OGV Loads

(c) Aerodynamic performances

Figure 7.6: Compliance minimization under TSFC aggregated constraint (MMO): global gains

7.1.3 TSFC Minimization

In this section, a TSFC minimization under volume fraction constraint is performed in MMO version (Eq. 5.4). Only fatigue load cases are taken into account in the optimization process, while limit LCs are just monitored. The final structure is reported in Fig. 7.7.

Optimal structure is totally different from any other solutions seen previously. It is essentially based on an aggregation of beam structures.

The back of the structure is not very different from the solutions relative to the minimizations of compliance in Stow Configuration: in fact, a system of beams supports the residual of the upper spar and ensures the respect of Boundary Conditions. The shape is totally different from the previous case, but the logic followed by the solution is the same. However, this system of chains is doubled on the two sides of the DS.

This double structure is then linked to the main engine mount on the top and a complementary support on the bottom.

The former is constituted by a Y-shape beam joining back-support to the front engine mount. The orientation is quite horizontal and aims at supporting thrust efforts.

From rear structure, a support involving both sides of IFS is present: as announced before, IFS is somehow involved in TSFC regulation. These two beams are connected through a small beam.

The totally new introduction of this formulation is given by a skeleton surrounding the engine and connecting the upper-mentioned beam (the link between the two supports of IFS) and the lower bi-fi, now acquiring a role in primary structure. The skeleton is also glued to the turbine, thus ensuring a support quite different from the ones seen until this moment. In particular, turbine is no more supported from above but from the inferior half.

At the bottom, the lower bi-fi is filled by shell elements and substitutes the previous connection between inferior fixed beams of TRU. It should also be connected to the front engine mount, but convergence is probably not sufficient to establish this junction.

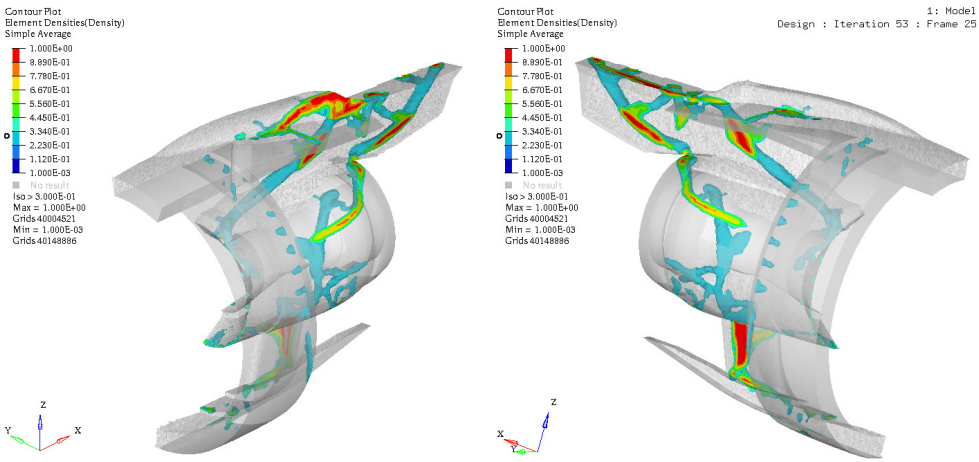

(a) Exploded view

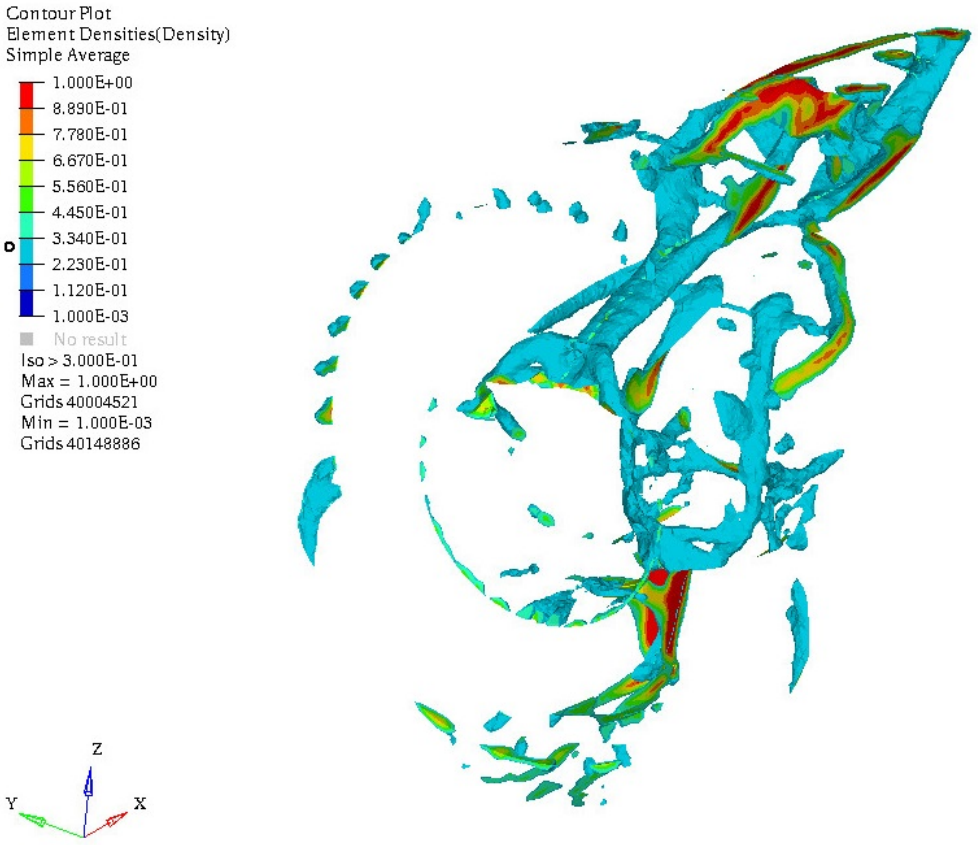

(b) Iso-metric isolated view

Figure 7.7: TSFC minimization (MMO): iso-view of optimised structure

To complete the load path, the series of reinforcements all around front mount engine ring is enhanced to ensure a better control over TSFC.

Such a structure based on thin beams presents the advantage of generating distributed inertial loads, on the opposite side of the massive structures analyzed at this point

It is important to underline the fact that several micro-structures are present in the final result, but maybe derive from numerical error in the optimization process.

This formulation cannot stand alone to define a stiff structure, as seen in the analogue TO problem in isolated Stow Configuration. However, with respect to the previous analysis, the errors can be easily adjusted by hand by an engineer, since connections are clearly identified.

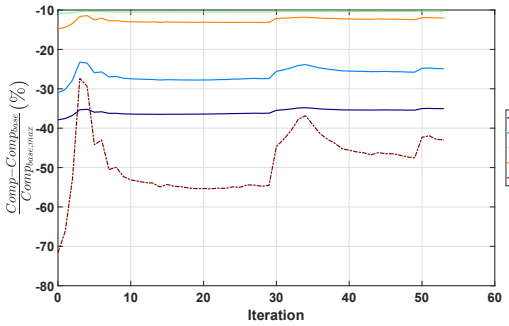

(a) Compliance history

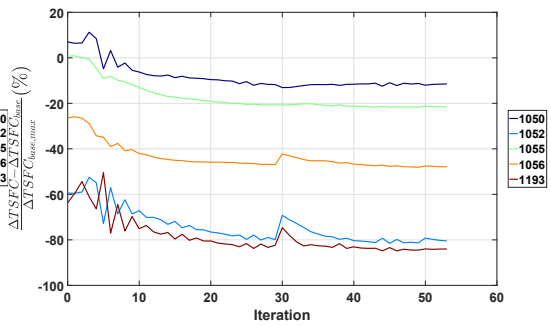

(b) TSFC history

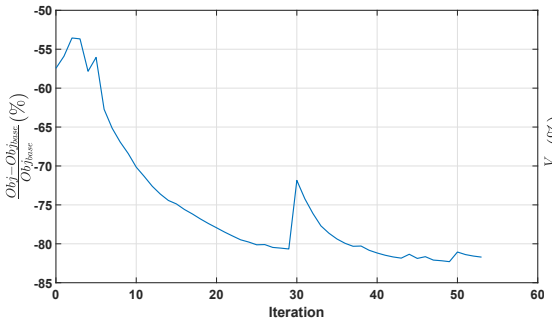

(c) Objective history

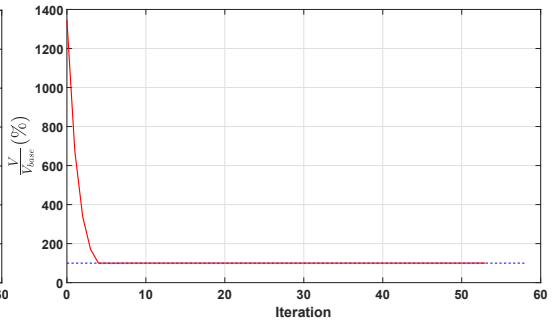

(d) Volume fraction history

Figure 7.8: TSFC minimization (MMO): convergence history

In Fig. 7.8 the complete convergence history is furnished. Here, compliances are only monitored.

The objective (aggregated TSFC) shows a totally different evolution from previous ones: in fact, despite volume fraction is initially violated, objective is not too much penalized. This can be explained from the nature of TSFC: this is defined from local relative displacements (tip clearances), which do not take into account the global movements of the whole structure. The algorithm thus focuses on locally reinforcing the structure, without necessarily increasing the global stiffness. Looking at compliances evolution, for example, we may observe the increase all along the simulation (i.e. a reduction in stiffness): this is evident above all in Reverse LC 1193, which was a critical LC in all compliance minimization in all MMO problems treated at this point.

Finally, results of this analysis show a drastic improvement of aerodynamic performances in all fatigue LCs. All tip clearances are reduced by far, with respect to all other simulations performed at this point. However, these results must be verified through CFD analysis, given the intensity of changes.

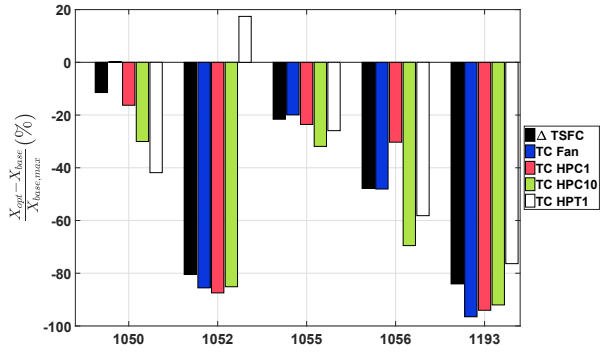

(a) Aerodynamic performances

Figure 7.9: TSFC minimization (MMO): global gains

7.2 Final MMO Results: OGV Loads constraint introduction

In this Section, OGV load are implemented into the model and taken into account in the optimization process. Compliance and TSFC minimization are repeated while including OGV bending load constraints. As well, these are also considered as objective in a third TO problem. In all scenarios, if not differently specified, all responses are aggregated via $p - norm$.

7.2.1 Compliance Minimization (complete formulation)

At this point, compliance minimization under volume fraction, TSFC and OGV load constraints is performed (Eq. 5.5). It is important to remind that TSFC is intended only on fatigue LCs, while OGV loads on static LCs. Constraint and objective aggregations are computed through $p - norm$ formulation. Moreover, bending moments are actually included in TO formulation, while torsion is only monitored. This constitutes the most complete formulation on the present study.

The solution found (reported in Fig. 7.10) consists of a very complex architecture. The basic idea of a box involving aerodynamic surfaces is still valid. However, mass devoted to this part of the optimal structure is inferior, as totally new components appear to satisfy both TSFC and OGV bending load constraints. On the other side, support structures connecting front mount ring to IFS disappear.

The support of turbine stages is limited now to an assembly of thin beams. In particular, the attack is based on six detached points: three on the first stages of turbine and three on the last ones. A complementary connection appears between the front attacks and the main box, to locally enhance the stiffness of the structure and taking the tip clearance on turbine stages under control.

The main box transmits the efforts on IFS through two hinges situated on the back, just in front of the attacks described in previous paragraph.

All connections between fan case and upper fixed beams of the TRU are maintained. Moreover, a new structure between main box and fan case appears on the left side of the engine. Given that DS is not exactly symmetric, on the right side (the slave in Pattern Repetition constraint used to implement the symmetry constraint in MMO), the flux of efforts passes through the aerodynamic surface on the cradle. The apparently floating structures in Fig. 7.10.b represent, in fact, this supplementary load path. This double architecture is seemingly devoted to retain efforts deriving from thrust loads. It is interesting to underline the fact that, again, aerodynamic surfaces contribute to the transmission of efforts in the primary structure.

The front attack linking DS and front mount ring is now divided into two parts: a quasi-horizontal central beam, clamped on the front ring itself (around low-pressure compressor stages); an oblique complex structure on the high-pressure compressor stages. The former is devoted to retain thrust loads (it creates, in fact, a continuous horizontal load path which passes through the main box), while the latter is supposed to absorb inertial efforts.

A totally new introduction, related to the combination of OGV bending load and TSFC constraint, is given by the complex architecture present at the bottom of the engine. This can be conceived as an X-shape structure, if observed from the left plan XZ. The bottom sector of turbine support is linked, together with the rear extremity of IFS, to the trailing edge of lower bi-fi. From here, the load path follows the aerodynamic surface till the inferior fixed beams of TRU and, then, to the bottom of the fan case (this connection involves just a few elements). An identical scheme is followed by the other half of the X-structure, linking high-pressure compressor stages to fixed beams of TRU and passing through the aerodynamic surfaces of bi-fi (where it crosses the upper-mentioned structure). Each part of this architecture is then transposed on the other side of the symmetry plan.

From this component, two connections to IFS are supposed to be part of the optimal structure, but they are not complete: actually, the constraint on volume fraction is too tight to allow the formation of a complete tie.

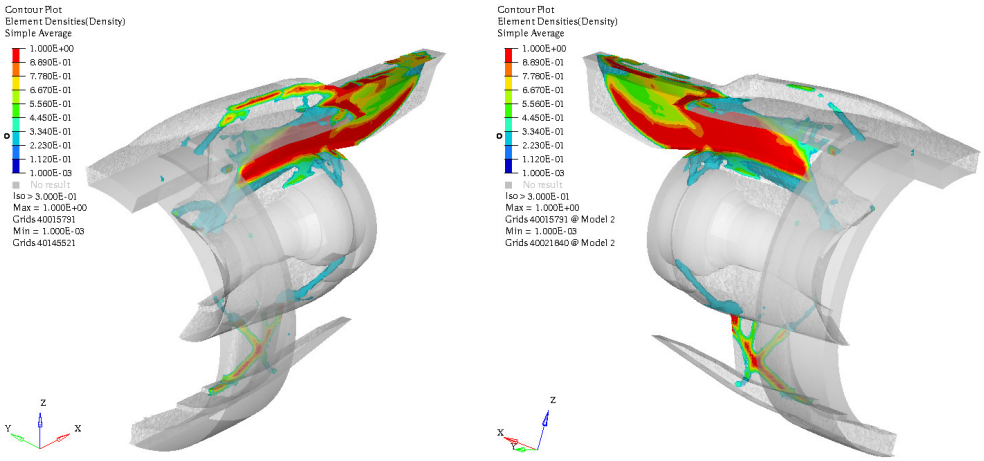

(a) Exploded view

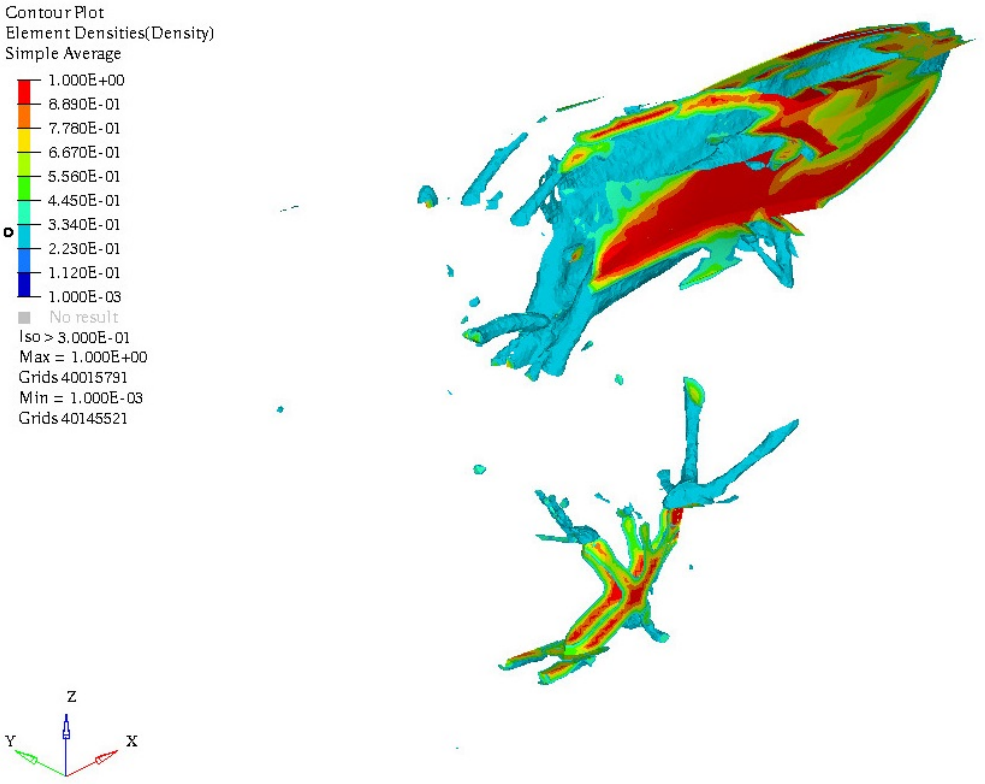

(b) Iso-metric isolated view

Figure 7.10: Compliance minimization under TSFC and OGV load constraints (MMO): iso-view of optimised structure

Like in other solutions, some meaningless structures are still present at convergence: this is evident in the upper appendix of the X-shape structure at the bottom or the semi-floating micro-structure between the two connections between fan case and aerodynamic surface of the cradle. These probably derive from numerical errors in optimization process, threshold filtering or even mistakes in symmetry constraint imposition by *Optistruct*.

In Fig. 7.11 convergence graphs are illustrated. As easily visible, solution is not converged at iteration 100: in fact, a continuation is automatically performed by the algorithm at iteration 92. Given that solution at iteration 91 is sufficiently stable (presenting a change rate in objective function below 0.1%) and in order not to use an exaggerated number of iterations, we can consider this density distribution as final solution. The only way to verify whether the obtained point is a local or the global minimum consists in performing multiple analysis from multiple starting points: being this computationally too expansive, we do not go deeper in this direction.

Until the moment of the great oscillation at iteration 92, the convergence history is typical of a TO problem with initially one violated constraint out of three.

Maximum compliance follows the shape of LCs 2018 and 2019 in Stow Configuration: this is a hint to the growing importance of these two face to the others, even LCs 1193 and 2192 in Reverse Configuration. After an initial reduction, a minimum is touched at iteration 5. After this, increase in objective function is slowed at iteration 9, because of the saturation of OGV bending load constraint: at this point, volume fraction is still violated and TSFC constraint still inactive. Then, objective function value augments, till saturation of volume fraction constraint, at iteration 30. Again, objective function decreases and TSFC constraints goes toward saturation, which will be reached at iteration 40. It is important to underline the fact that, despite the same limit on TSFC constraint was imposed on this problem and the one in Section 7.1.2, here TSFC constraint is active: this can be explained from the intervention of OGV bending load constraint, which, at optimality,

is antagonist to the former.

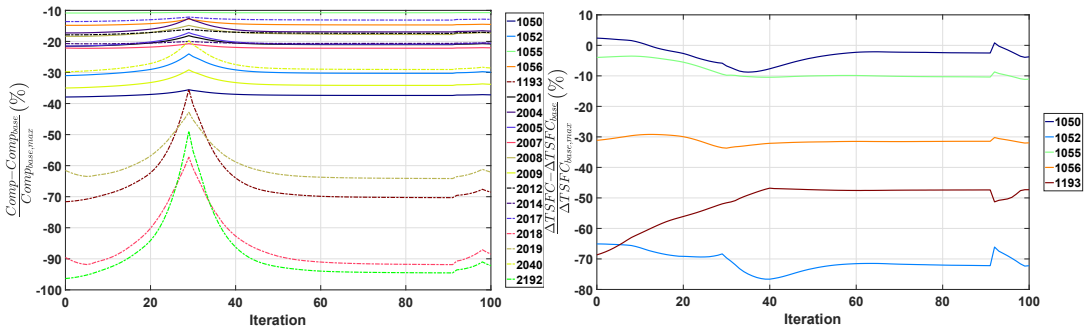

(a) Compliance history

(b) TSFC history

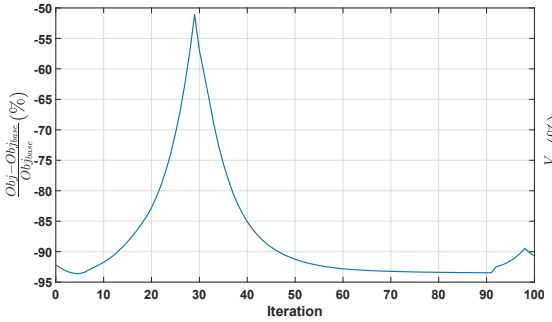

(c) Objective history

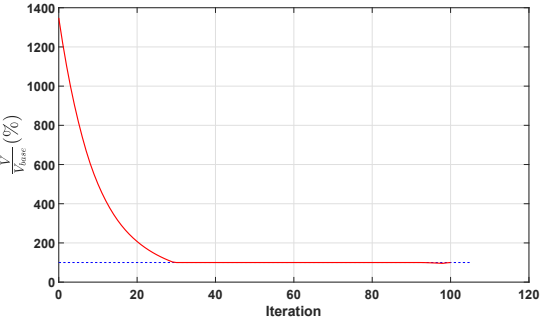

(d) Volume fraction history

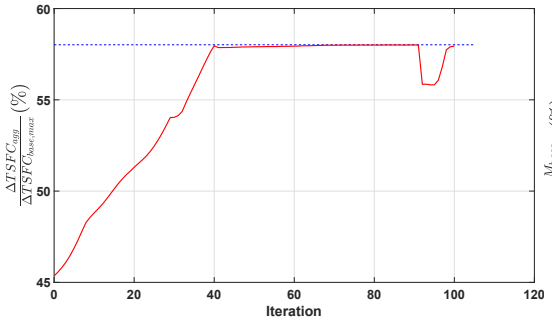

(e) TSFC aggregation history

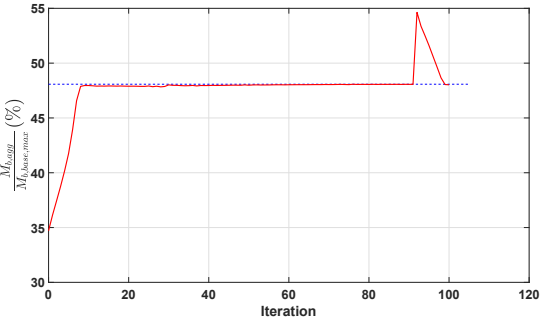

(f) OGV Load aggregation history

Figure 7.11: Compliance minimization under TSFC and OGV load constraints (MMO): convergence history

Looking at the performances of the optimal structure (see Fig. 7.12), we may observe that all responses, both structural and aerodynamic, are improved. In particular, the critical LCs are: 2018, 2019 (Stow Configuration), 1193, 2192 (Reverse Configuration) for compliance; almost all limit LCs for bending; 1052, 1056 (Stow Configuration) and 1193 (Reverse Configuration) for TSFC.

However, torsion loads are hugely increased: the max of this response becomes comparable to the bending component of OGV loads (in Fig. 7.12.d, both components are adimensioned with respect to baseline bending component).

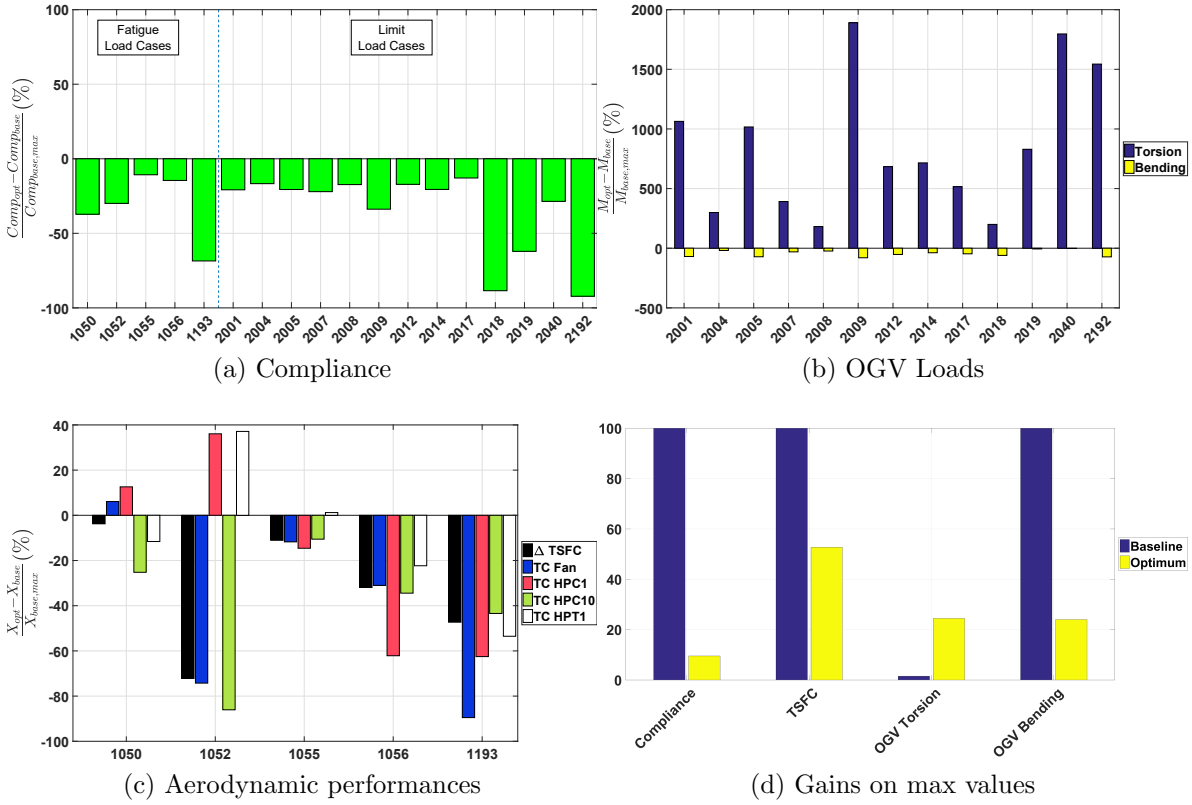

(a) Compliance (b) OGV Loads

(c) Aerodynamic performances (d) Gains on max values

Figure 7.12: Compliance minimization under TSFC and OGV load constraints (MMO): global gains

Choice of constraint aggregation formulation is not straight-forward: thus, a benchmark was performed (see Fig. 7.13) before exploiting the results in previous pages. It can be observed that both G_{KS} and G^l_{KS} provide a disconnected structure at the bottom, making the solutions useless. Moreover, links to turbine is totally missing in G_{KS} formulation, despite the conservative character of this latter.

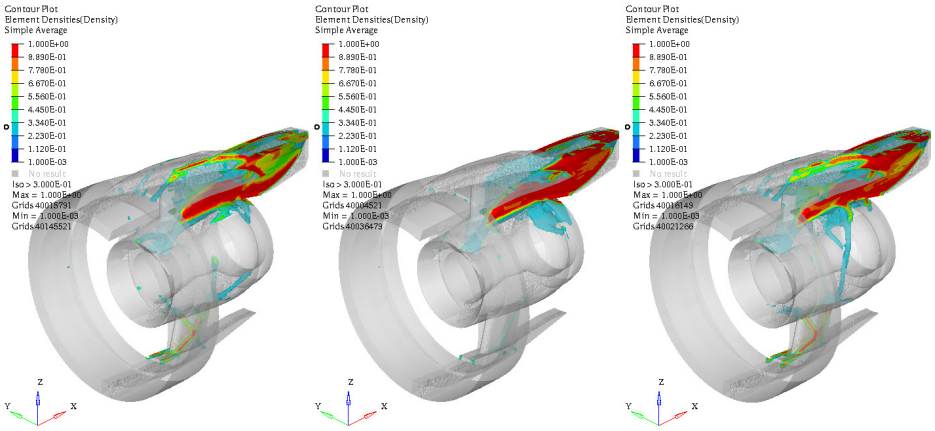

(a) Full view

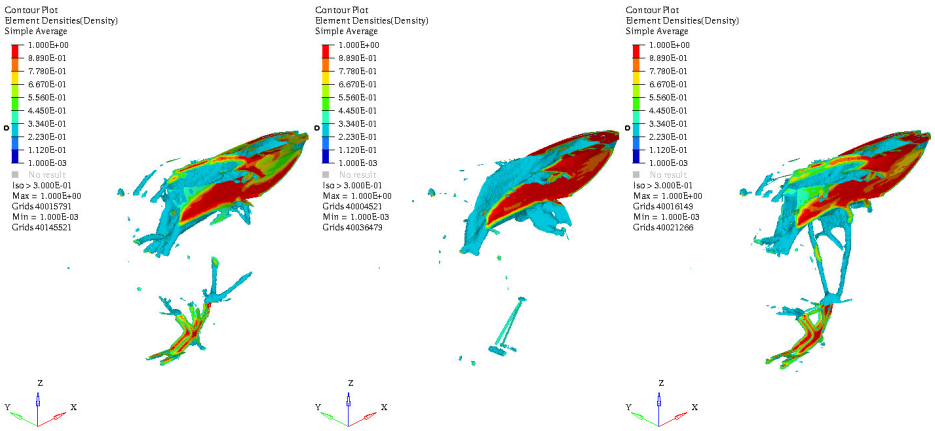

(b) Iso-metric isolated view

Figure 7.13: Compliance minimization under TSFC and OGV load constraints (MMO): results with different aggregation formulations (from left, $p-norm$, G^l_{KS} and G_KS)

7.2.2 OGV Loads Minimization

The original formulation in Eq. 5.6 does not produce a connected structure, as visible in Fig. 7.14. The resulting density distribution is based on local reinforcements, which are not integrated one to the other. In particular, the core of the engine itself appears suspended and disconnected from any other structure. This is due to the lack of a global constraint in TO problem. Therefore, history convergence and performance analysis are not reported for this simulation.

By modifying the original formulation, and introducing a new objective, some results can be extracted. In particular, in this section, the considered objective function is the maximum among bending loads on OGV in all limit LCs and compliances values in two configurations of the engine (taking into account all LCs). Results are displayed in Fig. 7.15.

The obtained structure is much simpler than the one in Section 7.2.1: there is a main box, connected to Front Engine Mount ring through two beams, to the IFS through four hinges on both sides and to turbine stages through an usually massive reinforcement (involving also IFS). Moreover, several supports on the engine and fan case appear. This constitutes an interesting solution because of the inner simplicity of the architecture.

7.2.3 TSFC Minimization

This simulation (treating problem in Eq. 5.7)essentially provides with a disconnected structure till iteration 100. The analysis is not restarted, given the little variations on objective function all along the optimization, and no post-processing of results is reported.

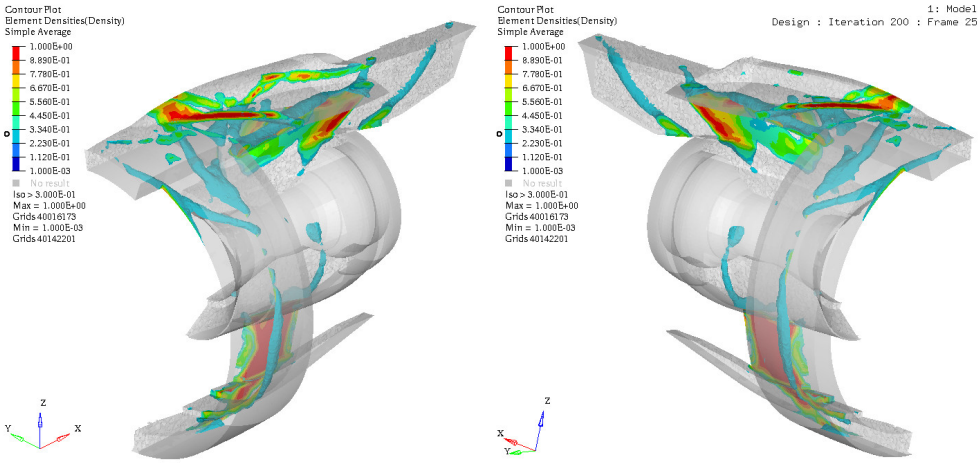

(a) Exploded view

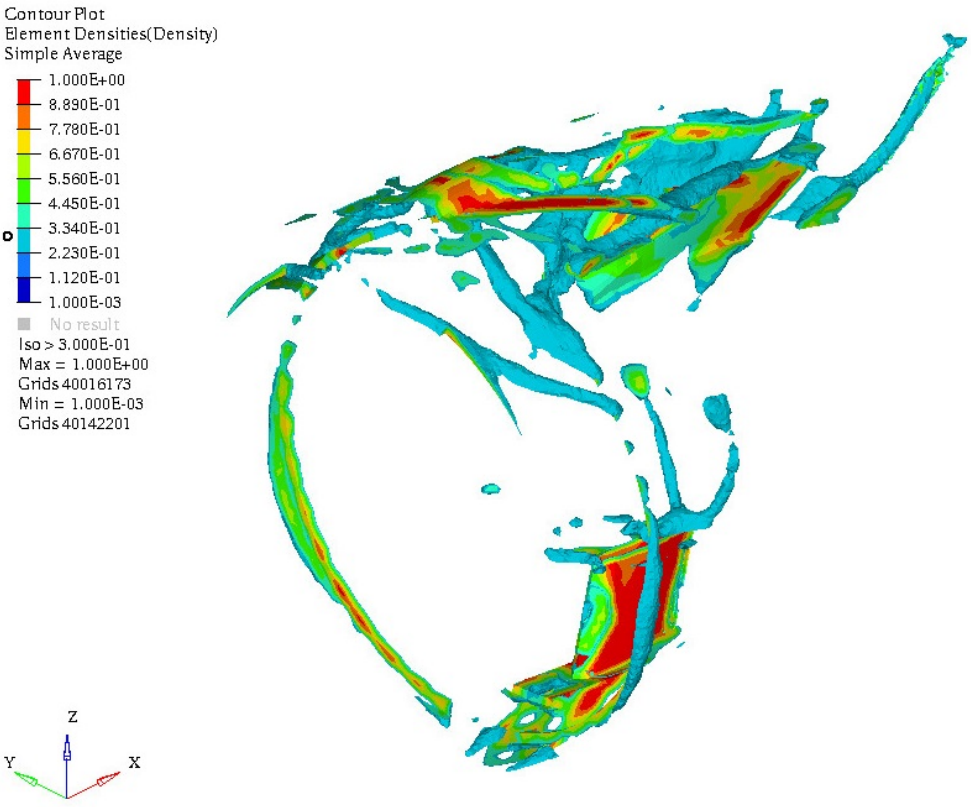

(b) Iso-metric isolated view

Figure 7.14: OGV loads minimization under TSFC constraint (MMO): iso-view of optimised structure

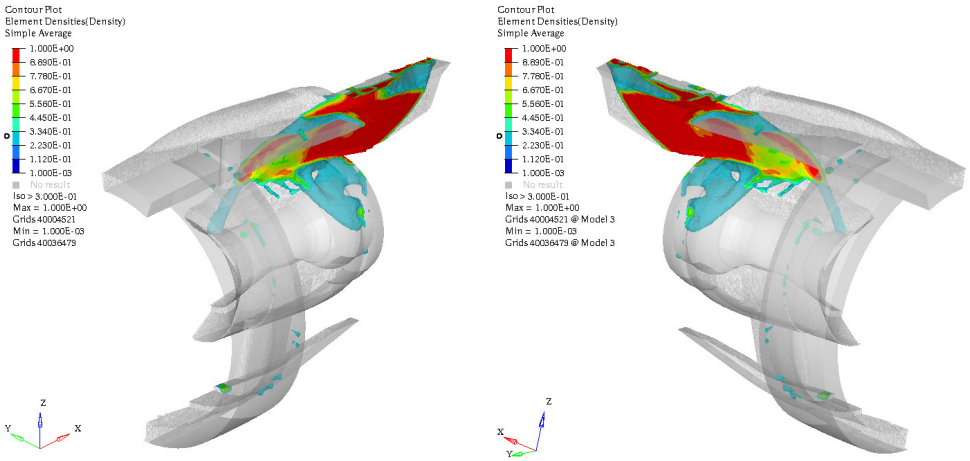

(a) Exploded view

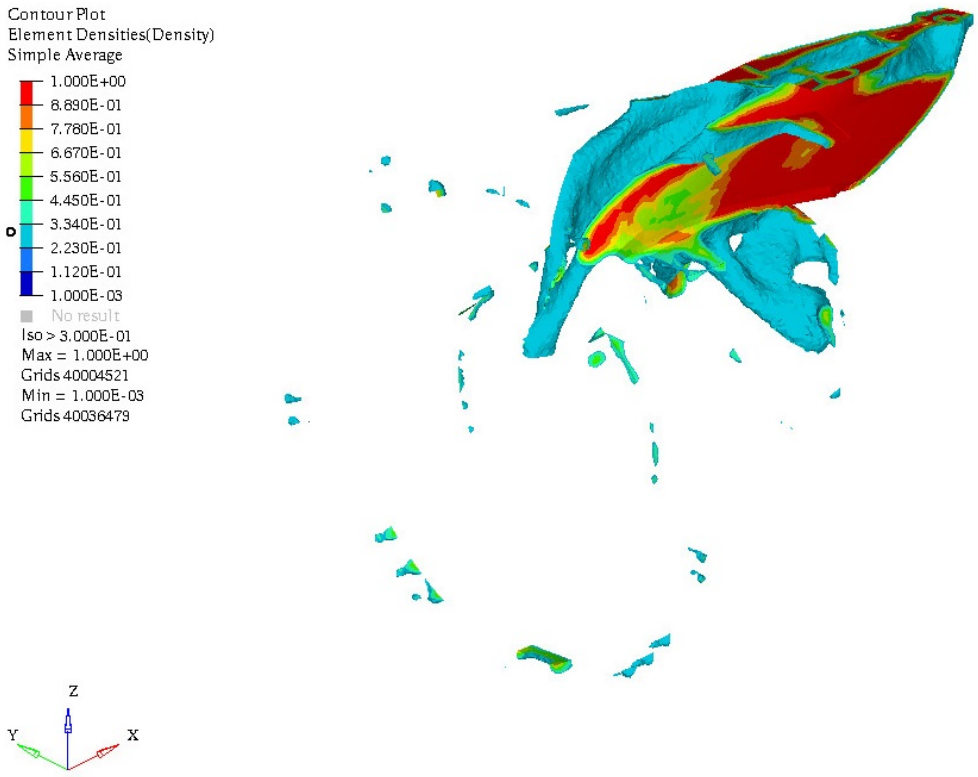

(b) Iso-metric isolated view

Figure 7.15: OGV loads/compliance minimization under TSFC constraint (MMO): iso-view of optimised structure

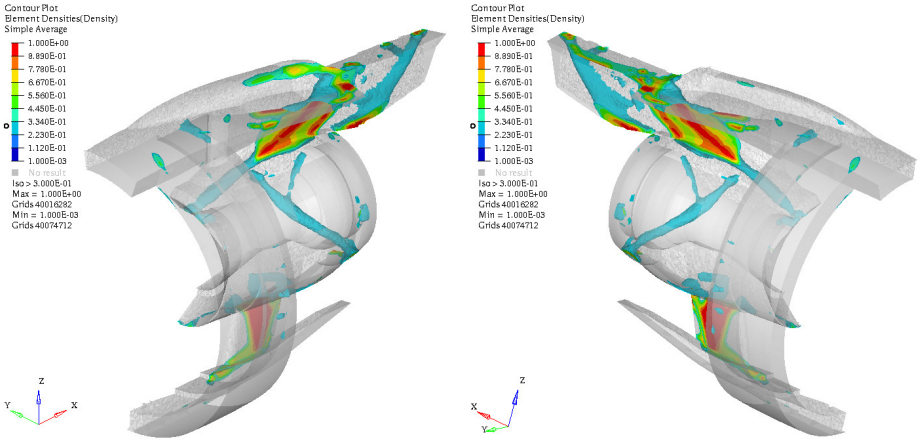

(a) Exploded view

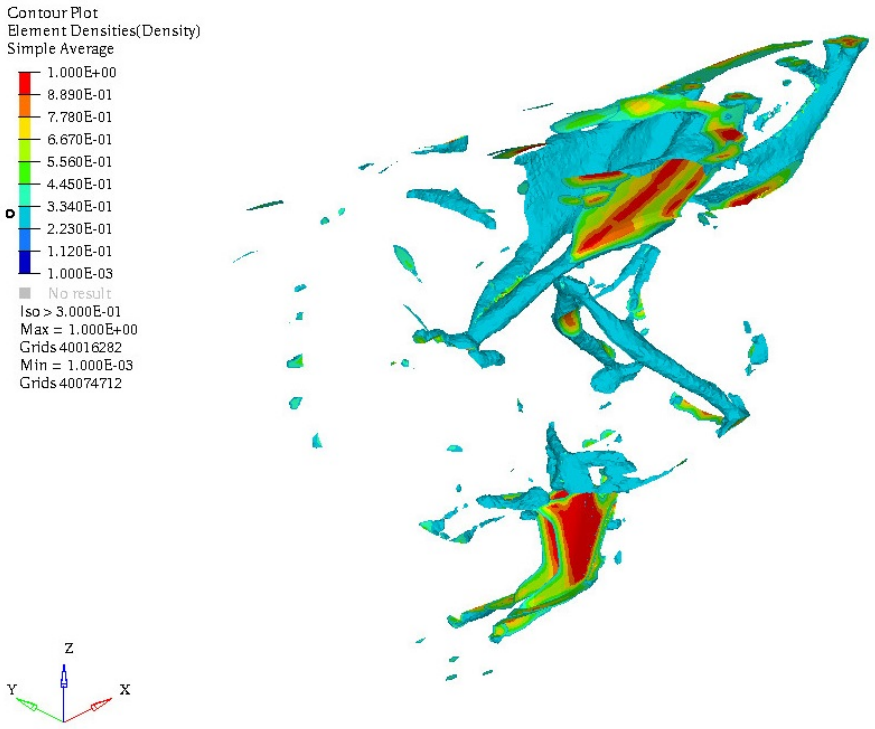

(b) Iso-metric isolated view

Figure 7.16: TSFC minimization under OGV loads constraint (MMO): iso-view of optimised structure

7.2.4 Compliance Minimization (under OGV load constraint)

In this Section, we ignore TSFC constraint in compliance minimization from Eq. 5.5. Results of the density distribution are reported in Fig. 7.17.

The optimal structure is almost identical to the one presented in Section 7.2.1. Few differences can be found by confronting Figg. 7.10 and 7.17:

- attack on turbine is more massive, but still conserves a division in multiple points;
- on the front, the quasi-horizontal beam on the engine mount ring is moved towards up, while attacks on the high-pressure compressor stages are reinforced;
- on the bottom, the connection between inferior sector of high-pressure compressor stages and lower fixed beams of TRU is interrupted at the crossing point on the aerodynamic surfaces of lower bi-fi, while individual components are weakened;
- new connections between DS and IFS appear on the top.

Convergence history and performance balance (not reported) are straightforward. The former is essentially identical to the one presented in Fig. 7.11. Looking at the global gains, it is obvious that compliances are improved (there is one less constraint), identical OGV loads (almost same structure with identical constraint imposition) and poorer aerodynamic performances (since TSFC is no more constrained).

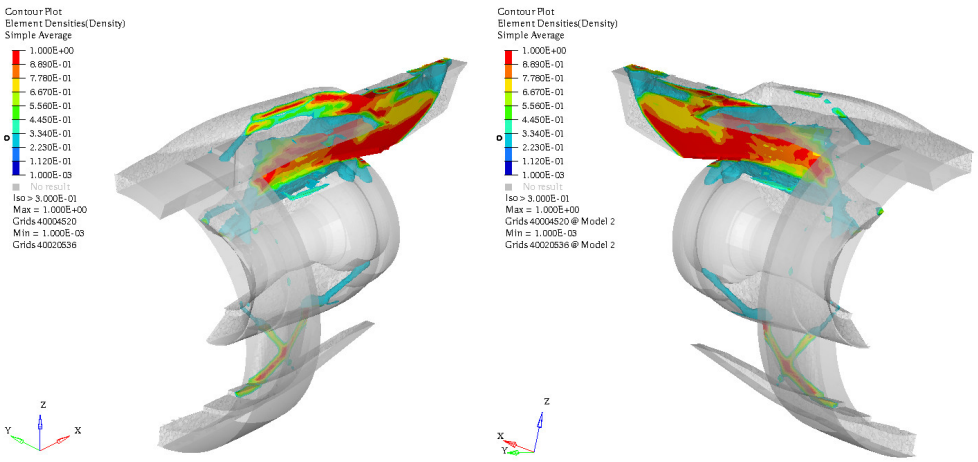

(a) Exploded view

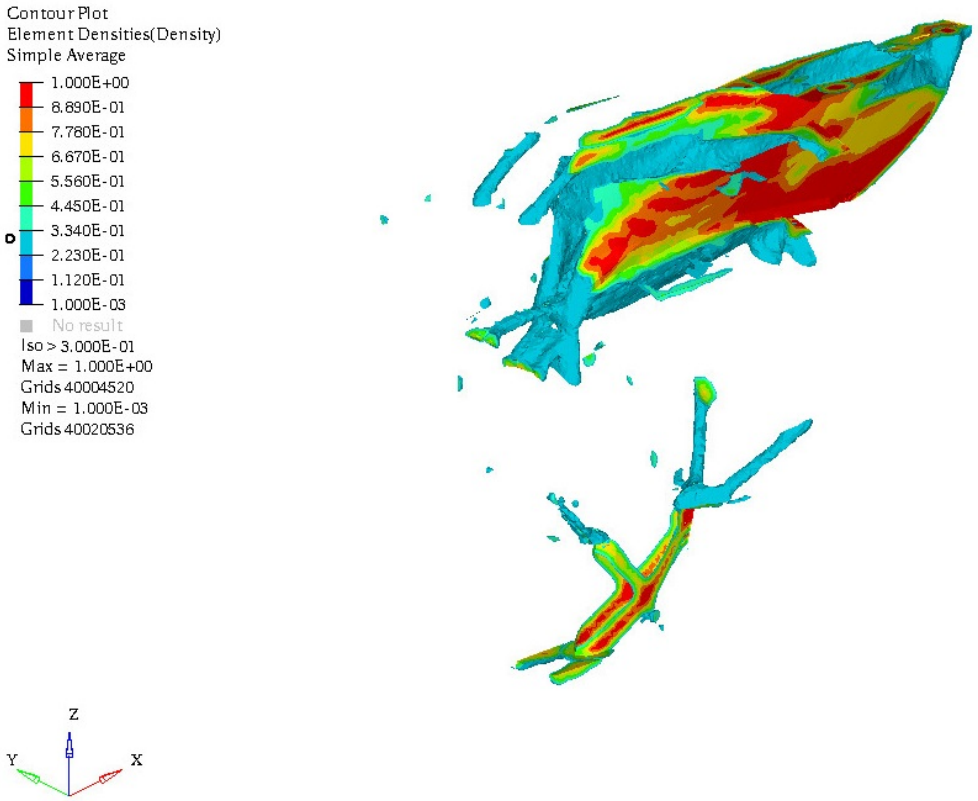

(b) Iso-metric isolated view

Figure 7.17: Compliance minimization under OGV loads constraint (MMO): iso-view of optimised structure

7.3 Pareto front

Once established the correct TO formulation, a Pareto front is to be determined, to deeply understand the effects of the imposed limits on the optimal solution. To this purpose, several variations on the values of all three constraints in Problem 5.5 (bending on OGV, TSFC and volume fraction) are here studied.

First of all, we modify the imposed limit on volume fraction. It is natural that with a superior quantity of material a better solution can be conceived: thus, the graph in Fig. 7.18 reflects this concept. However, in this case, augmenting volume fraction too much could lead to a stagnation of the objective function possible gains: in fact, given the fact that a huge percentage of loads comes from inertial phenomena, increasing the mass would also imply an increase in loads (and then in compliance).

It can be observed from TO results (cfr. Appendix B) that a reduction in volume fraction by 15% leads optimal structure to weaken attacks on IFS and the bottom connection with the Front Engine Mount. On the other side, by adding a 15% of mass, links on turbine are reinforced and become more massive, but still distinguishable in several points of attacks. By adding another 15%, these become very massive and indistinguishable; moreover, the connections between the lower fixed beams of TRU (typical of other simulations in previous chapters) are re-established.

This study is useful also because it allows to define a hierarchy among structures when it comes to translation into real architecture and consequent realization.

By variating TSFC limit value, the compliance does not see any huge variation. Moreover, in the correspondent graph (see Fig. 7.19), we observe that the point obtained by augmenting TSFC by 20% does not belong to the Pareto front, but is just a local minimum: in fact, the baseline point (at abscisse 100%) dominates it, since both compliance and TSFC are lower.

Looking at the obtained structures, differences are also very little and essentially involve attacks on turbine and Front Engine Mount: the general

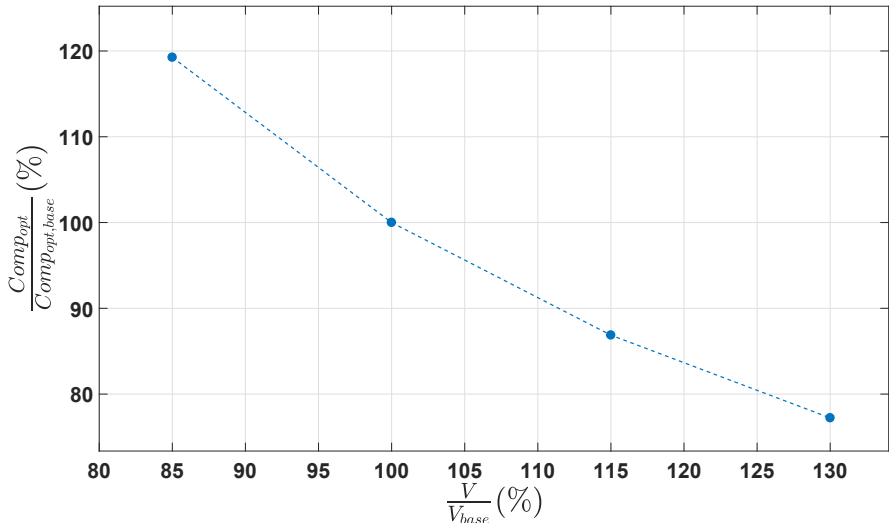

Figure 7.18: Pareto front: Compliance vs volume fraction constraint

rule is that both are reinforced by decreasing the limit on maximum TSFC allowed. However, structure appears poorly connected by the end of simulation: this is a hint to the fact that convergence is still far from arriving. A re-analysis with a superior number of maximum iterations would be computationally too expensive.

Finally, by tuning OGV bending limits, enormous changes in optimal compliances are registered (see Fig. 7.20), as well as in density distributions (cfr. Appendix B).

As general rule, direct connections between main box and inferior support are preferred to architecture involving the turbine (as in baseline case), when reducing the limit on OGV bending load. Moreover, attack on Front Engine Mount gets more and more massive, presenting also evident changes in shape.

It is important to underline the fact that, like for TSFC variation, a tighter limit reduces convergence rate.

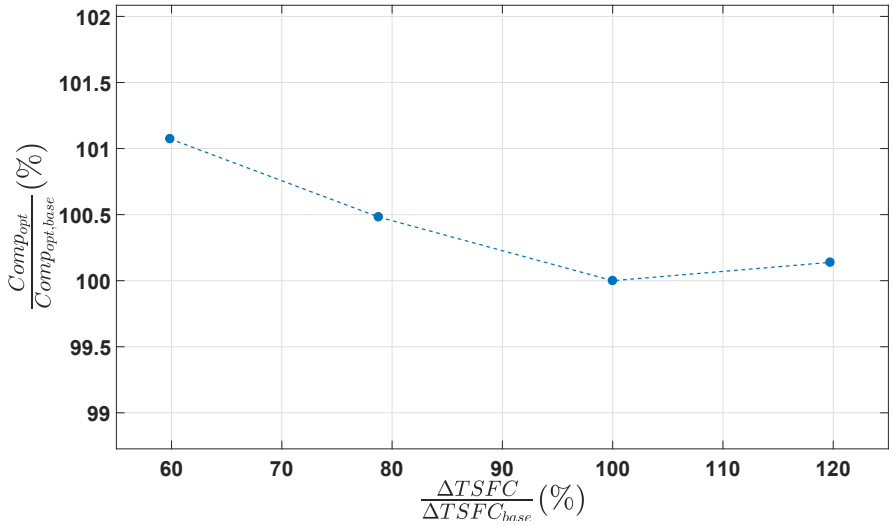

Figure 7.19: Pareto front: Compliance vs TSFC constraint

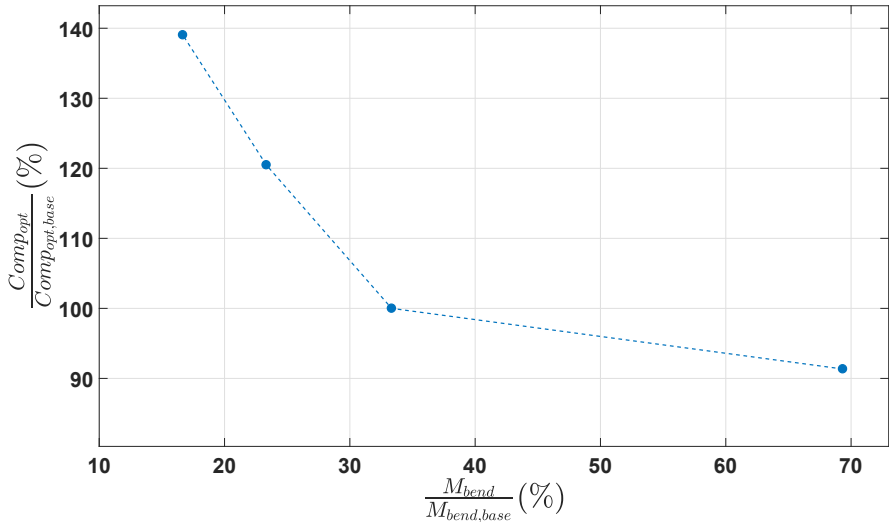

Figure 7.20: Pareto front: Compliance vs OGV bending constraint

Chapter 8

Conclusions

In the present study, a new problem regarding the Topology Optimization of the airframe of an Ultrafan Engine is presented and discussed. In the Literature review, several studies on Ultrafan Engines and Topology Optimization are briefly introduced, as well as a previous analogue study performed in 2018 that constitutes the starting point of the present internship in Airbus Operations SAS.

The problem has been defined in all its parts: Design Space, Boundary Conditions, interfaces between previous model and Design Space, optimization problems and constraints evaluations. The consequent model, developed in an *Optistruct* environment, has been illustrated, taking into account also the solidity of the base assumptions.

A number of analysis devoted to better understand the logic behind the pylon architecture design were performed. It has been shown that:

- built-in *MINMAX* tool in *Optistruct* environment does not provide a sufficiently good convergence rate of treated TO problems: an user-defined aggregation is a valuable alternative;

- $p-norm$ aggregation is the most suited for the problems treated and reported here, above all when introducing OGV bending load constraint;

- Stow configuration alone is not sufficient to obtain a stiff structure:

therefore, MMO is most suited for this kind of TO problem;

- results in Stow and MMO are very different, both in terms of effects of formulation itself (problem in Eq. 5.4 is sufficient in MMO, but not in Stow) and density distributions in final structures;

- all adopted formulations lead to a reduction of compliances in all LCs;

- compliance minimization can lead to a decrease in TSFC and an increase in both bending and torsion loads on OGVs;

- OGV bending load constraint introduction is necessary to control the global resistance of the structure, but does not provide a good limitation over torsion loads, as expected in previous analysis;

- torsion component of loads on OGV is increased and becomes comparable to bending component in optimal structure;

- a compliance minimization which takes into account volume fraction, TSFC (in fatigue LCs) and OGV bending load (in limit LCs) constraints is the most complete and suited formulation to the study;

- such an optimal structure presents a main box with numerous connections on turbine, Front Engine Mount Ring and IFS, involving the whole DS;

- these upper-mentioned connections can be approximated as a net of beams;

- all four considered responses in TO problem are antagonists in optimality conditions, allowing to trace a Pareto front;

- volume fraction and bending limits show a huge influence over compliance minimization results, while TSFC seems almost ineffective (if one only looks at objective variations).

Several aspects of the present study could be further investigated in future works.

First of all, successive analysis could integrate a finer mesh in Finite Element Model, in order to explore different solutions deriving from the refinement. A deeper study on High Performance Computing possibilities would prove beneficial to reduce computational time.

Secondly, adopting different kinematic hypothesis on contacts between DS and non-design region or selecting other TO scenarios could furnish totally different results.

Thirdly, a detailed post-processing of final results, including a free-body diagram could lead to a better understanding of load paths, thus to a translation of density distribution into a real structure.

Finally, an implementation of TO explicit methods would provide designs with a direct geometrical interpretation.

Appendix A

Tip clearances convergence

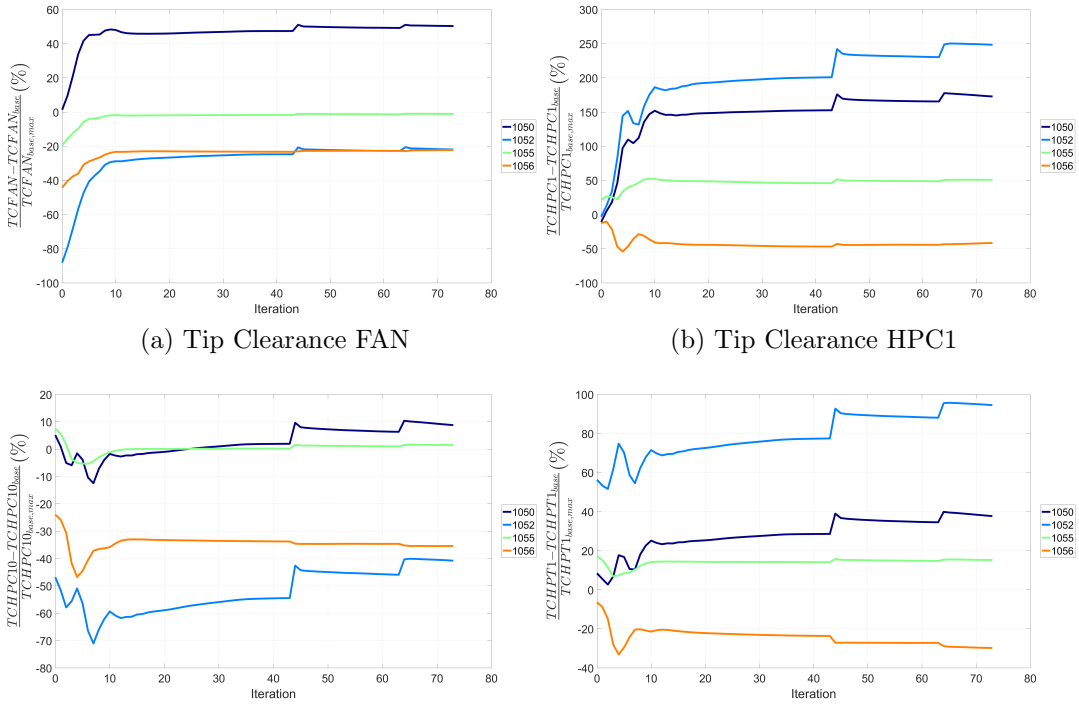

(a) Tip Clearance FAN

(b) Tip Clearance HPC1

(c) Tip Clearance HPC10

(d) Tip Clearance HPT1

Figure A.1: Classical Problem (with compliance aggregation, Stow): tip clearance convergence history

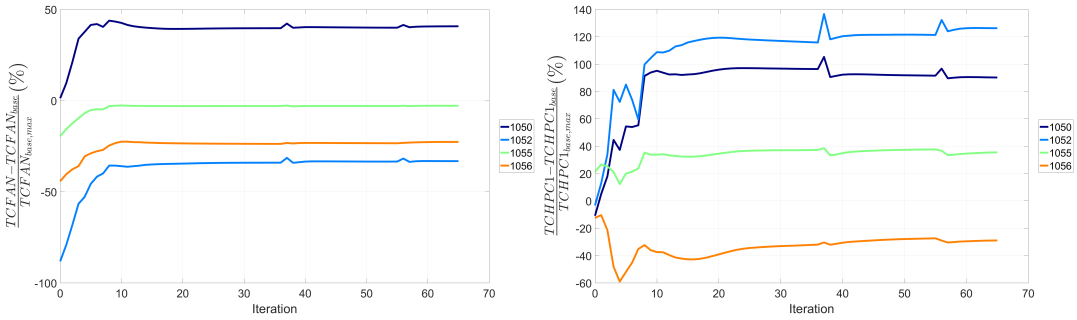

(a) Tip Clearance FAN

(b) Tip Clearance HPC1

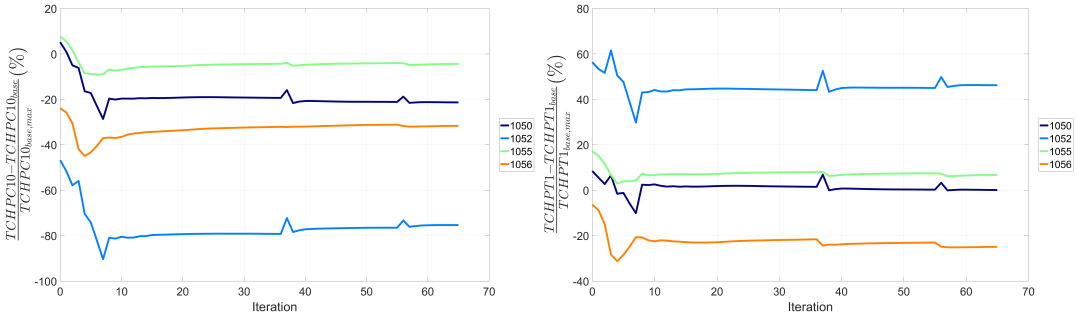

(c) Tip Clearance HPC10

(d) Tip Clearance HPT1

Figure A.2: Compliance minimization under TSFC constraint (Stow): tip clearance convergence history

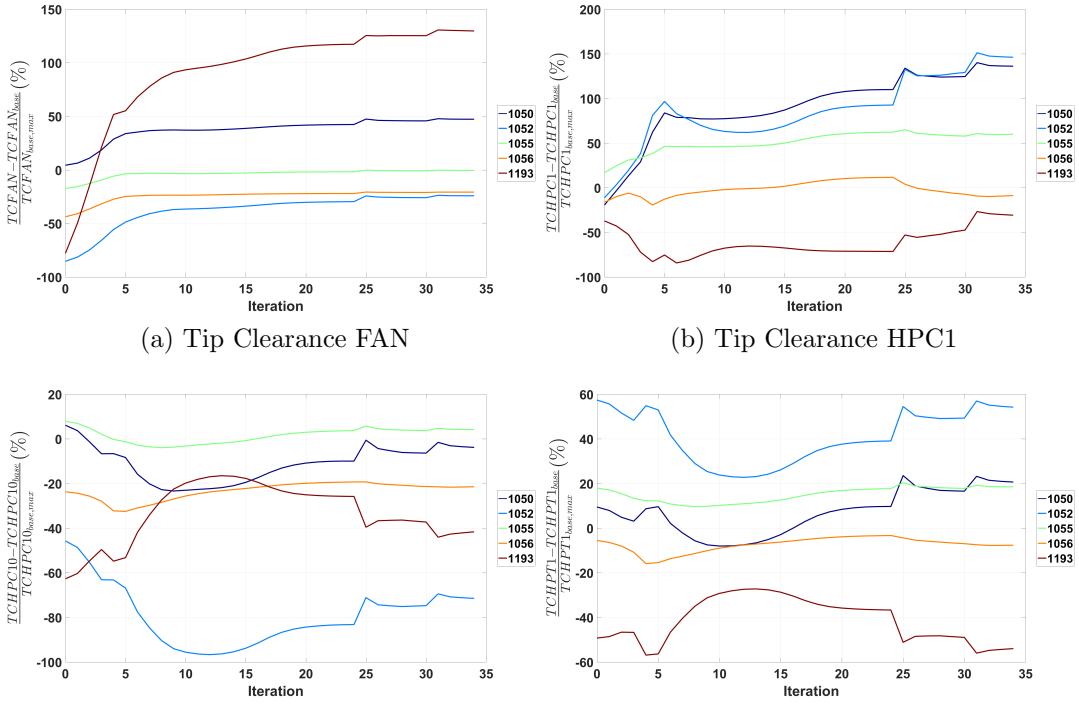

(a) Tip Clearance FAN

(b) Tip Clearance HPC1

(c) Tip Clearance HPC10

(d) Tip Clearance HPT1

Figure A.3: Classical Problem (MMO): tip clearance convergence history

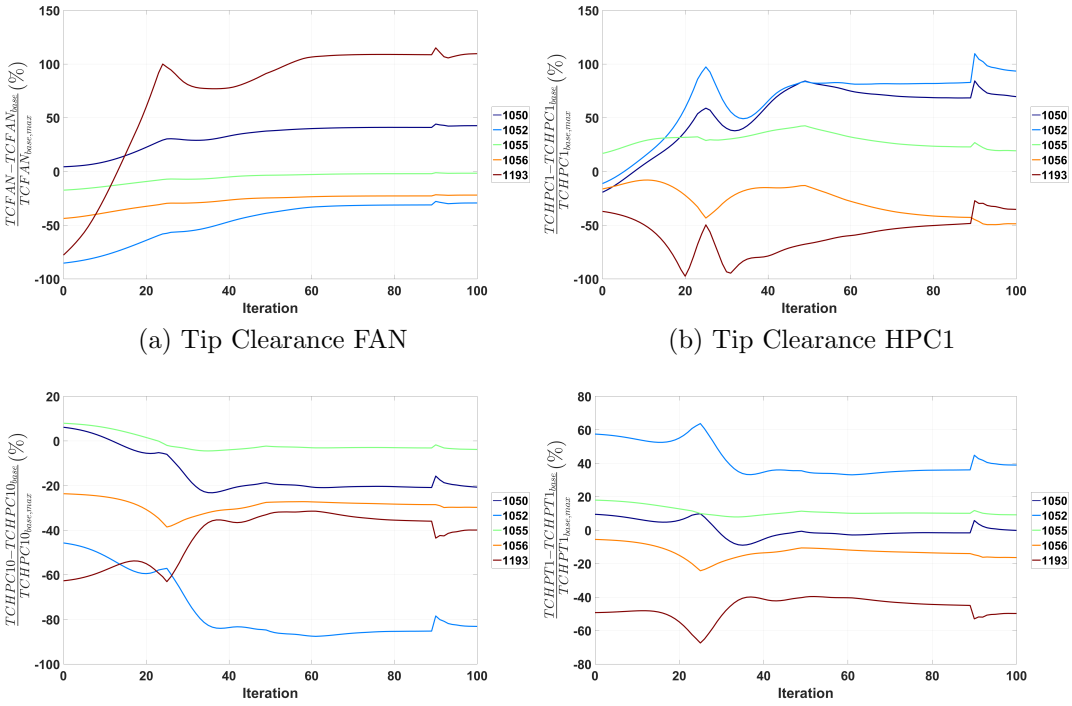

(a) Tip Clearance FAN

(b) Tip Clearance HPC1

(c) Tip Clearance HPC10

(d) Tip Clearance HPT1

Figure A.4: Compliance minimization under TSFC constraint (MMO): tip clearance convergence history

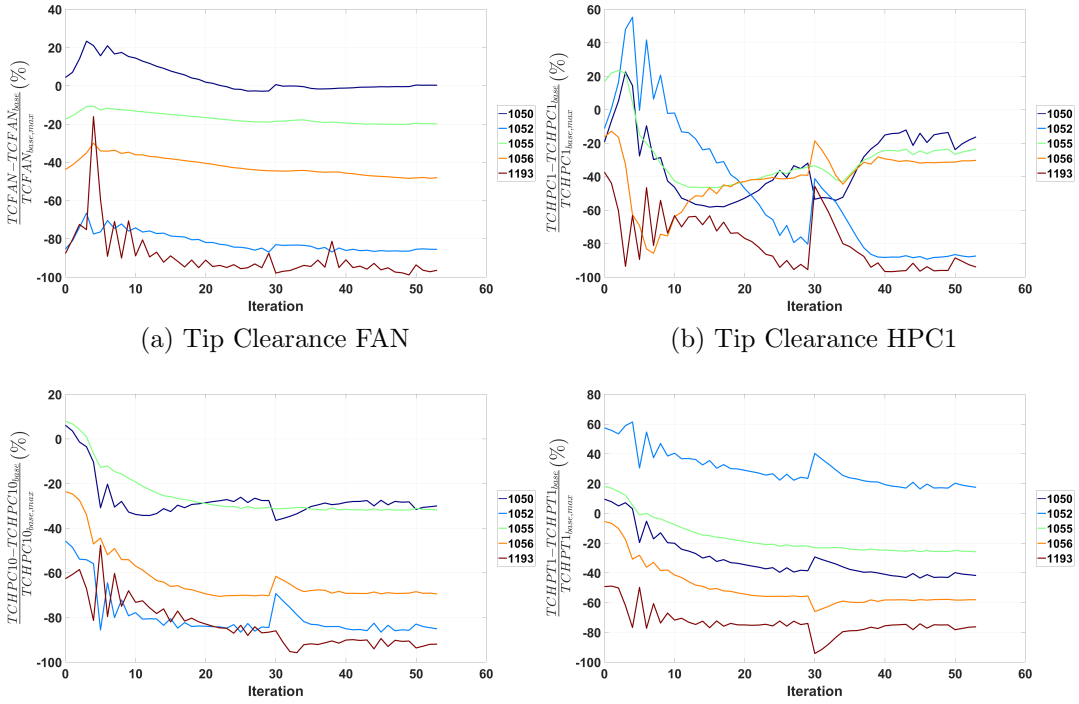

(a) Tip Clearance FAN

(b) Tip Clearance HPC1

(c) Tip Clearance HPC10

(d) Tip Clearance HPT1

Figure A.5: TSFC minimization (MMO): tip clearance convergence history

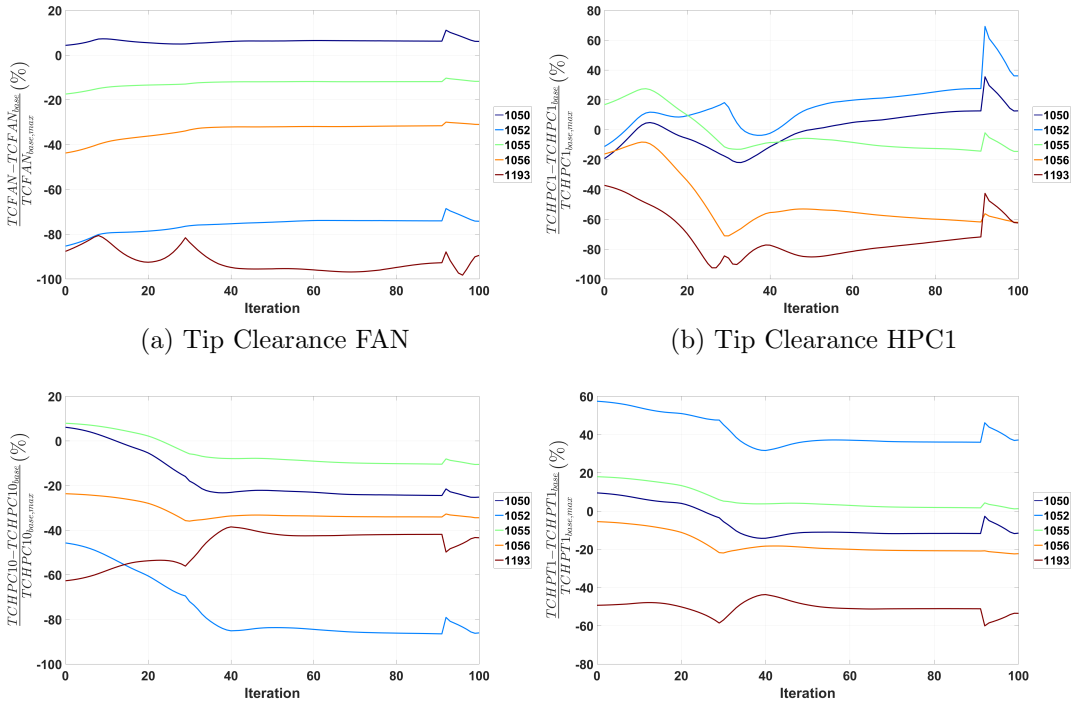

(a) Tip Clearance FAN

(b) Tip Clearance HPC1

(c) Tip Clearance HPC10

(d) Tip Clearance HPT1

Figure A.6: Compliance minimization (complete formulation MMO): tip clearance convergence history

Appendix B

Optimal Structures in Pareto front

Structures described in Chapter 7.3 are here illustrated. Convergence history is not reported.

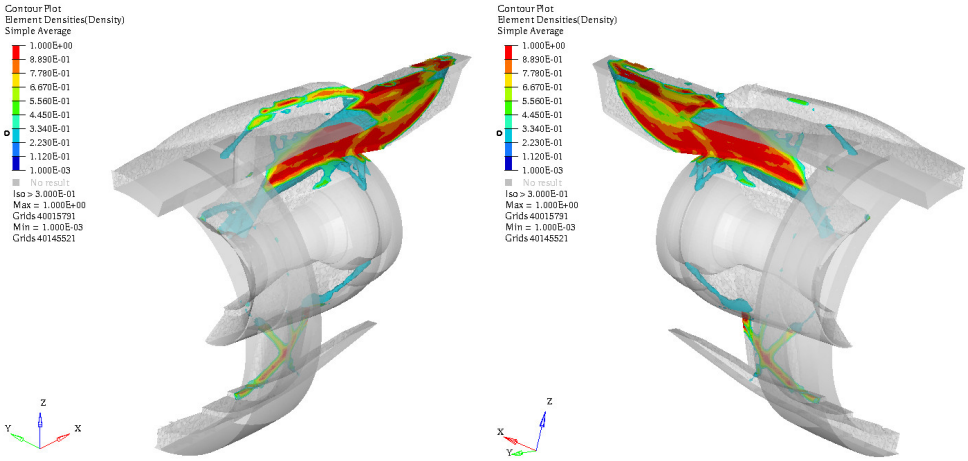

(a) Exploded view

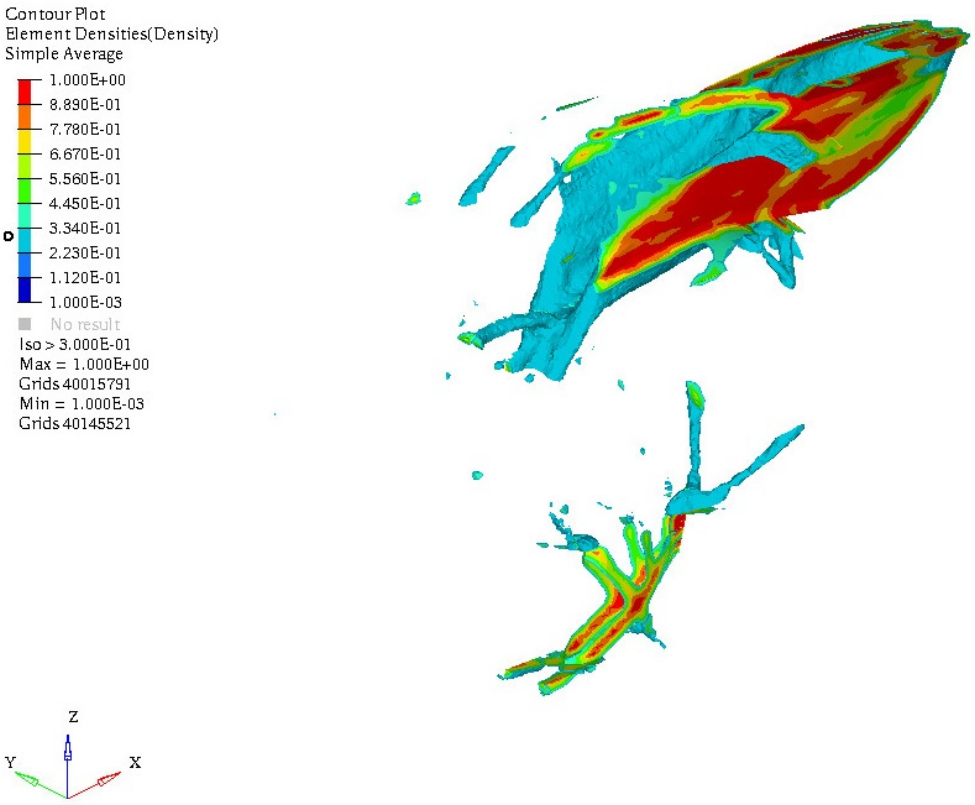

(b) Iso-metric isolated view

Figure B.1: Pareto front ($V = 0.85\ V_0$): iso-view of optimised structure

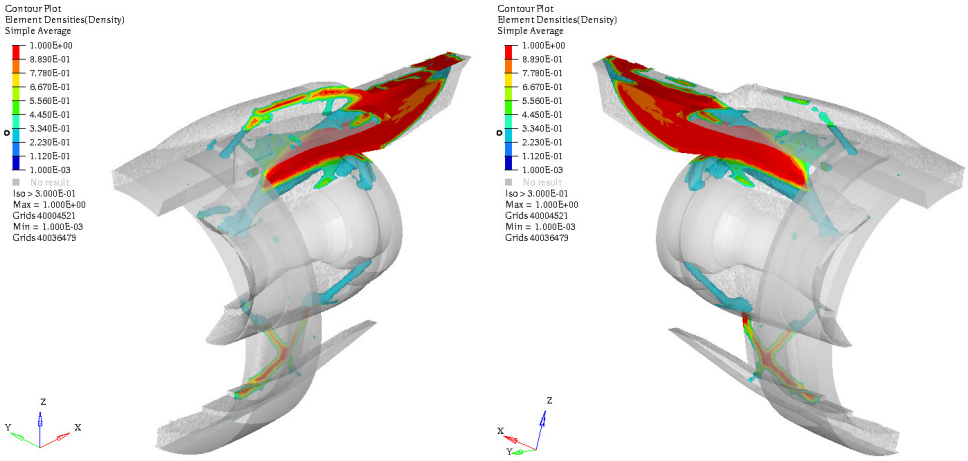

(a) Exploded view

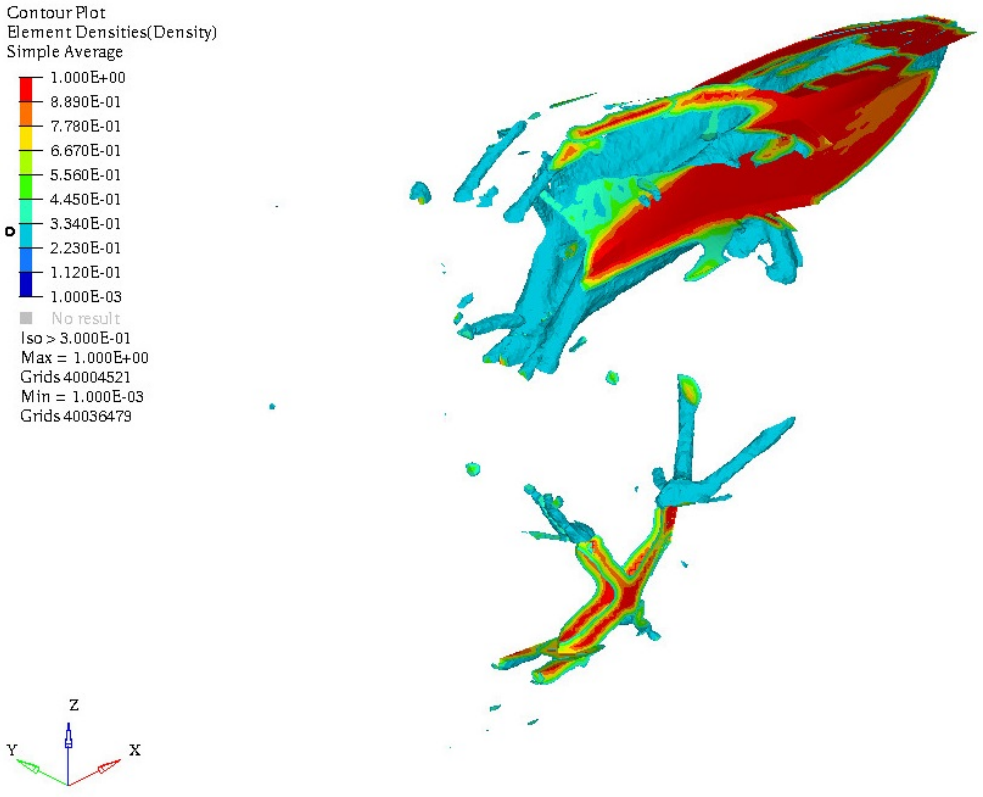

(b) Iso-metric isolated view

Figure B.2: Pareto front ($V = 1.15\ V_0$): iso-view of optimised structure

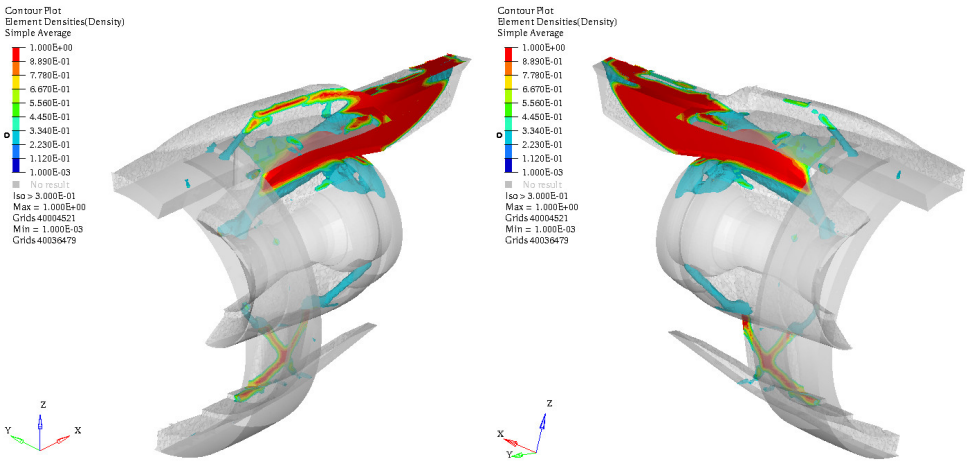

(a) Exploded view

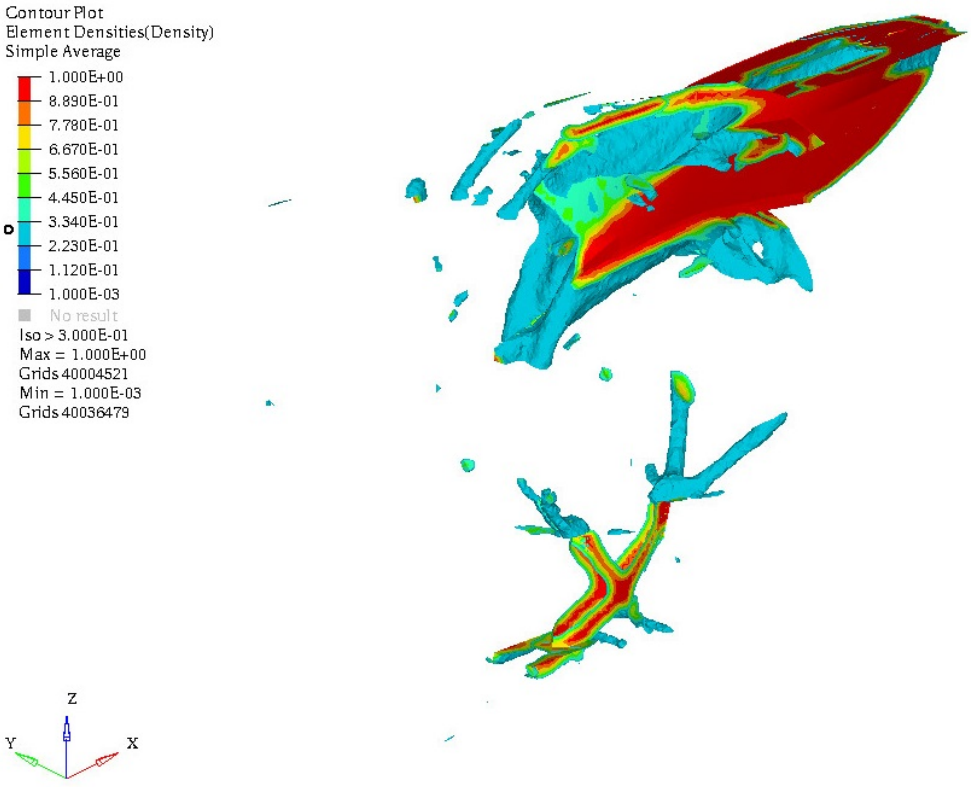

(b) Iso-metric isolated view

Figure B.3: Pareto front ($V = 1.3\,V_0$): iso-view of optimised structure

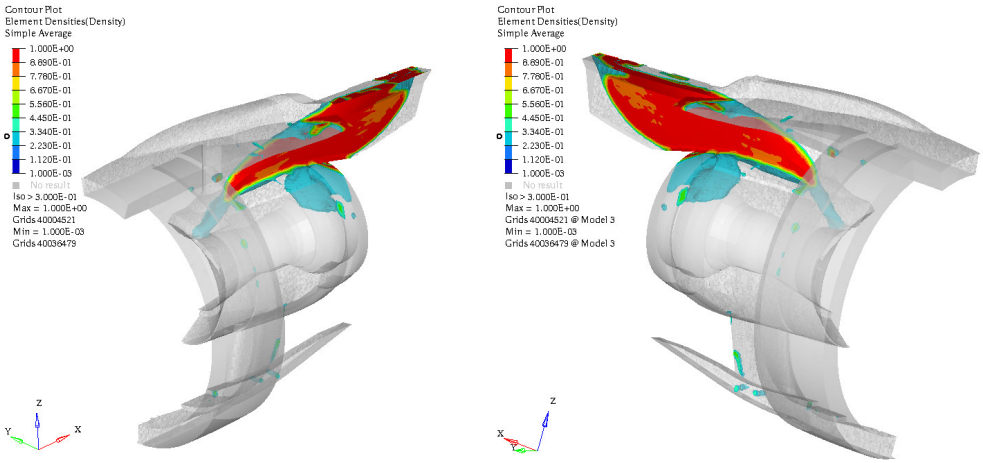

(a) Exploded view

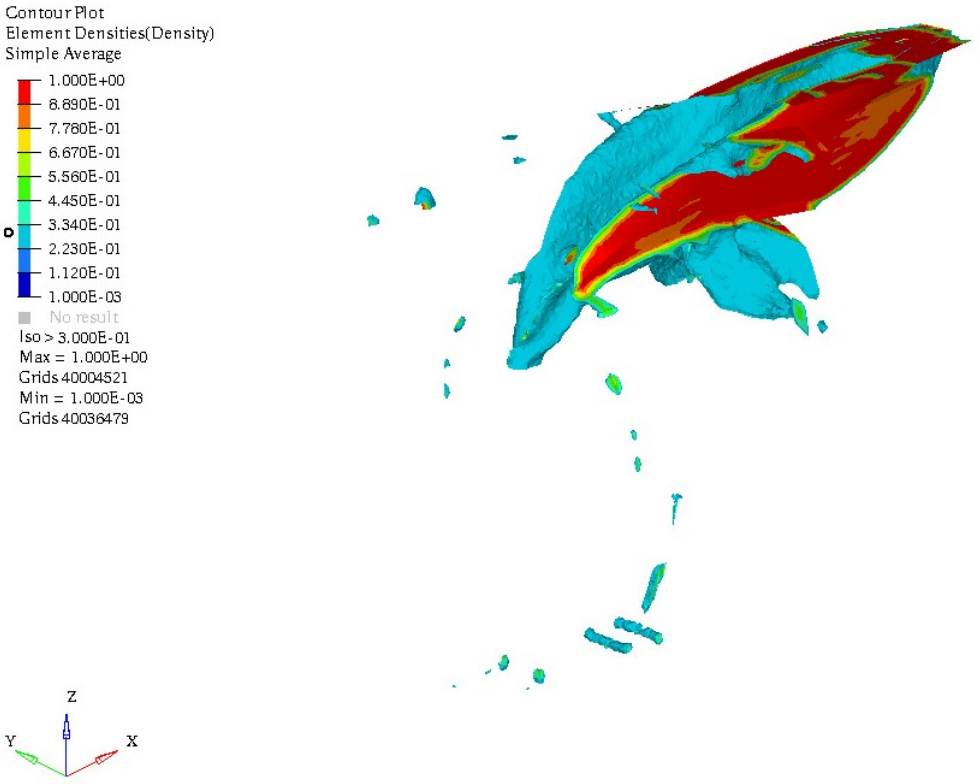

(b) Iso-metric isolated view

Figure B.4: Pareto front ($M = 2\,M_0$): iso-view of optimised structure

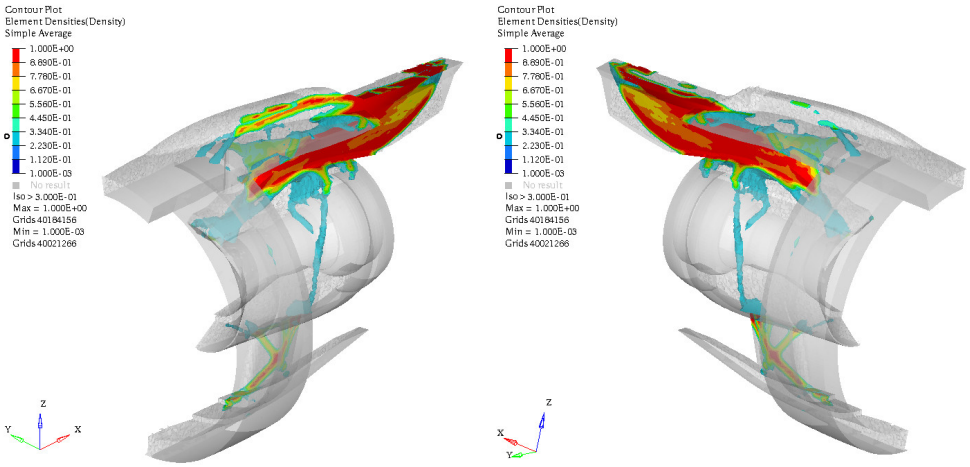

(a) Exploded view

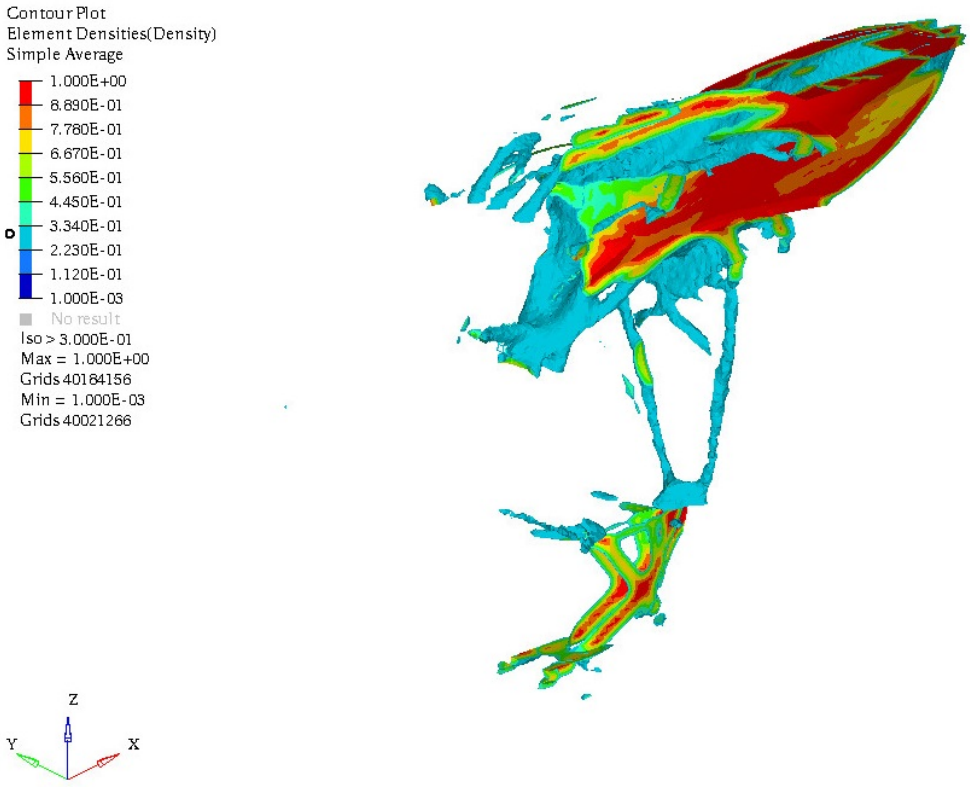

(b) Iso-metric isolated view

Figure B.5: Pareto front ($M = 0.7\ M_0$): iso-view of optimised structure

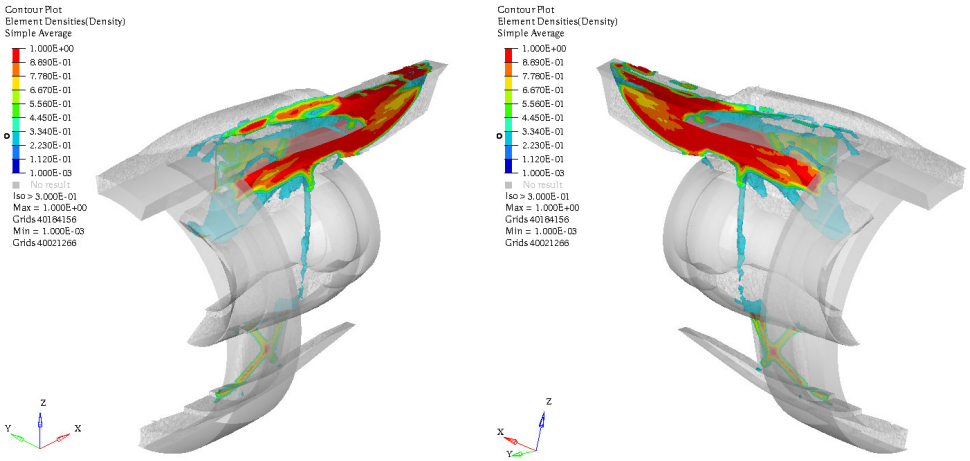

(a) Exploded view

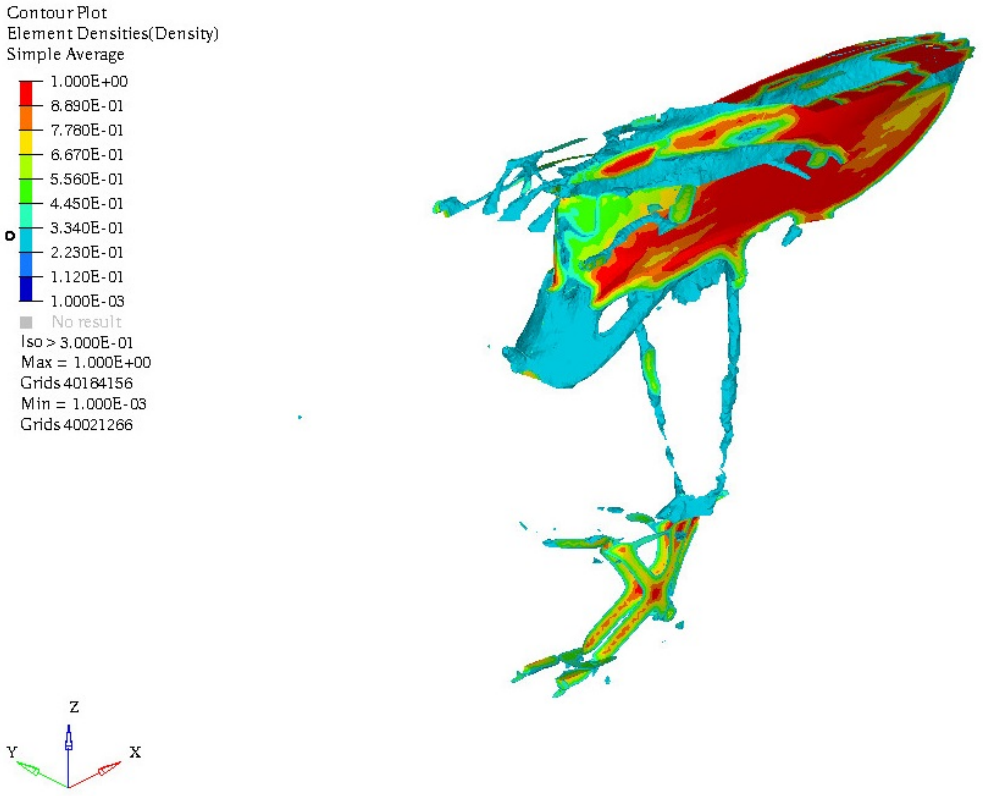

(b) Iso-metric isolated view

Figure B.6: Pareto front ($M = 0.5\ M_0$): iso-view of optimised structure

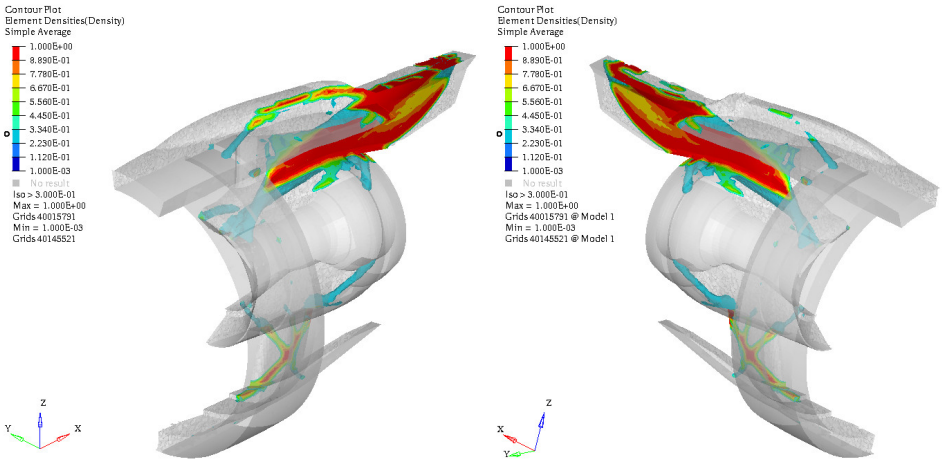

(a) Exploded view

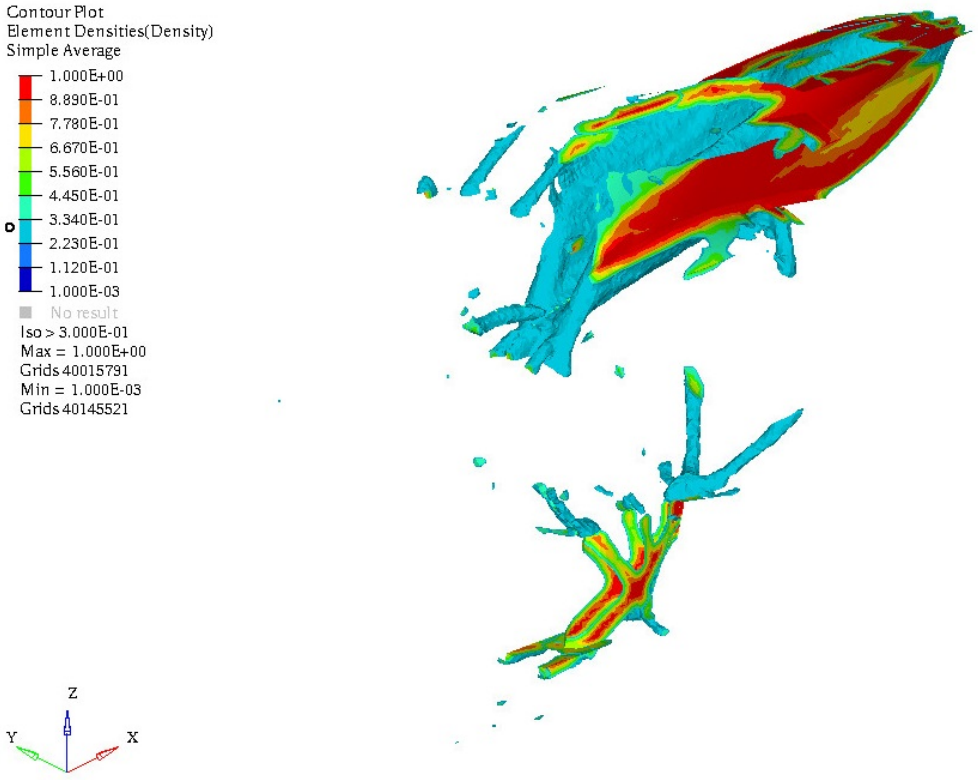

(b) Iso-metric isolated view

Figure B.7: Pareto front ($TSFC = 1.2\ TSFC_0$): iso-view of optimised structure

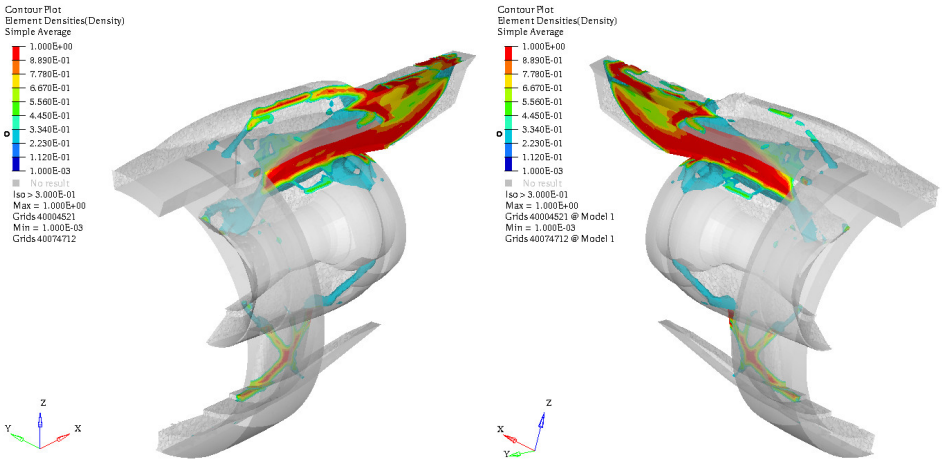

(a) Exploded view

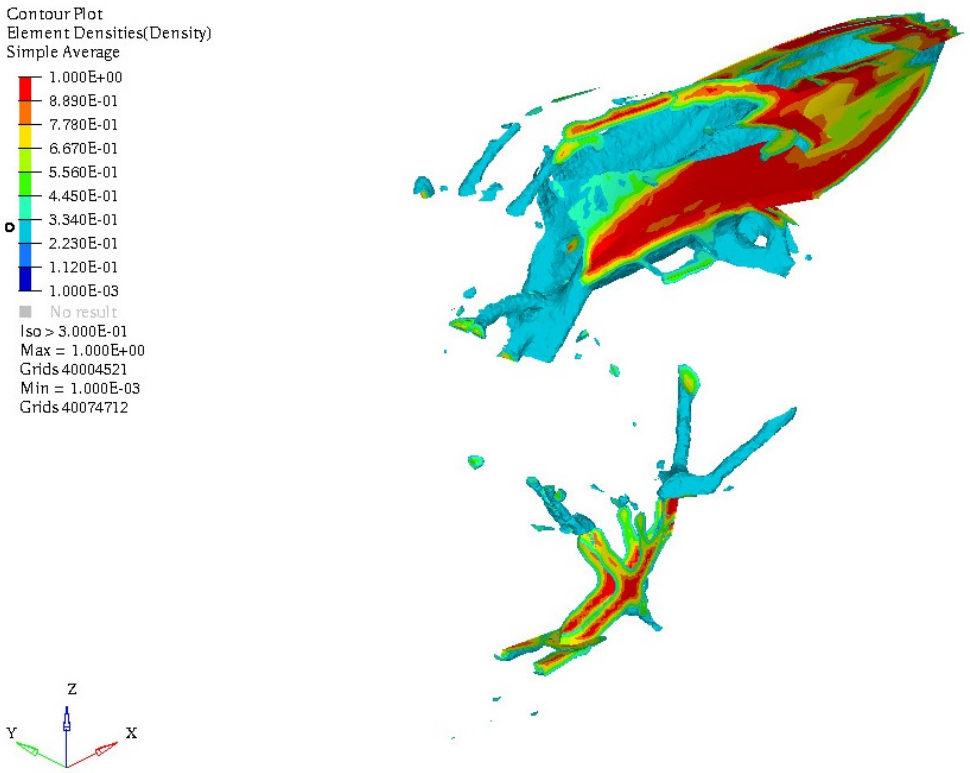

(b) Iso-metric isolated view

Figure B.8: Pareto front ($TSFC = 0.8\ TSFC_0$): iso-view of optimised structure

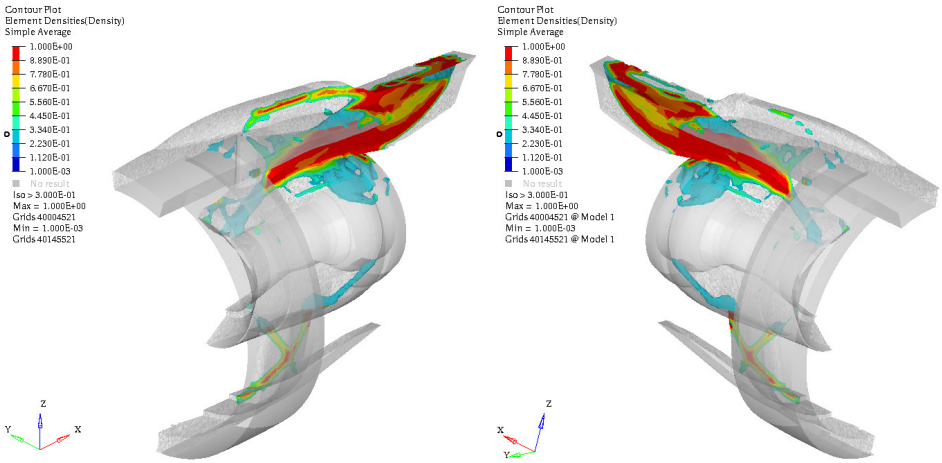

(a) Exploded view

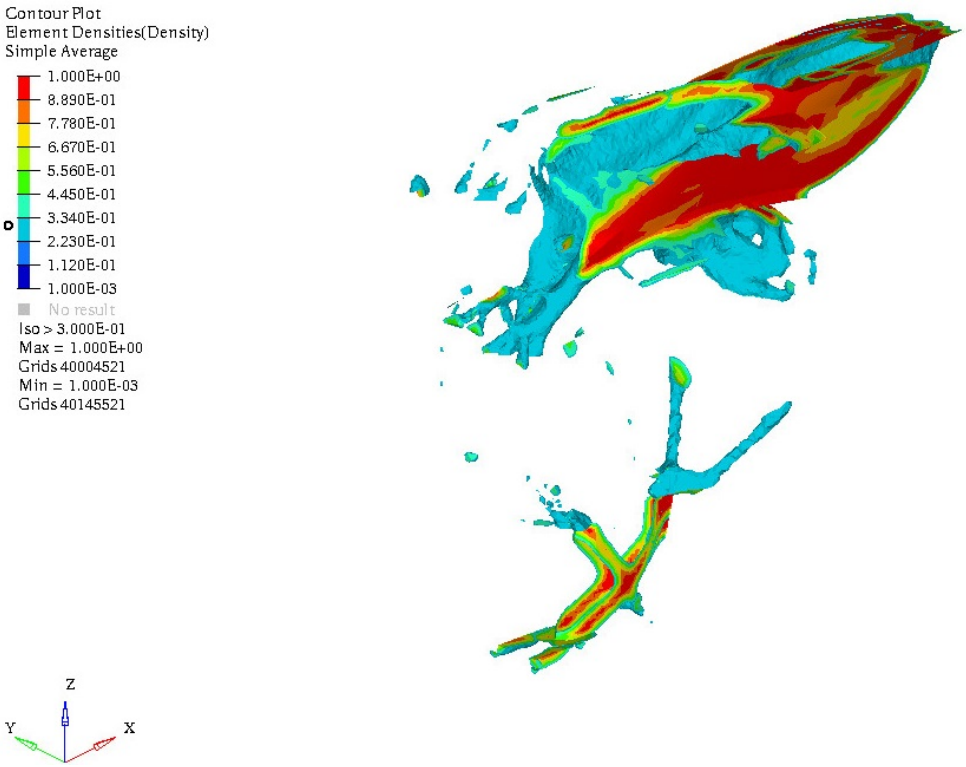

(b) Iso-metric isolated view

Figure B.9: Pareto front ($TSFC = 0.6\ TSFC_0$): iso-view of optimised structure

Appendix C

Tabular Results

CONF.	CATEGORY	ID	$\Delta Comp$ (%)	$\Delta TSFC$ (%)	ΔM_x (%)	ΔM_{bend} (%)
Stow	Fatigue	1050	-37.39	30.06		
Stow	Fatigue	1052	-30.31	-38.74		
Stow	Fatigue	1055	-10.75	7.01		
Stow	Fatigue	1056	-14.62	-15.84		
Stow	Limit	2001	-21.02		716.73	-41.25
Stow	Limit	2004	-16.85		141.38	-18.70
Stow	Limit	2005	-20.87		671.57	-43.29
Stow	Limit	2007	-22.12		218.46	-21.32
Stow	Limit	2008	-17.53		20.91	-20.71
Stow	Limit	2009	-34.19		1363.19	-42.20
Stow	Limit	2012	-17.28		334.15	-46.32
Stow	Limit	2014	-20.60		460.12	-22.45
Stow	Limit	2017	-13.00		211.38	-39.36
Stow	Limit	2018	-91.36		187.40	-57.20
Stow	Limit	2019	-63.98		247.56	3.62
Stow	Limit	2040	-29.03		1346.74	10.18
Reverse	Fatigue	1193	-70.18	-18.76		
Reverse	Limit	2192	-94.41		436.24	141.93

Table C.1: Tabular results of Classical problem (MMO): relative variations

CONF.	CATEGORY	ID	$\Delta Comp$ (%)	$\Delta TSFC$ (%)	ΔM_x (%)	ΔM_{bend} (%)
Stow	Fatigue	1050	-35.02	-11.70		
Stow	Fatigue	1052	-24.77	-79.79		
Stow	Fatigue	1055	-10.29	-21.43		
Stow	Fatigue	1056	-11.92	-47.19		
Stow	Limit	2001	-17.30		855.20	-74.70
Stow	Limit	2004	-12.91		-1.63	-15.37
Stow	Limit	2005	-16.35		774.89	-77.10
Stow	Limit	2007	-19.09		226.98	-35.64
Stow	Limit	2008	-9.02		262.49	-12.86
Stow	Limit	2009	-28.92		1647.21	-85.01
Stow	Limit	2012	-13.10		958.81	-37.01
Stow	Limit	2014	-18.58		558.40	-43.41
Stow	Limit	2017	-10.10		757.10	-33.95
Stow	Limit	2018	15.51		2924.93	49.21
Stow	Limit	2019	-1.73		3366.41	89.98
Stow	Limit	2040			1512.85	2.19
Reverse	Fatigue	1193	-42.05	-83.97		
Reverse	Limit	2192	-57.49		1339.72	-41.30

Table C.2: Tabular results of TSFC minimization (MMO): relative variations

CONF.	CATEGORY	ID	$\Delta Comp$ (%)	$\Delta TSFC$ (%)	ΔM_x (%)	ΔM_{bend} (%)
Stow	**Fatigue**	**1050**	**-37.21**	**-3.75**		
Stow	**Fatigue**	**1052**	**-29.91**	**-72.22**		
Stow	**Fatigue**	**1055**	**-10.73**	**-11.06**		
Stow	**Fatigue**	**1056**	**-14.53**	**-31.94**		
Stow	**Limit**	**2001**	**-20.82**		**1063.50**	**-69.48**
Stow	**Limit**	**2004**	**-16.69**		**299.59**	**-18.91**
Stow	**Limit**	**2005**	**-20.62**		**1016.76**	**-71.52**
Stow	**Limit**	**2007**	**-22.06**		**391.77**	**-30.47**
Stow	**Limit**	**2008**	**-17.32**		**181.33**	**-23.51**
Stow	**Limit**	**2009**	**-33.82**		**1890.37**	**-80.11**
Stow	**Limit**	**2012**	**-17.14**		**683.96**	**-52.08**
Stow	**Limit**	**2014**	**-20.55**		**715.85**	**-37.87**
Stow	**Limit**	**2017**	**-12.90**		**515.84**	**-46.81**
Stow	**Limit**	**2018**	**-88.49**		**199.82**	**-60.13**
Stow	**Limit**	**2019**	**-62.08**		**829.66**	**-5.80**
Stow	**Limit**	**2040**	**-28.56**		**1796.61**	**-2.34**
Reverse	**Fatigue**	**1193**	**-68.53**	**-47.31**		
Reverse	**Limit**	**2192**	**-92.20**		**1543.82**	**-72.45**

Table C.3: Tabular results of complete formulation: relative variations

References

[1] B. McKay and A. Barlow, "The UltraFan engine and aircraft based thrust reversing," in *48th AIAA/ASME/SAE/ASEE Joint Propulsion Conference & Exhibit*. American Institute of Aeronautics and Astronautics, jul 2012.

[2] S. Lattime and B. Steinetz, "Turbine engine clearance control systems: Current practices and future directions," in *38th AIAA/ASME/SAE/ASEE Joint Propulsion Conference & Exhibit*. American Institute of Aeronautics and Astronautics, jul 2002.

[3] C. Hughes, D. V. Zante, and J. Heidmann, "Aircraft engine technology for green aviation to reduce fuel burn," in *3rd AIAA Atmospheric Space Environments Conference*. American Institute of Aeronautics and Astronautics, jun 2011.

[4] J. R. Hooker, A. Wick, C. H. Zeune, and A. Agelastos, "Over wing nacelle installations for improved energy efficiency," in *31st AIAA Applied Aerodynamics Conference*. American Institute of Aeronautics and Astronautics, jun 2013.

[5] G. Krishnan, C. Perullo, and D. N. Mavris, "An assessment of relative technology benefits of a variable pitch fan and variable area nozzle," in *49th AIAA/ASME/SAE/ASEE Joint Propulsion Conference*. American Institute of Aeronautics and Astronautics, jul 2013.

[6] X. Yang, H. Tang, and M. Chen, "Performance modeling and optimization assessment of variable pitch fan for ultrafan engine," in *2018 Joint Propulsion Conference*. American Institute of Aeronautics and Astronautics, jul 2018.

[7] T. Fukano and C.-M. Jang, "Tip clearance noise of axial flow fans operating at design and off-design condition," *Journal of Sound and Vibration*, vol. 275, no. 3-5, pp. 1027–1050, aug 2004.

[8] T. Fukano, Y. Takamatsu, and Y. Kodama, "The effects of tip clearance on the noise of low pressure axial and mixed flow fans," *Journal of Sound and Vibration*, vol. 105, no. 2, pp. 291–308, mar 1986.

[9] R. Martin, "Nacelle aerodynamic and inertial loads (nail) project, test report," *NASA CR-165760*, 1981.

[10] M. B. Graf, T. S. Wong, E. M. Greitzer, F. E. Marble, C. S. Tan, H.-W. Shin, and D. C. Wisler, "Effects of non-axisymmetric tip clearance on axial compressor performance and stability," in *Volume 1: Aircraft Engine; Marine; Turbomachinery; Microturbines and Small Turbomachinery*. ASME, jun 1997.

[11] J.-H. Zhu, W.-H. Zhang, and L. Xia, "Topology optimization in aircraft and aerospace structures design," *Archives of Computational Methods in Engineering*, vol. 23, no. 4, pp. 595–622, 2016.

[12] M. P. Bendsøe and N. Kikuchi, "Generating optimal topologies in structural design using a homogenization method," *Computer methods in applied mechanics and engineering*, vol. 71, no. 2, pp. 197–224, 1988.

[13] M. P. Bendsøe and O. Sigmund, "Material interpolation schemes in topology optimization," *Archive of applied mechanics*, vol. 69, no. 9-10, pp. 635–654, 1999.

[14] M. Zhou and G. Rozvany, "The coc algorithm, part ii: topological, geometrical and generalized shape optimization," *Computer Methods in Applied Mechanics and Engineering*, vol. 89, no. 1-3, pp. 309–336, 1991.

[15] Y. M. Xie and G. P. Steven, "A simple evolutionary procedure for structural optimization," *Computers & structures*, vol. 49, no. 5, pp. 885–896, 1993.

[16] M. Y. Wang, X. Wang, and D. Guo, "A level set method for structural topology optimization," *Computer methods in applied mechanics and engineering*, vol. 192, no. 1-2, pp. 227–246, 2003.

[17] G. Allaire, F. Jouve, and A.-M. Toader, "Structural optimization using sensitivity analysis and a level-set method," *Journal of computational physics*, vol. 194, no. 1, pp. 363–393, 2004.

[18] J. A. Norato, M. P. Bendsøe, R. B. Haber, and D. A. Tortorelli, "A topological derivative method for topology optimization," *Structural and Multidisciplinary Optimization*, vol. 33, no. 4-5, pp. 375–386, feb 2007.

[19] J. Norato, R. Haber, D. Tortorelli, and M. P. Bendsøe, "A geometry projection method for shape optimization," *International Journal for Numerical Methods in Engineering*, vol. 60, no. 14, pp. 2289–2312, 2004.

[20] J. Norato, B. Bell, and D. Tortorelli, "A geometry projection method for continuum-based topology optimization with discrete elements," *Computer Methods in Applied Mechanics and Engineering*, vol. 293, pp. 306–327, aug 2015.

[21] W. Zhang, J. Yuan, J. Zhang, and X. Guo, "A new topology optimization approach based on moving morphable components (MMC) and the ersatz material model," *Structural and Multidisciplinary Optimization*, vol. 53, no. 6, pp. 1243–1260, dec 2015.

[22] W. Zhang, W. Yang, J. Zhou, D. Li, and X. Guo, "Structural topology optimization through explicit boundary evolution," *Journal of Applied Mechanics*, vol. 84, no. 1, p. 011011, nov 2016.

[23] W. Zhang, J. Chen, X. Zhu, J. Zhou, D. Xue, X. Lei, and X. Guo, "Explicit three dimensional topology optimization via moving morphable void (MMV) approach," *Computer Methods in Applied Mechanics and Engineering*, vol. 322, pp. 590–614, aug 2017.

[24] W. Zhang, D. Li, J. Zhou, Z. Du, B. Li, and X. Guo, "A moving morphable void (MMV)-based explicit approach for topology optimization considering stress constraints," *Computer Methods in Applied Mechanics and Engineering*, vol. 334, pp. 381–413, jun 2018.

[25] S. Zhang, J. A. Norato, A. L. Gain, and N. Lyu, "A geometry projection method for the topology optimization of plate structures," *Structural and Multidisciplinary Optimization*, vol. 54, no. 5, pp. 1173–1190, 2016.

[26] E. Andreassen, A. Clausen, M. Schevenels, B. S. Lazarov, and O. Sigmund, "Efficient topology optimization in MATLAB using 88 lines of code," *Structural and Multidisciplinary Optimization*, vol. 43, no. 1, pp. 1–16, Nov 2010.

[27] O. Sigmund, "A 99 line topology optimization code written in matlab," *Structural and Multidisciplinary Optimization*, vol. 21, no. 2, pp. 120–127, Apr 2001.

[28] R. V. Kohn and G. Strang, "Optimal design and relaxation of variational problems, i," *Communications on pure and applied mathematics*, vol. 39, no. 1, pp. 113–137, 1986.

[29] R. B. Haber, C. S. Jog, and M. P. Bendsøe, "A new approach to variable-topology shape design using a constraint on perimeter," *Structural optimization*, vol. 11, no. 1-2, pp. 1–12, 1996.

[30] C. Jog, "Topology design of structures using a dual algorithm and a constraint on the perimeter," *International Journal for Numerical Methods in Engineering*, vol. 54, no. 7, pp. 1007–1019, 2002.

[31] M. P. Bendsøe and O. Sigmund, *Optimization of structural topology, shape, and material*. Springer, 1995, vol. 414.

[32] M. P. Bendsøe, "Optimal shape design as a material distribution problem," *Structural optimization*, vol. 1, no. 4, pp. 193–202, 1989.

[33] A. Rietz, "Sufficiency of a finite exponent in simp (power law) methods," *Structural and Multidisciplinary Optimization*, vol. 21, no. 2, pp. 159–163, 2001.

[34] A. Bhattacharyya, C. Conlan-Smith, and K. A. James, "Topology optimization of a bi-stable airfoil using nonlinear elasticity," in *18th AIAA/ISSMO Multidisciplinary Analysis and Optimization Conference*. American Institute of Aeronautics and Astronautics, Jun 2017.

[35] A. Verbart, M. Langelaar, and F. Van Keulen, "A unified aggregation and relaxation approach for stress-constrained topology optimization," *Structural and Multidisciplinary Optimization*, vol. 55, no. 2, pp. 663–679, 2017.

[36] P. Duysinx and M. P. Bendsøe, "Topology optimization of continuum structures with local stress constraints," *International journal for numerical methods in engineering*, vol. 43, no. 8, pp. 1453–1478, 1998.

[37] G. Beliakov, A. Pradera, T. Calvo *et al.*, *Aggregation functions: A guide for practitioners*. Springer, 2007, vol. 221.

[38] G. Kreisselmeier and R. Steinhauser, "Systematic control design by optimizing a vector performance index," in *Computer aided design of control systems*. Elsevier, 1980, pp. 113–117.

[39] R. Yang and C. Chen, "Stress-based topology optimization," *Structural optimization*, vol. 12, no. 2-3, pp. 98–105, 1996.

[40] T. Calvo and R. Mesiar, "Stability of aggregation operators." in *EUSFLAT Conf.*, 2001, pp. 475–478.

[41] O. Sigmund and J. Petersson, "Numerical instabilities in topology optimization: a survey on procedures dealing with checkerboards, mesh-dependencies and local minima," *Structural optimization*, vol. 16, no. 1, pp. 68–75, 1998.

[42] M. P. Bendsoe, J. Guedes, R. B. Haber, P. Pedersen, and J. Taylor, "An analytical model to predict optimal material properties in the context of optimal structural design," *Journal of Applied Mechanics*, vol. 61, no. 4, pp. 930–937, 1994.

[43] L. Ambrosio and G. Buttazzo, "An optimal design problem with perimeter penalization," *Calculus of Variations and Partial Differential Equations*, vol. 1, no. 1, pp. 55–69, 1993.

[44] O. Sigmund, "Design of material structures using topology optimization," Ph.D. dissertation, Technical University of Denmark Denmark, 1994.

[45] J. Petersson and O. Sigmund, "Slope constrained topology optimization," *International Journal for Numerical Methods in Engineering*, vol. 41, no. 8, pp. 1417–1434, 1998.

[46] A. Diaz and O. Sigmund, "Checkerboard patterns in layout optimization," *Structural optimization*, vol. 10, no. 1, pp. 40–45, 1995.

[47] C. S. Jog and R. B. Haber, "Stability of finite element models for distributed-parameter optimization and topology design," *Computer methods in applied mechanics and engineering*, vol. 130, no. 3-4, pp. 203–226, 1996.

[48] M. Beckers, "Optimisation topologique de structures tridimensionelles en variable discretes," *University of Liege LTAS Technical Report*, 1997.

[49] O. Sigmund, "On the design of compliant mechanisms using topology optimization," *Journal of Structural Mechanics*, vol. 25, no. 4, pp. 493–524, 1997.

[50] A. Tovar and K. Khandelwal, "Continuation method and filter reduction in global topology optimization," in *Proceedings of the Computer Methods in Mechanics Conference (CMM). Warsaw, Poland*, 2011.

[51] M. Zhou, Y. Shyy, and H. Thomas, "Checkerboard and minimum member size control in topology optimization," *Structural and Multidisciplinary Optimization*, vol. 21, no. 2, pp. 152–158, 2001.

[52] M. Zhou and G. Rozvany, "Dcoc: an optimality criteria method for large systems part i: theory," *Structural optimization*, vol. 5, no. 1-2, pp. 12–25, 1992.

[53] ——, "Dcoc: an optimality criteria method for large systems part ii: algorithm," *Structural optimization*, vol. 6, no. 4, pp. 250–262, 1993.

[54] L. Yin and W. Yang, "Optimality criteria method for topology optimization under multiple constraints," *Computers & Structures*, vol. 79, no. 20-21, pp. 1839–1850, 2001.

[55] K. Svanberg, "The method of moving asymptotes—a new method for structural optimization," *International Journal for Numerical Methods in Engineering*, vol. 24, no. 2, pp. 359–373, Feb 1987.

[56] V. Braibant and C. Fleury, "An approximation-concepts approach to shape optimal design," *Computer Methods in Applied Mechanics and Engineering*, vol. 53, no. 2, pp. 119–148, 1985.

[57] C. Fleury and V. Braibant, "Structural optimization: a new dual method using mixed variables," *International journal for numerical methods in engineering*, vol. 23, no. 3, pp. 409–428, 1986.

[58] C. Fleury and L. A. Schmit Jr, "Dual methods and approximation concepts in structural synthesis," 1980.

[59] C. Fleury, "Conlin: an efficient dual optimizer based on convex approximation concepts," *Structural optimization*, vol. 1, no. 2, pp. 81–89, 1989.

[60] ——, "Structural weight optimization by dual methods of convex programming," *International Journal for Numerical Methods in Engineering*, vol. 14, no. 12, pp. 1761–1783, 1979.

[61] ——, "Reconciliation of mathematical programming and optimality criteria approaches to structural optimization," *Foundations of structural optimization: a unified approach*, pp. 363–404, 1982.